Title

THE EMERGENCE OF SPONTANEOUS COORDINATED EPITHELIAL ROTATION ON CYLINDRICAL CURVED SURFACES

Authors

Alexandros Glentis,[1]† Carles Blanch-Mercader,[2]† Lakshmi Balasubramaniam,[1] Thuan Beng Saw,[3] Joseph d'Alessandro,[1] Sebastien Janel,[4] Audrey Douanier,[5] Benedicte Delaval,[5] Frank Lafont,[4] Chwee Teck Lim,[3,6,7] Delphine Delacour,[1] Jacques Prost,[2,3]* Wang Xi,[1]* Benoit Ladoux[1]*

Affiliations

[1] Université Paris Cité, CNRS, Institut Jacques Monod, F-75013 Paris, France.

[2] Laboratoire Physico Chimie Curie, UMR 168, Institut Curie, PSL Research University, CNRS, Sorbonne Université, 75005 Paris, France.

[3] Mechanobiology Institute, National University of Singapore, 5A Engineering Drive 1, Singapore 117411, Singapore.

[4] Univ. Lille, CNRS, Inserm, CHU Lille, Institut Pasteur Lille, U1019 - UMR 9017 - CIIL - Center for Infection and Immunity of Lille, F-59000 Lille, France

[5] CRBM, Univ Montpellier, CNRS, Montpellier, France.

[6] Department of Biomedical Engineering, National University of Singapore, 4 Engineering Drive 3, Singapore 117583, Singapore.

[7] Institute for Health Innovation & Technology, National University of Singapore, 14 Medical Drive, Singapore 117599, Singapore.

*Corresponding author. Email: jacques.prost@curie.fr (J.P.); wang.xi@ijm.fr (W.X.); benoit.ladoux@ijm.fr (B.L.)

†These authors contributed equally to this work.

Abstract

Three-dimensional collective epithelial rotation around a given axis represents a coordinated cellular movement driving tissue morphogenesis and transformation. Questions regarding such behaviors and their relationship with substrate curvatures are intimately linked to spontaneous active matter processes and to vital morphogenetic and embryonic processes. Here, using interdisciplinary approaches we study the dynamics of epithelial layers lining different cylindrical surfaces. We observe large-scale, persistent and circumferential rotation in both concavely and convexly curved cylindrical tissues. While epithelia of inverse curvature show an orthogonal switch in actomyosin network orientation and opposite apicobasal polarities, their rotational movements emerge and vary similarly within a common curvature window. We further reveal that such persisting rotation requires stable cell-cell adhesion and Rac-1-dependent cell polarity. Using an active-polar-gel model, we unveil the different relationships of collective cell polarity and actin alignment with curvatures, which lead to coordinated rotational behavior despite the inverted curvature and cytoskeleton order.

Teaser

Persistent 3D collective epithelial rotation emerges in cylindrical tissues despite inverse curvature and actin alignment.

98 **MAIN TEXT**

99

Introduction

100 Whole-tissue collective epithelial rotation (CeR) features a cohort of cells lining a quadric surface,
101 such as ellipsoid and sphere, persistently and synchronously rotating three-dimensionally (3D)
102 around a given axis with no free edge. This unexpected behavior has been observed in vivo as well
103 as in vitro. As a particular type of collective epithelial movement, CeR plays a critical role in
104 embryonic development (*1-4*) and glandular tissue transformation (*5*), accompanies tissue
105 morphogenesis (*6*) and may be involved in cancerous invasion (*7*). A marked example is a global
106 follicle epithelial cell rotation around the long axis of the egg chamber, relative to and within the
107 overlaying basement membrane, during *Drosophila* oogenesis (*1-3*). This rotation starts from stage
108 one and lasts consistently for hours until later stages (*2*). Similarly, clusters of cells in the
109 developing *Drosophila* genitalia rotate 24h after puparium formation (*4*). Besides these in vivo
110 phenomena, mammary epithelial acini embedded in 3D hydrogel matrices also demonstrate
111 coordinated rotational movement (*6, 8*), which may contribute to the establishment of acinar
112 structures (*5*) and alveologenesis (*6*). These observations suggest that CeR could be an intrinsic,
113 preserved property of curved epithelia (*9*). In addition, how dynamic epithelia interact with their
114 underlying curvatures remains an intriguing question to better understand 3D active tissue
115 mechanics.
116

117 Like other sorts of collective migration, cells could establish coordinated tissue-level front-to-rear
118 polarity, such as actin-based lamellipodial protrusions (*2*) and Rac-1 gradient (*10*), to maintain a
119 persistent CeR. In an expanding 2D epithelium with a leading front, the monolayer is facing an
120 open space. The leader cells constantly sense the presence of a "front" edge and a "rear" via
121 intercellular cadherin adhesions (*11*). This leads to a mechanosensing pathway gradient not only in
122 the leaders but spanning tens of cells behind (*12*). In contrast, cells within a rotating tissue have no
123 free edges and there is no inherent "forward" direction. Thus, the well-established mechanism for
124 a canonical leader-guided collective migration may not be entirely applicable. In a rotating
125 epithelium, each cell is surrounded by others and in principle behaves as a follower cell. Under this
126 circumstance, recent investigations have showed that cells within an intact, migrating epithelium
127 are also polarized and actively orient and contribute to directional collective migration (*13, 14*).
128 Lacking information as to the position of leader cells, these cells may rely more on anisotropic cell-
129 cell interactions to align their front-rear polar axes (*9, 11*). These include force-induced collective
130 tissue polarity (*12, 15, 16*) that may originate from anisotropic mechanical stresses, tension and
131 tugging at the cell cortex. Such mechanical signals can be propagated through actin cytoskeleton
132 network and lateral cell-cell adhesions (*17*). Hence, perturbation of actin organization and cell-cell
133 adhesion may compromise symmetry-breaking in an intact epithelium and hamper its directional
134 collective motility. In previous works using 3D epithelial acini, molecular analysis reveals a
135 relationship between coordinated rotation and actin polymerization, cell-cell adhesion as well as
136 cell apical-basal polarity (*5, 8*). Additionally, during *Drosophila oogenesis* (*1-3*), circumferentially
137 aligned actin filaments lining the inner surface of the follicular epithelium are found to aid the
138 persisting azimuthal rotation (*1, 2, 18*). In parallel, such global rotation of follicle cells is coupled
139 to the maintenance of actin stress fiber alignment, lamellipodial protrusions and remodeling of the
140 extracellular matrix (ECM) (*2*).

141 In the light of the above notions and considering CeR occurs on quadric surfaces, it is then rational
142 to deduce that CeR might be a geometry-sensitive behavior. In addition, actin filaments in cells are
143 sensitive to geometries and known to reorient and reorganize in response to 2D patterns (*19*) and
144 substrate curvatures (*20-22*). Actin cytoskeleton remodeling and nematic ordering (*23*) have been

145 shown to be implicated in cellular mechanosensing either experimentally (*24*) or theoretically (*25-*
146 *27*). Thus, concavely curved tissues could have radically different actomyosin network organization
147 from that in convexly bent tissues. Such changes could elicit variations in cell-cell/cell-substrate
148 interactions, thereby impacting tissue rotational movement (*1, 8, 28*). Given the aforementioned
149 example of *Drosophila* egg chambers, it is intuitive to envision that the polarized,
150 circumferentially-aligned actin networks may facilitate anisotropic force transition via cell-cell
151 adhesions. This could promote collective polarity and CeR along the principal stress direction as in
152 planar epithelia (*29*). However, the relationship between actin cytoskeleton network and directional
153 CeR remains elusive until now. In addition, it is not immediately clear whether CeR is correlated
154 with polarized actomyosin network organization and/or cell-cell adhesion, which may link to
155 asymmetric mechanical tension transmission in a tissue. In fact, a recent 2D patterned model has
156 revealed that the maintenance of collective rotation without a leading front requires polarity signals
157 at the single-cell level rather than stable cell-cell junctions (*10*). Furthermore, current studies
158 employed exclusively concavely curved ellipsoidal or spherical epithelia with a central, apical
159 lumen, such as a handful of in vivo (*e.g.*, *Drosophila* egg) or 3D culture (*e.g.*, acini and organoids
160 in 3D hydrogels) models. This overlooks the possibility and potential consequences of reverse
161 apicobasal and actin polarized structures as well as other complexities because of changes in
162 curvatures. Controllable geometric cues are then necessary to unravel the intertwined relationship
163 among actin alignment, cell-cell adhesion, cell polarity, curvatures, and CeR. Hence, exploring
164 collective cell dynamics as a function of curved environments will improve our understanding of
165 tissue behaviors in complicated geometrical conditions in vivo and in vitro.

166 In this study, we ask whether CeR is merely a geometry-dependent behavior or a wider phenomenon
167 that manifests itself as an intrinsic property of epithelial tissues whenever the context allows. We
168 use microfabricated tubes and fibers as simple and define cylindrical substrates for cell culture. To
169 address the above-mentioned questions and acquire deep insights into CeR dynamics on cylindrical
170 curvatures, we form concavely (negatively) and convexly (positively) curved epithelial monolayers.
171 We discover that epithelial cells can self-organize to display whole-tissue-level persistent rotation
172 over a large range of curvatures. Using an active-polar-fluid framework, we explore the rotational
173 dynamics on various curvatures with opposite nematic orders in actin cytoskeleton.

174

175 # Results
176 ## Whole-tissue level rotation in 3D concave cylindrical epithelia
177 Persistent rotation around a random axis in spherical cysts (acini, fig. S1A) of Madin-Darby Canine
178 Kidney (MDCK) cells embedded in hydrogel matrices has been reported previously (*5, 8, 28*). Such
179 a culture approach is often used to recapitulate epithelial tubular morphogenesis (*30, 31*) and tube-
180 shaped tissues (ducts, Fig. 1A and fig. S1B) with apically polarized cells facing a central lumen. To
181 facilitate cell tracking, we used MDCK histone 1-GFP cells. We formed MDCK acini and ducts of
182 varying sizes and closed topologies that are ranging from 25 to 75 μm in diameter (Ø) and up to
183 400 μm in length. In both types of MDCK tissues, we observed persistent CeR (movie S1 and S2,
184 Fig. 1B and fig. S1, C and D) when mitosis was ceased by mitotic inhibitor mitomycin *c*. This is
185 reminiscent of the fast rotation phase in *Drosophila oogenesis* when follicle cells cease division (*2,*
186 *32*). Elimination of mitosis may promote CeR as mitotic stresses (*33*) can disturb directed collective
187 migration in confined space (*21*). Although collective cell rotation happened in both MDCK acini
188 and ducts, their behaviors were different. In contrast to acini whose rotational axis varied in time,
189 rotating MDCK ducts (up to Ø = 75 μm) moved around a defined longitudinal (*l*) axis (fig. S1E).
190 This resulted in parallel cell trajectories along the cylindrical azimuthal (*a*) direction (Fig. 1, B and
191 C). Such spontaneous movement had a characteristic non-zero, relatively stable average azimuthal
192 velocity, V_θ over time and a close-to-zero, fluctuating average longitudinal velocity, V_z (Fig. 1, C

and D). These features indicate that epithelial ducts could establish collective circumferential rotation even when movement in the longitudinal direction was allowed. In this work, we then examined the coordinated rotation of cylindrical tissues (CTs) around a defined l-axis with $|\overline{V_\theta}| > 0$ and $|\overline{V_z}| \approx 0$, which persisted for at least 3 hours. In addition, we also discovered short-period CeR in pronephric tubules of developing zebrafish embryos 35hpf (*34*) (movie S3 and fig. S1, F and G). Cells in the elongating epithelial tubules also demonstrated persistent azimuthal movements for hours around the l-axis with slightly lower velocities than those of Matrigel-embedded MDCK ducts and MDCK CTs in polydimethylsiloxane (PDMS) microtubes (see next paragraph) of similar size (fig. S1H).

These observations inspired us to further investigate the emergence of CeR in epithelial monolayers with a concave cylindrical shape. To simplify the geometrical complexity of the self-organizing ducts, we used an established approach (*21*) and grew MDCKs into confluent tubular tissues inside PDMS microtubes (fig. S2A). This method allowed us to form well-defined concave MDCK tubes ranging from 25 to 250 μm in diameter and up to 1000 μm in length (Fig. 1E and fig. S2B). In addition, the MDCK tubular CTs (*t*-CTs) enclosed a hollow lumen and showed an apicobasal polarity towards the lumen (fig. S2C), reminiscent of follicle epithelial polarity (*2, 35*) and MDCK ducts (Fig. 1A and fig. S1B). Of note, we observed persistent CeR around the l-axis (movie S4) in both clockwise and counter-clockwise directions (Fig. 1F). Such coordinated motions as disclosed by the angular displacement of cells (Fig. 1G) occurred in more than 60% of *t*-CTs of all different MDCK cell types tested, spanning from 25 (smallest size possible) up to 150 μm in diameter (Fig. 1H) and persisting up to 40 hours (Fig. 1G). Moreover, we observed similar CeR behaviors inside fibronectin-/Matrigel-/poly-L-lysine-coated (fig. S3) PDMS microtubes. These observations suggested that CeR may not be sensitive to ECM components even though substrate coating could be modified by cell-induced reorganization of the matrix (*36*).

Characteristics of epithelial tissue rotation inside microtubes

To analyze the collective rotational dynamics, we virtually opened the *t*-CTs using a home-built Fiji macro (*21*) (see methods), which allowed us to convert 3D movies into 2D projections (Fig. 2A). In typical 2D projections of rotating *t*-CTs, individual cell trajectories were mostly parallel to the azimuthal axis (*a*-axis, Fig. 2B). Particle imaging velocimetry (PIV) analysis on such 2D projections showed that all cells uniformly moved in the azimuthal direction with small angular deviations in the velocities (movie S5 and fig. S4A), demonstrating a whole-tissue collective rotation. When we plotted $|\overline{V_\theta}|$ for each experiment as a function of diameter and found a non-monotonic trend with a peak at $\varnothing = 100$ μm (Fig. 2C and fig. S4B). Additionally, a threshold of $\varnothing = 150$ μm was identified, above which no CeR was observed. This threshold may be attributed to the intrinsic dynamics of MDCK epithelial cells whose velocity correlation length was measured to be ~200 μm on flat unconfined surfaces (*37, 38*). In the range of $\varnothing = 25$ to 150 μm, we found that CeR duration and azimuthal velocity correlation length, ξ_θ, increased with the diameter (Fig. 2, D and E, see methods). The relationship between ξ_θ and the diameter was in good agreement with our previous observations in advancing *t*-CTs (*21*), corresponding to cellular behaviors constrained by geometry. When analyzing average cell movement over time (for instance, V_θ in a 75 μm *t*-CT, Fig. 2F, left), we found that the emergence of CeR was correlated to a sudden increase in V_θ from nearly zero to about 10 μm/h within 2 hours (movie S4). In contrast, V_z for the same *t*-CT fluctuated with time without any particular trend (Fig. 2F, right). Spatiotemporal kymograph for V_θ showed a clear border marking the CeR starting time point between two distinct velocity patterns (i.e., different color patterns) for non-rotation and rotation regions (Fig. 2G, left). On the contrary, the kymograph for V_z demonstrated similar patterns before and after that time point (Fig. 2G, right).

Interestingly, in non-confluent conditions with advancing t-CTs (21), we also observed synchronized rotations with collective forward helicoidal movement (fig. S5 and movie S6), which lasted longer than those transient rotations within 2D advancing cohorts (37). Among confluent PDMS microtubes, two adjacent groups of cells in a t-CT could occasionally rotate in opposite directions, generating a shear border and eventually the whole tissue coordinated and rotated uniformly in one direction (movie S7 and fig. S6A, $n = 7$ out of 9). In this case, the average V_θ exhibited a gradual deviation away from zero with time (fig. S6B, top-left). The corresponding kymograph (fig. S6B, bottom-left) showed two regions of distinct velocity patterns along the l–axis at the early phase (fig. S6B from 0 to 8h), indicating two cohorts rotating in opposing directions. After, the region of one pattern waned as time passed and the other gradually became dominant over the whole l–axis (fig. S6B from 8 to 16h). Under these conditions, we observed larger fluctuations in average V_z (fig. S6B, right) than the ones obtained without shear. Overall, these results suggest that cells could coordinate their rotational movement via cell-cell interactions, indicating that cell-cell adhesion in concave t-CTs could play a role in coordinating whole-tissue CeR.

Reduced cell traction on substrate during collective tissue rotation

Since cell-substrate interaction evolves during collective epithelial migration ($29, 39$), we then investigated if the abrupt shift of t-CT dynamics from a disordered state to a homogeneous CeR could lead to an apparent change in cell traction on the substrate. To measure traction forces (TFs) of t-CTs applied on the microtube inner walls, we used soft silicone microtubes (52.3 ± 3.3 kPa in Young's modulus and Ø = 75 µm). Due to the fact that CeR is a rotating movement around a long axis without a leading front, to simplify calculation we sampled a narrow window at the bottom of the microtubes (movie S8), where curvature effects could be neglected. Before CeR started, there were no clear patterns of TFs and the average traction largely fluctuated with time (Fig. 2H, from 0 to 15h). After the onset of CeR, we measured a sheer drop in average TF (34.2 ± 13.2 Pa, $n = 5$). This reduced traction was then maintained throughout the whole CeR period with reduced fluctuation (Fig. 2H, from 15 to 40h). Interestingly, such a reduction was mainly attributed to a decrease in TF in the azimuthal direction, T_θ, because T_z (longitudinally exerted TF) remained relatively stable with time (Fig. 2I). We found a clear change in the T_θ patterns in the kymograph before and after the commencement of CeR while the T_z patterns remained unaltered (Fig. 2I). In short, our data demonstrated curvature-sensitive CeR dynamics with a threshold of Ø = 150 µm and a sudden decrease in average T_θ after the onset.

Convex CTs on microfibers show a similar rotational movement

Because substrate curvature is known to regulate collective behaviors and cell-substrate interactions ($21, 40$-42), we questioned whether a reverse curvature could cause different tissue dynamics. By growing H1-GFP MDCKs outside PDMS fibers of varying diameters (Fig. 3A, fig. S7, A and B), we achieved convex CTs on fiber (f-CTs) of inverted apicobasal polarity (fig. S7C). Surprisingly, we also observed similar CeR behaviors in f-CTs (movie S9, and fig. S7, D and E) as those of t-CTs in more than 70% of these convexly curved epithelial tissues (fig. S7F). They presented alike CeR duration (Fig. 3B) as well as a non-monotonic trend of $|\overline{V_\theta}|$ as diameter increased, which peaked at Ø = 75 µm (Fig. 3C). The threshold for CeR to emerge in f-CTs was Ø $\leq$ 100 µm, whereas f-CTs of Ø > 100 µm did not rotate ($n = 6$). In addition, MDCK f-CTs on fibronectin-/Matrigel-/poly-L-lysine-coated (fig. S8) microfibers collectively rotated in a similar fashion. Furthermore, traction force microscopy (TFM) on f-CTs was performed on comparably soft silicone microfibers (64.6 ± 4.0 kPa in Young's modulus and Ø = 75 µm). There was also a clear reduction in the profile of average traction after the onset of CeR (Fig. 3D). Furthermore, such a decrease was mainly attributed to a decrease in T_θ (Fig. 3E). In comparison with the case of t-CTs (Fig. 2H, a reduction of 34.2 ± 13.2 Pa), the magnitude of the decrease was smaller (12.1 ± 11.7 Pa, $n = 4$). The difference

between *f*-CTs and *t*-CTs might originate from different cell-substrate interactions due to different curvatures. Previous investigations have demonstrated that cell-scale curvature could affect focal adhesion (FA) organization and dynamics (*43*), which would profoundly influence pluricellular protrusion orientations (*44*) and cell polarity (*45*). In our case, it was possible that *t*-CTs and *f*-CTs responded to distinct curvatures with different tissue organizations and mechanics. The distinct mechanisms then led to different variations in traction forces during CeR and deserved future investigations. Besides this difference, we concluded that CeR could emerge in MDCK CTs regardless of the positive or negative tissue curvatures.

3D curved epithelial tissues adapt distinct organization of actomyosin networks according to their curvatures

Cellular actin networks are known to respond to substrate curvature (*20-22*). We then examined whether rotating MDCK CTs of concave and convex curvatures accommodated alike or distinct actin cytoskeleton organizations. Interestingly, we discovered that basal actin filaments aligned longitudinally inside concave *t*-CTs while azimuthally in convex *f*-CTs (Fig. 4A). Such a sharp contrast in actin filament orientations according to tissue geometries manifested in curved CTs of Ø ≤ 100 μm in both cases (Fig. 4B). In CTs of larger diameters, actin became isotropic (Fig. 4B), suggesting a synchronized effect of curvature and confinement (*21, 22*). Of note, using MDCKs expressing myosin-IIA RFP we found myosin-IIA networks in rotating *t*-CTs showed the same orientation as actin (fig. S9A and movie S10). Therefore, upon a certain degree of confinement, concavely curved MDCK *t*-CTs adopted longitudinally aligned actomyosin networks that were perpendicular to the direction of their CeR. On the contrary, convexly curved *f*-CTs had the azimuthally aligned actin networks that were oriented along their CeR direction. Additionally, the formation of such oriented actin networks was confirmed in MDCKs expressing LifeAct-GFP (fig. S9B) and recurred in both fibronectin (Fig. 4B) and Matrigel (fig. S9C) coated PDMS microtubes. In the case of *t*-CT, it might not link to substrate rigidity either since basal actin in Matrigel- (33.3 ± 1.6 Pa in Young's modulus for Matrigel vs. ~1–2 MPa for PDMS (*46*) microtubes) embedded MDCK ducts also presented *l*-axial alignment (fig. S9D). Interestingly, despite these changes in the nematic alignment of actomyosin cytoskeleton, cell shape within CTs showed no preferential orientation (fig. S9E). In addition, conventional ventral actin stress fibers (SFs) that are attached to focal adhesions (FAs) at the cell edges might form and align in a similar fashion (fig. S10). We further noticed that these actin filaments might extend over multiple cells via cell-cell junctions (CCJs) (Fig. 4, A and C), suggesting that they might interact with cell-cell adhesions for mechanical force transduction (*47*). In short, we observed that actin networks oriented in distinct directions according to the curvature of the tissues (see also Theoretical Section 6 in Supplementary Materials).

CCJs of different orientations bear anisotropic tensions

Based on the above observations, we then questioned the relationship between CCJs and oriented actin filaments. The former is anchored to and relies on actin networks to withstand substantial forces (*48*). We found that E-cadherin (E-cad), a key cell adhesion molecule, showed no preferential distribution in variously oriented CCJs in both MDCK WT *t*-CTs and *f*-CTs (fig. S11). In contrast, another component of adherens junctions, β-catenin (*49*), formed finger-like structures in parallel to the basal actin alignment, i.e., aligning in longitudinal or azimuthal directions for *t*-CTs or *f*-CTs (Fig. 4C), respectively. As a result, β-catenin was preferentially recruited to the CCJs that were perpendicular to the basal actin networks in either case (Fig. 4D). β-catenin is known to link to actin cytoskeleton via α-catenin, a key receptor for transmembrane cadherin adhesion complexes (*50*). Looking at the marker (α-18) for tension-bearing α-catenin (*51*), we also found an anisotropic distribution of unfolded (i.e., bearing tensions) α-catenin to CCJs where the β-catenin fingers were seen (Fig. 4D). These findings suggested that the CCJs in *t*-CTs that were parallel to CeR direction

($\overrightarrow{V_\theta}$ direction, Fig. 4D left panel, violet α-18 enriched CCJ) were bearing tensions as opposed to *f*-CTs where tension was supported by CCJs perpendicular to $\overrightarrow{V_\theta}$ (Fig. 4D right panel, violet α-18 enriched CCJ). Interestingly, these findings showed that large coordinated collective movements could emerge despite different molecular organizations of cytoskeleton and CCJ. Such organizations are known to promote tension anisotropy as previously described in other systems (*52, 53*) and accommodate geometric constraints. This was supported by our discoveries that *t*-CTs continued rotating even when tissue contractility was mitigated by a ROCK inhibitor, Y-27 (*54*) (movie S11). Interestingly, disrupting CCJs using EGTA eliminated aligned actin filament organizations (Fig. 4, E and F). The profound interdependence of CCJs and actin alignment as well as the emergence of anisotropic tension and various planar polarities in curved epithelial tissues deserve further investigation.

Proper cell-cell adhesions are essential for CeR

CCJs are known to play an important role in collective cell migrations in various in vivo and in vitro systems (*55*). In our attempts using EGTA to disrupt CCJs, we found that such treatment halted CeR, while CeR recurred in both concave and convex CTs after EGTA washout (Fig. 5, A and B). This is different from 2D epithelial rotation in rings (*10*), which remains unaffected upon EGTA treatment. We then inactivated E-cad gene using CRISPR-Cas9 (*38*). E-cad knock-out (KO) in MDCKs weakened the cell-cell adhesions but cells could still maintain their contact through another cadherin (cadherin 6, fig. S12) (*38*). We observed similar CeR in both E-cad KO *t*-CTs and *f*-CTs (fig. S13 and movie S12). Nevertheless, E-cad KO resulted in a significantly shorter velocity correlation length (ξ = ~140 μm) in comparison with MDCK WT (ξ = ~200 μm) (*38*). This led to a decrease in the CeR thresholds ($\emptyset \leq 100$ μm for E-cad KO *t*-CTs ($n = 11$) and $\emptyset \leq 50$ μm for E-cad KO *f*-CTs ($n = 22$). In addition, E-cad KO caused marked reductions in CeR event percentages (fig. S13A) and rotation speeds (fig. S13, B, C and E), although cells could maintain coordinated rotation for hours (fig. S13, C-F).

To further perturb CCJs, we simultaneously knocked out E-cadherin and cadherin 6 in MDCK cells (MDCK cadherin double KO). These MDCK cadherin double KO cells lost β-catenin expression at the adherens junctions (fig. S12) and did not show CeR in either *t*-CTs ($n = 15$) or *f*-CTs ($n = 15$) in the range of $\emptyset = 50 – 100$ μm even at their confluence (fig. S14 and movie S13). In addition, we formed *t*-CTs ($n = 16$) or *f*-CTs ($n = 8$) using MDCK α-catenin knock-down (α-cat KD) cells (*37*) on both concavely and convexly curved scaffolds. Similarly, these cells showed alike features of random motions in V_θ and V_z, as well as their corresponding kymographs (fig. S15). Altogether, these results showed that the establishment and maintenance of collective cell rotation required stable cadherin-mediated CCJs in response to cylindrical curvatures.

Roles of lamellipodial protrusions in CeR

After investigating the roles of CCJ stability, we asked how protrusive forces usually generated by actin filaments could impact CeR. Using high-resolution time-lapse imaging, we discovered that the long-range, basal actin filaments in both *t*-CTs and *f*-CTs remained persistently immobile related to the substratum during CeR (Fig. 5C and movie S14) and may disappear when they reached the rear edge of the cell. In addition, we found that actin-based cryptic lamellipodia continuously appeared at the cell edges (Fig. 5D). Interestingly, these protrusions were highly aligned with the CeR direction, regardless of the oriented actomyosin networks (Fig. 4, A and B, and fig. S9, A and B) and the random cell orientation (fig. S9E) in all confluent CTs. To check whether these were polarized structures, we monitored YFP-PBD signals as a marker for active

Rac-1 and Cdc42 and found that cells accumulate Rac-1 at their fronts as they protruded forward (fig. S16), suggesting the role of polarized protrusions in CeR. This was supported by treatment with a Rac-1 inhibitor (Z62), which immediately halted CeR (Fig. 5E). Overall, we identified immobile long-range actin filaments in rotating *t*-CTs and *f*-CTs while polarized cellular protrusions as essential factors for persistent CeR.

An active-polar-gel description for CeR

To gain insights into 3D CeR, we used an overdamped active-polar-fluid framework (*56-58*) including explicit couplings between substrate curvature and cell polarity (see Theoretical Section 1-2 in Supplementary Materials). To describe MDCK CTs, we accounted for an average cell polarity and an average cell velocity given by a polarity field $\boldsymbol{p}$ and a velocity field $\boldsymbol{v}$, respectively. Here, the polarity field $\boldsymbol{p}$ can represent an averaged direction of planar polarity in cell monolayers, such as cryptic lamellipodia on one side of cells. In cylindrical geometries, the principal directions of a cylindrical substrate are the longitudinal direction $\hat{z}$ and the azimuthal direction $\hat{\theta}$ (Fig. 6A, *l* and *a* in the experimental section, respectively). In addition, the substrate curvature along the longitudinal direction vanishes, and along the azimuthal direction is $1/R$, where $R = \emptyset/2$ is the substrate radius. The curvature $1/R$ changes sign when describing concave (negative) or convex (positive) curvatures corresponding to microtubes and microfibers, respectively. In this case, we allowed R to change sign to account for different curvatures, *i.e.*, $R < 0$ for microtubes and $R > 0$ for microfibers.

To describe the effects of substrate curvature on cell polarity, we accounted for couplings allowed by symmetries between the substrate curvature and the polarity field. For cylindrical substrates, we found that the equilibrium uniform polarity states are determined as the minimum of an effective free-energy density f (see Theoretical Section $1 - 3$ in Supplementary Materials for a derivation of f as a thin film limit of a 3D Landau-Ginzburg free-energy density):

$$f = \left(\chi_2 + \frac{\bar{\beta}_1}{R} + \frac{\bar{\beta}_2}{R^2}\right)\frac{(p_z^2 + p_\theta^2)}{2} + \left(\frac{\beta_1}{R} + \frac{\beta_2}{R^2}\right)\frac{p_\theta^2}{2} + \chi_4\frac{(p_z^2 + p_\theta^2)^2}{4} \quad (1)$$

where p_z and p_θ are the components of the polarity field $\boldsymbol{p}$ in the longitudinal and azimuthal directions, respectively. In view of the fact that confluent MDCK cell monolayers are on average immobile on a flat substrate (*59, 60*), we considered that a disordered state dominates for a sufficiently large radius R and set the phenomenological parameters $\chi_2 > 0$ and $\chi_4 > 0$. For intermediate R, the substrate curvature can induce ordered states via couplings with the polarity field. The parameters $(\beta_1, \bar{\beta}_1)$ and $(\beta_2, \bar{\beta}_2)$ are amplitudes associated with linear and quadratic couplings in $1/R$ and the polarity field, respectively. Hence, the linear couplings $(\beta_1, \bar{\beta}_1)$ change sign with curvature (*i.e.*, convex (positive) to concave (negative)), whereas the quadratic couplings $(\beta_2, \bar{\beta}_2)$ do not (Fig. 6A). As a result, quadratic couplings may lead to collective rotation in both concave and convex CTs while linear couplings may only cause CeR in either one of the conditions.

The radius R then determines the state of CTs (either rotation or no rotation, see Theoretical Section $3 - 4$ in Supplementary Materials for details). Within the parameter regime where $\bar{\beta}_1 = \bar{\beta}_2 = 0$ in Eq. (1), the system can either assume a disordered phase (no rotation) whereby $p_z = p_\theta = 0$, or an azimuthal ordered phase (rotation) whereby $p_z = 0$ and $p_\theta = \pm\mathcal{P}$ (Fig. 6B and see Theoretical Section $3 - 4$), where $\mathcal{P}$ depends on R and material parameters. In the overdamped limit, force balance in the azimuthal direction leads to the steady-state azimuthal velocity field in the azimuthal ordered phase (see Theoretical Section 4 in Supplementary Materials):

$$v_\theta = \pm \frac{T_0 \sqrt{\chi_2/\chi_4}}{\xi(1 + \alpha_2/r^2)} \sqrt{-\left(1 + \frac{1}{r} + \frac{\alpha_1}{r^2}\right)} \qquad (2)$$

which depends only on two dimensionless parameters: : $\alpha_1 = \beta_2\chi_2/\beta_1^2$ and $\alpha_2 = \eta\chi_2^2/\xi\beta_1^2$ and the dimensionless radius r = $R\chi_2/\beta_1$. The parameter η corresponds to the shear viscosity, ξ to a friction coefficient with the underlying substrate and T_0 to the amplitude of polar traction forces. With this, we found that the direction of p_θ and v_θ is set by a symmetry-breaking process without sign preference, i.e., no chirality in CeR, in agreement with our experiments in Fig. 1F and fig. S7E. Besides, we found that in the presence of a free edge, the velocity field is helicoidal and involves a superposition of the azimuthal velocity (2) and the longitudinal velocity, which is also in agreement with our findings in fig. S5.

Next, we infer the contribution of linear and quadratic couplings to curvature in CTs, by applying our continuum approach to the velocity patterns of CTs in their steady-rotational state in a range of Ø from 25 to 250 µm (Fig. 6C, see the fitting procedure in Theoretical Section 5 in Supplementary Materials). Our fitting disclosed a region of the parameter space that is compatible with the experimental measurements (Fig. 6C, and Table S1 in Theoretical Section 5 in Supplementary Materials). In this region, the ratio $|\beta_2/\beta_1| > 200\ \mu m$ is larger than the CeR thresholds (Ø > 150 µm for t-CTs and Ø > 100 µm for f-CTs), showing that quadratic couplings are predominant for CeR in curved CTs. Hence, we concluded that a quadratic coupling of the polarity field in the MDCK CTs to the curvature led to the persistent CeR. Furthermore, using the parameters that fitted best our measurements (Fig. 6C) we identified an experimental trajectory by changing R, which traversed both the CeR and disordered phases (Fig. 6B, green line). In this regime, for sufficiently small radius, the azimuthal velocity, set by balancing active traction forces and viscous stresses, increases with the substrate radius. For sufficiently large radius, the reduction of the curvature field, leads to a reduction of both the polar order parameter and the azimuthal velocity, vanishing above a critical radius (Fig. 6C). This is in agreement with the experimental data that describe the curvature-velocity relationship (Fig. 3C).

Moreover, we studied how the orientation of actin fibrils couples to curvature in MDCK CTs. To describe the average orientation of actin fibrils, we used a director field $\hat{n}$. Besides, we consider that actin fibrils exhibit a nematic order, i.e., our theoretical description is invariant under inversions $\hat{n} \to -\hat{n}$ and $|\hat{n}| = 1$. Then, the previous theoretical approach was extended by including couplings between the director field $\hat{n}$, the polarity field p and the substrate curvature. We found that the equilibrium uniform states are determined as the minimum of an effective free-energy density that generalizes Eq. (1) (see Theoretical Section 6 in Supplementary Materials). To infer the nature of the curvature couplings that determined actin network organization in MDCK CTs, we compared the equilibrium uniform orientation patterns of $\hat{n}$ to the experimental case. In our experiments, the orientation of actin fibrils was found, on average, in the longitudinal direction for t-CTs (concave) and in the azimuthal direction for f-CTs (convex) in a range of Ø = 25 – 100 µm (Fig. 4A and B). This observation indicates that linear couplings between the curvature and the director field $\hat{n}$ are predominant for the organization of actin networks because they change sign with curvature (*i.e.*, concave (negative) to convex (positive)). This analysis suggests that such linear curvature couplings could arise from different microscopic mechanisms, such as direct interactions between the substrate curvature and the actin fibrils, or indirect interactions mediated by cell polarity markers like cryptic lamellipodia (see Theoretical Section 6 in Supplementary Materials).

Discussion

3D tissue rotation is an interesting phenomenon where a cohort of cells without a free front line a quadric surface and collectively rotate around an axis. However, even CeR happens in tissues of explicit curvatures, the relationship between CeR and tissue geometries remains largely unexplored. Using in vitro 3D tissue rotational models, we expand the repertoire of CeR beyond current negatively curved epithelial models. We highlight the robustness of CeR on both concavely and convexly curved substrates regardless of apicobasal polarity and cytoskeleton networks. Our experimental findings are well captured by a theoretical approach based on active-polar-fluid (Fig. 6) where cell polarity, velocity and actin filaments are coupled quadratically or linearly to the tissue curvatures. Our discoveries have important implications for our understanding of in vitro and in vivo tissue behaviors in complex geometrical conditions, concerning front-rear cell polarity, collective cell migration and long-range actomyosin order.

First of all, it is intriguing to find that CTs with completely different oriented actin networks demonstrate much alike collective rotational migration. This could indicate mechanical stresses are transmitted in different directions in t-CTs and f-CTs, leading to anisotropic tension in tissues. Given the fact that actin filaments link to both CCJs and FAs, complex crosstalk between cell-cell and cell-substrate may determine the distribution of different actin filaments and tension in the curved tissues. The negative curvature may favor the formation of CCJ-associated actin filaments while the convex geometry could promote the growth of conventional ventral actin SFs with both ends attached to FAs. The comparison of our active-polar-gel description to experiments on MDCK CTs suggests that the organization of actin filaments could be explained by two different linear curvature couplings. To further identify the nature of the mechanism, one could study the cross-correlations between the orientation of actin filaments and cell migration on substrates with more complex curvature patterns, such as undulated stripes, or examine their spatiotemporal fluctuations in t-CTs and f-CTs for a fixed diameter. Nevertheless, CeR emerges regardless of the different actin networks and potentially distinct anisotropic tissue tension distributions. Thus, an intuitive implication could be that CeR is a state minimizing shear in epithelia whose migratory direction does not necessarily align with principal stress direction in tissue as 2D collective migration (*29*). Such a mismatch between collective movement and the principal stress direction has been reported in human mammary gland organoids. In these situations, rigid body rotation of nascent alveoli occurs before circumferential tension in the tissue overrides axial one as well as cell repolarization in the azimuthal direction (*6*). In our case, helical migration due to the combination of CeR and longitudinal expansion emerges in both non-confluent t-CTs and f-CTs, where there is a clear l-axial stress. In addition, reduction of mechanical stress in CTs by Y-27 treatment does not block CeR. These findings are in line with the notion that CeR could emerge regardless of different actomyosin and CCJ organizations that promote tension anisotropy.

Nevertheless, the underlying principles and factors that trigger collective polarity for CeR remain unclear. Cellular protrusions seem to be important and cells tend to protrude on substrates where they could well attach. Whereas in our TFM measurement on t-CTs, we find an abrupt decrease in traction T_θ. Such an observation reveals a transition in cell-substrate interactions from a chaotic status without defined collective movement to CeR. This may suggest that maintaining CeR does not require strong cell-substrate interactions. Before the CeR onset, cells in the tissue might be grouped into separate clusters that constantly interact with their neighboring cells. This allows long-range force transmission via cytoskeleton and cell-cell adhesions across the entire clusters (*16, 39*). The kymographs of T_θ and T_z before CeR (Fig. 2I) then demonstrate regional traction distributions. These regional resultant forces could be either positive or negative and thus, the measurement of the average T (Fig. 2H, 0 – 15 h) shows large fluctuations with time. Once CeR emerges as a state that may minimize shear (*29*), T_θ mitigates throughout the entire t-CT with unchanged T_z, resulting

in a reduced T (Fig. 2H, 15 – 40 h). This finding may be explained by a possible redistribution of forces from cell-substrate towards cell-cell contacts to promote coordinated motion. Of note, though similar, the decrease in T_θ value is less significant in rotating f-CTs. We speculate that the reduction in cell-substrate traction at the onset of CeR could lead to a competition between the active contractility and the bending elasticity of the azimuthally aligned actin filaments (*20*) in f-CTs. The bent actin filaments may still require strong cell-substrate adhesion even after the CeR onset. Whereas this scenario does not exist in t-CTs, where the longitudinally aligned actin filaments are not bent. Thus, actin bending in f-CTs may require strong and stable cell-substrate interactions. Altogether, these results indicate different and indirect roles of varying actomyosin networks in CeRs could exist and how these networks are established and maintained deserve further investigation.

A recent study reveals the existence of immobile actin SFs in *Drosophila* and their role in promoting parallel cell trajectories during collective rotational migration (*18*). The authors propose a treadmilling behavior that enables SFs to persist in a moving epithelium. This model may resemble the CeR in positively curved f-CTs but we notice that the follicular epithelium in *Drosophila* egg chamber is negatively bent and has an inverted apicobasal polarity. The stationary, azimuthally aligned actin filaments in f-CTs may indeed undergo treadmilling by adding new adhesions and actomyosin segments at their fronts. However, our paxillin staining did not reveal multiple adhesions along the actin filaments (fig. S10) and our results show they could connect to adherens junctions. Furthermore, in t-CTs where the actin filaments are aligned perpendicular to CeR direction, cells' trajectories were also mostly in parallel (Fig. 2B). Thus, our results suggest that at least in MDCK epithelia, cells could keep their parallel trajectories without the support of aligned actin networks while the role of SFs could not be entirely ruled out. As the immobile actin filaments in t-CTs have to be disassembled and give space to an incoming cell, it is impossible for such l-axial filaments to undergo front-rear treadmilling. Instead, they may slide along the CCJs over time, a phenomenon that is recently discovered in apical SFs in developing epithelial tissues (*61*). It is then of high interest to carefully investigate the lifetimes as well as the nucleation and disassembly mechanisms of both l- and a-axial actin in the follow-up studies. A scrutinization of the evolution of CCJs and their connections with these oriented actomyosin networks could also provide important information about epithelial organization during CeR. In this work, partial perturbation of CCJs by E-cad KO does not fully block CeR in small CTs but results in notable reductions in CeR event percentages and $|\overline{V_\theta}|$. This could be attributed to a significant decrease in velocity correlation length. Interestingly, such a change in epithelial properties may correspond to a downwards shifting of the experimental trajectory (green line) on the y-axis in the phase diagram of Fig. 6B, i.e., to regions where the CeR thresholds are smaller. Further perturbation of CCJs (MDCK cadherin double KO and α-catenin KD) leads to the blockage of CeR in all situations and random motions in V_θ and V_z even at a high confluence, highlighting the essential role of CCJ stability in CeR.

Our combined experimental and theoretical approach proposes a framework to understand the emergence of collective cell dynamics on cylindrical curvatures. Altogether, this work presents a reductionist experimental approach and biophysical modeling to explore CeR in both concavely and convexly curved epithelia. Interestingly, the reverse organization between actin structures and junctional complexes in microtubes and on microfibers demonstrates that molecular functional components can adapt to geometrical constraints to favor similar behaviors at the multicellular level. We anticipate that these versatile functional structures may help cells to navigate their environment. Our model enables future investigations into rotating tissues of different actomyosin networks, apicobasal polarity and actin-CCJ interactions, thus offering opportunities to shed light on the functional link between tissue mechanics and tissue development.

Materials and Methods

All experiments were conducted according to the regulations of the French legislation and European Union guidelines. Approval by an ethics committee is not required for experiments using MDCK cell lines.

Live imaging on zebrafish embryos

Zebrafish Tg(cldnb:lynEGFP) transgenic lines (gift from D. Gilmour) (*62*) were raised at 28°C and kept under standard laboratory conditions according to European Union guidelines for the handling of laboratory animals. The use of zebrafish was approved by the Comité d'Ethique pour l'Expérimentation Animale and the Direction Sanitaire et Vétérinaire de l'Hérault (CRBM aquatic facility, C-34-172-39). Embryos were staged according to hours post-fertilization (hpf). One cell stage embryos were injected with 100 pg of H2B-mcherry mRNA. Capped mRNA were synthesized with the mMessage mMachine SP6 in vitro transcription kit (Ambion- Thermo Fisher) using PCS2 + H2B-mcherry (gift from Philipp Keller; Addgene plasmid #99265; https://www.addgene.org/99265/) as template. Before live imaging, 24hpf zebrafish embryos were manually sorted on the basis of their fluorescence and dechorionated. 1-Phenyl-2-thiourea (PTU, Sigma) was then used to remove pigmentation according to standard protocols. For live imaging, embryos are anesthetized with tricaine methanesulfonate (MS222, Sigma, 0.2 mg/mL) until larvae are motionless and non-responsive to a touch stimulus. Embryos were then mounted in 1% low-melting agarose containing in E3 medium on 8-well microscopy slides (Ibidi). Additional tricaine/E3 is added to fill the culture dish. Timelapse imaging of the pronephros was acquired using a spinning disk microscope driven by Fusion software: Inverted Nikon microscope coupled to a Dragonfly Andor spinning disk, EMCCD iXon888 Life Andor, 40x Apo / 1.15 NA / WD 0.6 mm / water. Images were recorded every 5 minutes (z stack of 1μm interval) between 34 and 51 hpf. Image processing (cropping, rotation, drift correction, brightness and contrast adjustment) were performed with Fiji or Imaris (Bitplane) software.

MDCK cell culture

MDCK-WT (Madin-Darby canine kidney wild type) cells, MDCK-histone 1-GFP (stable cell line transfected with histone 1-GFP, H1-GFP), MDCK-LifeAct-GFP (stable cell line transfected with LifeAct GFP, binding to actin filaments), MDCK-PBD-YFP (stable cell line expressing YFP-tagged p21-binding domain probe of activated Rac1 and Cdc42, kindly provided by Fernando Martin-Belmonte, Universidad Autónoma de Madrid), MDCK-Myosin-II-RFP (stable cell line transfected with Myosin-II-RFP), MDCK Ecad-KO, MDCK double cadherin KO and MDCK α-cat KD were cultured in complete DMEM medium (Life Technologies), supplemented with 10% fetal bovine serum and 1% penicillin/streptomycin). All cells were cultured at 37°C and 5% CO2 conditions.

Generation of MDCK cadherin double KO cell line

MDCK E-cadherin (encoded by *CDH1*) and cadherin-6 (encoded by *CDH6*) double KO stable cells were generated from MDCK E-cadherin KO (*38*) using a pair of CRISPR-Cas9 plasmids (Addgene 48138 and Addgene 62988). The 2 following gRNA sequences were used: CACCGGGGGATATACAGGCCACCAAG and CACCGGTTGTGTATAGTATCCTACA. Around 5 million cells were electroporated (Neon Transfection System Invitrogen) with 10 μg of plasmid in one pulse of 20 ms and at 1,650 V. Twenty-four hours later, cells were selected by adding 2 μg ml–1 puromycin in the culture media. Twenty-four hours later, GFP-positive single cells were sorted in 96 well plates by flow cytometry using an Influx 500 sorter-analyser (BD BioSciences). The clonal populations were then selected based on the absence of β-catenin by immunofluorescence staining. The absence of cadherin-6 in the clones generated was confirmed by western blot analysis of protein extracts (fig. S13).

Western blot

Proteins for MDCK cells were extracted using lysis buffer (100mM Tris7.5 + 150mM NaCl + 0.5% NP40 + 10% Glycérol + 0.5% Triton) containing 1X protease inhibitor cocktail (Roche) and 1X phosphatase inhibitor (Phosphostop, Roche). Protein (20 μg) was loaded onto NuPage 4–12% Bis-Tris gel using a mini gel tank and dry transferred using an iBlot transfer system (Invitrogen). Non-specific sites were blocked using 5% non-fat dry milk in 0.1% PBS Tween. Primary antibodies (GAPDH from ThermoFisher Scientific, ref mA5-15738 or cadherin-6 from Cell Signaling, ref 48111) were diluted in PBS Tween at 1:1000 and the blots were incubated overnight on a shaker at 4 °C. The blots were then washed 3-4 times for 10 min each in PBS 0.1% Tween and incubated with either HRP linked (Pierce) or Dylight 800 (ThermoFisher Scientific) linked secondary antibodies at 1:10 000 for 2 hours. The blots were then washed three times with PBS 0.1% Tween or TBST for 10 min each. The blots were then revealed using CHEMIDOC MP (BioRad) using Super West Femto (34095 Thermo Scientific) or chemiluminescence.

Culture of Matrigel-embedded MDCK cysts and ducts

To culture MDCK cysts and ducts within Matrigel (Corning, #734-1100) we adopted and adjusted methods described previously (*31, 63*). Briefly, detached MDCK H1-GFP cells (10^4 cells/ml) were suspended with 50% Matrigel (diluted in complete DMEM medium) by repetitive pipetting. Drops (100 μl) of cell-Matrigel mixture were transferred to a precooled glass-bottom Petri dish (Fluorodish™, Cat#: FD35-100) and incubated at 37 ºC for 1 h for gel polymerization. The cell-Matrigel drops were then overlaid with 3 ml of complete DMEM medium for long-term culture. The medium was changed every 2 days. Typically, MDCK cysts and ducts developed after culturing for 6 days and fluorescent microscopy imaging was performed between 7 and 10 days after cell seeding.

Microfabrication of elastomeric microtubes and microfibers

Microtubes were fabricated inside polydimethylsiloxane (PDMS) blocks as described previously (*21*). Briefly, smooth copper or platinum wires (Goodfellow SARL) of different diameters were aligned in parallel 1 – 2 μm above a silicon wafer (1×1 cm^2) using a precise stage (*64*) that could control the positions of each wire. A fresh mixture of silicone elastomer base and silicone elastomer curing agent (Sylgard 184, DOWSIL™, 10:1 by weight) was poured on the silicon wafer to cover the metal wires. The entire setup was then left at room temperature for 24 h for PDMS polymerization. After the polymerization, the metal wire was pulled out during a sonication process in an acetone solution, forming parallel microtubes in a PDMS block. As-fabricated PDMS blocks were then heated up to 80 °C in an oven for 30 min to remove any acetone remnant. The PDMS blocks containing straight, parallel microtubes were later cut in a direction perpendicular to the microtubes into small pieces of ~0.5 – 1 mm (this is also the length of the microtubes) in the width. These small pieces were then stuck to a glass-bottom petridish (Fluorodish™, Cat#: FD35-100) for protein functionalization. The two openings of the microtubes allowed efficient diffusion of medium throughout, avoiding creation of a biochemical gradient inside the microtubes.

To fabricate PDMS microfibers, freshly mixed silicone elastomer base and curing agent (Sylgard 184, DOWSIL™, 10:1 by weight) were left at room temperature for about 10 h to allow viscosity of the mixture to increase. PDMS microfibers of different sizes were then pulled out of the viscous mixture at different speeds using 200 μl pipette tips. As-fabricated microfibers were hanged in an 80 °C oven for 1 h for full polymerization. These microfibers were cut into pieces of ~0.5 cm in length and hanged between two glass coverslips of 170 μm in thickness with a gap of *ca.* 0.5 – 1 mm, thus avoiding cells on the microfibers getting into contact with the substrate. The whole set-up was then stuck to a glass-bottom petridish (Fluorodish™, Cat#: FD35-100) for protein functionalization.

Following the similar procedures as above, soft silicon microtubes and microfibers were made from a mixture of silicon gels 52-276 A and B (Dow Corning) at a ratio of 5:6. The curing time for this soft polymer is 30 – 60 min at room temperature, following by a 1-h baking at 80 °C.

To facilitate cell adhesion, PDMS microtubes and microfibers were first treated with oxygen plasma for 5 min using a plasma cleaner (P/N PDC-002-HPCE, HARRICK PLASMA). Soft silicon microtubes/fibers were exposed to UV in a UVO-Cleaner (Jelight company, Inc, model 342-220) for 2 min. All the elastomeric microtubes/fibers were then coated with fibronectin (Sigma-Aldrich) by soaking into a fibronectin solution of 50 μg/ml overnight at 4 °C. These cylindrical scaffolds were thoroughly rinsed with $1 \times$ PBS before cell seeding.

Formation of MDCK epithelial cylindrical tissues

To form MDCK *t*-CTs, MDCK cells were seeded right outside both openings of elastomeric microtubes and let migrate into the microtubes freely until confluence. Before the confluence, MDCK cohorts inside microtubes formed advancing, non-confluent *t*-CTs. It normally took 2 – 3 days to form confluent *t*-CTs and a complete DMEM medium containing 10 μM mitomycin *c* (Sigma-Aldrich) was added for 1 h to block cell division (collective rotation in CTs could also be observed without the treatment of mitomycin *c*, but blocking mitosis significantly increased the percentage of rotation). As-formed *t*-CTs were washed and immersed with/in fresh DMEM medium and mounted on a confocal microscope (Zeiss, LSM 780 or LSM 980) for 3D live-cell imaging.

MDCK *f*-CTs were formed in a similar way by seeding MDCK cells right next to both ends of elastomeric microfibers and let them to migrate onto the microfibers freely until confluence. As-formed *f*-CTs were also treated with 10 μM mitomycin *c* 1 h to block mitosis and enhance CeR.

Life-cell imaging of collective rotation in MDCK CTs and drug treatment

Samples of MDCK CTs were mounted on a confocal microscope (Zeiss, LSM 780 or LSM 980) and *z*-stacks (0.5 – 1 μm per Z step) covering the whole volume of MDCK CTs were recorded at 10 min/frame with either 25×, 40× or 63× objectives. Alternatively, MDCK CTs were imaged at 10 min/frame with a Biostation IM-Q (Nikon) using a $10 \times$ objectives with multiple focal planes to cover the entire MDCK CTs. To facilitate cell tracking, H1-GFP MDCKs or MDCKs expressing LifeAct GFP or YFP-PBD or MDCK-Myosin-II-RFP were used. Otherwise, nuclei in MDCK WT, Ecad-KO, cadherin double KO, or α-catenin KD cells were stained with NUCLEAR-ID® Blue DNA Dye (Enzo, ENZ-CHM103-0200) by mixing 1 μL of the dye in 1mL DMEM medium. 3D time-lapse videos were recorded over a period ranging from 12 to 72 h. During imaging, drug treatment to rotating MDCK CTs was performed. Drugs were added during the course of imaging to allow continuous observations of the effects for 10 – 20 h. Similarly, washout of drugs using fresh pre-warmed complete DMEM medium was recorded by continuous live-cell imaging that lasted for 10 – 30 h after. To inhibit Rac-1 activity, cells were treated with 100 μM Z62954982 (MERCK Millipore, Cat#: CAS 1090893-12-1). For Ca^{2+}-dependent adhesions disruption, EGTA (Sigma Aldrich) was added to make a final concentration of 2.5 mM during experiments and left to react for at least 20h. To inhibit cell contractility, ROCK inhibitor Y-27632 (Sigma Aldrich, Y0503) was added to DMEM medium to make a final concentration of 10 – 25 μM.

Immunofluorescent staining of MDCK CTs and confocal microscopy

Before cell fixation, live-cell imaging of MDCK CTs was performed using a Biostation IM-Q (Nikon) to spot collective cell rotation in CTs. The rotating CTs were then immediately fixed with 4% paraformaldehyde for 20 min, permeabilized with 0.1% Triton X-100 for 10 min while shaking and blocked in a solution of 3% BSA for 2h. Antibodies and Phalloidin were diluted in a 3% BSA solution. Actin cytoskeleton was visualized after staining with either Alexa-488 (Invitrogen,

A12379, 1:250), Alexa-568 (Invitrogen, A12380, 1:250) or Alexa-647 (Invitrogen, A22287, 1:25) labeled Phalloidin for 2 h. For staining α- or β-catenin, samples were incubated with a primary antibody against either α-catenin, raised in rabbit (1:100, Sigma) or primary antibody against β-catenin, raised in rabbit (1:100, Sigma). For staining apical side of MDCK CTs, samples were incubated with a primary antibody against GP-135, raised in mouse (1:100, DSHB). All samples were incubated overnight with primary antibody solutions at 4°C, while shaking. The next day a washing procedure of 3×10 min using 1× PBS was applied to wash away the extra primary antibodies. Cells were then stained with 1:50–200 dilutions of secondary antibodies (Invitrogen) and Hoechst 33342 (Life Technologies, H3570, 1:1000). Samples were mounted with anti-bleaching medium (Vector Laboratories, H-1000) and *z*-stacks of MDCK CTs were acquired on a confocal microscope (Zeiss LSM710 or LSM780) using a 40× or a 25× oil or a 63× water objectives at 0.5 to 1 µm per stack.

Traction force microscopy

Traction force microscopy (*16, 41*) was performed to examine traction exerted by MDCK CTs on cylindrical substrates. In brief, soft silicon microtubes and microfibers were coated with a layer of red-fluorescent carvoxylate-modified microbeads (Invitrogen, F8810) by silanizing the surfaces using a 10% solution of (3-Aminopropyl)triethoxysilane (Sigma Aldrich, A3648) in 100% ethanol for 15 min. The microbeads-laden soft silicon microtubes and microfibers were later coated with fibronectin by direct incubation at a concentration of 50 µg /ml overnight at 4°C. MDCK cells were then allowed to form epithelial CTs on these soft cylindrical substrates. Live-cell imaging was performed on these samples to record bead displacement and CeR simultaneously. At the end of the video, 500 µl of 10% SDS were added in the medium to remove cells in order to obtain reference positions of the microbeads. The displacement of microbeads relative to the reference positions was tracked using PIVlab with a Particle Imaging Velocimetry (PIV) interrogation window size of 16 × 16 pixels and an overlap of 50%. We then obtained traction forces of rotating CTs from bead displacements using a Fiji plugin FTTC (*65*) with a regularization parameter of 9×10^{-9}.

To determine the elasticity of Matrigel and soft silicon, AFM measurements were performed on a JPK NanoWizard III AFM that was mounted on a Zeiss Axio Observer.Z1 optical microscope. Before the measurement, Bruker MLCT-SPH-5UM DC colloidal probes with a tip radius of 5.5 µm were calibrated according to the SNAP method. Force-mapping covering 90 µm² arrays of 8 x 8 force curves was performed on the samples. Tip velocity was set to 2 µm/s and force threshold to 10 nN. Data were recorded using the JPK 6.3.43 version, and analyzed with Hertz model using the corresponding data processing software. Gel elasticities are presented as the mean ± S.E.M in the results.

Image analysis

To convert 3D *z*-stack images of MDCK CTs into 2D projections, we used a Fiji macro described previously (*64*). In brief, background subtraction was performed to reduce signal-to-noise ratio. The *z*-stack images were then re-sliced to project the *xz*-plane for the circular cross-section of MDCK CTs. After, a circle was fit to the circumference of the *t-/f*-CTs and their perimeters were mapped into to a line, which was straightened and re-sliced again to obtain a 2D projection of virtually opened *t-/f*-CTs. The circumferences of MDCK CTs became the new azimuthal (*a-*) axis and the length became the new longitudinal (*l-*) axis.

For analysis of cell velocity, we performed PIV mapping with PIVlab (a tool implemented using Matlab R2020) on the obtained 2D time-lapse projections of MDCK H1-GFP 3D movies (*21, 64*).

Nuclei movements were used to match those of the cells. Interrogation windows of 64×64 and 32×32 pixels with a 50% overlapping were applied. Outlier vectors in the acquired mapping were manually removed and a local standard deviation filter was used. With these settings, we calculated the velocity components in the longitudinal $(\overrightarrow{V_z})$ and azimuthal $(\overrightarrow{V_\theta})$ directions and the velocity correlation length, ξ, was calculated using a formula described previously (*66*).

To analyze actin filaments/β-catenin finger alignment in MDCK CTs, we calculated orientation of each filament/finger using OrientationJ (*67*), a plugin of Fiji. Similarly, we manually lined out cell peripheries in rotating CTs, applied an ellipsoidal fit and measured their orientations using OrientationJ. The obtained data were plotted with rose diagrams using Matlab R2020.

Statistical Analysis
Statistical analysis was performed using GraphPad Prism (version 7.00) or Microsoft Excel. All P values were derived from Student's t-tests comparing two groups using unpaired two-tailed analysis with Welch's correction or paired two-tailed t-tests, unless otherwise noted. Error bars denote the s.d. Statistical significance was defined as P< 0.05 with regard to the null hypothesis. (*26, 68-83*)

References
1. S. L. Haigo, D. Bilder, Global tissue revolutions in a morphogenetic movement controlling elongation. *Science* **331**, 1071-1074 (2011).
2. M. Cetera, G. R. Ramirez-San Juan, P. W. Oakes, L. Lewellyn, M. J. Fairchild, G. Tanentzapf, M. L. Gardel, S. Horne-Badovinac, Epithelial rotation promotes the global alignment of contractile actin bundles during Drosophila egg chamber elongation. *Nat. Commun.* **5**, 5511 (2014).
3. A. Popkova, O. J. Stone, L. Chen, X. Qin, C. Liu, J. Liu, K. Belguise, D. J. Montell, K. M. Hahn, M. Rauzi, X. Wang, A Cdc42-mediated supracellular network drives polarized forces and Drosophila egg chamber extension. *Nat. Commun.* **11**, 1921 (2020).
4. K. Sato, T. Hiraiwa, E. Maekawa, A. Isomura, T. Shibata, E. Kuranaga, Left–right asymmetric cell intercalation drives directional collective cell movement in epithelial morphogenesis. *Nat. Commun.* **6**, 10074 (2015).
5. K. Tanner, H. Mori, R. Mroue, A. Bruni-Cardoso, M. J. Bissell, Coherent angular motion in the establishment of multicellular architecture of glandular tissues. *Proc. Natl. Acad. Sci. U.S.A* **109**, 1973-1978 (2012).
6. P. A. Fernández, B. Buchmann, A. Goychuk, L. K. Engelbrecht, M. K. Raich, C. H. Scheel, E. Frey, A. R. Bausch, Surface-tension-induced budding drives alveologenesis in human mammary gland organoids. *Nat. Phys.* **17**, 1130-1136 (2021).
7. J. Zhang, K. F. Goliwas, W. Wang, P. V. Taufalele, F. Bordeleau, C. A. Reinhart-King, Energetic regulation of coordinated leader–follower dynamics during collective invasion of breast cancer cells. *Proc. Natl. Acad. Sci. U.S.A* **116**, 7867-7872 (2019).
8. H. Wang, S. Lacoche, L. Huang, B. Xue, S. K. Muthuswamy, Rotational motion during three-dimensional morphogenesis of mammary epithelial acini relates to laminin matrix assembly. *Proc. Natl. Acad. Sci. U.S.A* **110**, 163-168 (2013).
9. P. Rørth, Fellow travellers: emergent properties of collective cell migration. *EMBO reports* **13**, 984-991 (2012).
10. S. Jain, V. M. L. Cachoux, G. H. N. S. Narayana, S. de Beco, J. D'Alessandro, V. Cellerin, T. Chen, M. L. Heuzé, P. Marcq, R.-M. Mège, A. J. Kabla, C. T. Lim, B. Ladoux, The role of single-cell mechanical behaviour and polarity in driving collective cell migration. *Nat. Phys.* **16**, 802-809 (2020).

11. R. Mayor, S. Etienne-Manneville, The front and rear of collective cell migration. *Nat. Rev. Mol. Cell Biol.* **17**, 97-109 (2016).

12. B. Ladoux, R.-M. Mège, Mechanobiology of collective cell behaviours. *Nat. Rev. Mol. Cell Biol.* **18**, 743-757 (2017).

13. M. Reffay, L. Petitjean, S. Coscoy, E. Grasland-Mongrain, F. Amblard, A. Buguin, P. Silberzan, Orientation and Polarity in Collectively Migrating Cell Structures: Statics and Dynamics. *Biophys. J.* **100**, 2566-2575 (2011).

14. R. Farooqui, G. Fenteany, Multiple rows of cells behind an epithelial wound edge extend cryptic lamellipodia to collectively drive cell-sheet movement. *J. Cell Sci.* **118**, 51-63 (2005).

15. D. J. Montell, Morphogenetic Cell Movements: Diversity from Modular Mechanical Properties. *Science* **322**, 1502-1505 (2008).

16. X. Trepat, M. R. Wasserman, T. E. Angelini, E. Millet, D. A. Weitz, J. P. Butler, J. J. Fredberg, Physical forces during collective cell migration. *Nat. Phys.* **5**, 426-430 (2009).

17. F. Peglion, F. Llense, S. Etienne-Manneville, Adherens junction treadmilling during collective migration. *Nat. Cell Biol.* **16**, 639-651 (2014).

18. K. M. Sherrard, M. Cetera, S. Horne-Badovinac, DAAM mediates the assembly of long-lived, treadmilling stress fibers in collectively migrating epithelial cells in *Drosophila*. *bioRxiv*, 2021.2008.2007.455521 (2021).

19. T. Chen, A. Callan-Jones, E. Fedorov, A. Ravasio, A. Brugués, H. T. Ong, Y. Toyama, B. C. Low, X. Trepat, T. Shemesh, R. Voituriez, B. Ladoux, Large-scale curvature sensing by directional actin flow drives cellular migration mode switching. *Nat. Phys.* **15**, 393-402 (2019).

20. Y. Y. Biton, S. A. Safran, The cellular response to curvature-induced stress. *Physical Biology* **6**, 046010 (2009).

21. W. Xi, S. Sonam, T. Beng Saw, B. Ladoux, C. Teck Lim, Emergent patterns of collective cell migration under tubular confinement. *Nat. Commun.* **8**, 1517 (2017).

22. H. G. Yevick, G. Duclos, I. Bonnet, P. Silberzan, Architecture and migration of an epithelium on a cylindrical wire. *Proc. Natl. Acad. Sci. U.S.A* **112**, 5944-5949 (2015).

23. Y. Maroudas-Sacks, L. Garion, L. Shani-Zerbib, A. Livshits, E. Braun, K. Keren, Topological defects in the nematic order of actin fibres as organization centres of Hydra morphogenesis. *Nat. Phys.* **17**, 251-259 (2021).

24. M. Gupta, B. R. Sarangi, J. Deschamps, Y. Nematbakhsh, A. Callan-Jones, F. Margadant, R.-M. Mège, C. T. Lim, R. Voituriez, B. Ladoux, Adaptive rheology and ordering of cell cytoskeleton govern matrix rigidity sensing. *Nat. Commun.* **6**, 7525 (2015).

25. D. J. G. Pearce, S. Gat, G. Livne, A. Bernheim-Groswasser, K. Kuruse, Defect-driven shape transitions in elastic active nematic shells. *arXiv*, 10.48550/ARXIV.42010.13141 (2020).

26. L. A. Hoffmann, L. N. Carenza, J. Eckert, L. Giomi, Theory of defect-mediated morphogenesis. *Sci. Adv.* **8**, eabk2712 (2022).

27. I. Nitschke, S. Reuther, A. Voigt, Liquid crystals on deformable surfaces. *Proceedings of the Royal Society A: Mathematical, Physical and Engineering Sciences* **476**, 20200313 (2020).

28. A. S. Chin, K. E. Worley, P. Ray, G. Kaur, J. Fan, L. Q. Wan, Epithelial Cell Chirality Revealed by Three-Dimensional Spontaneous Rotation. *Proc. Natl. Acad. Sci. U.S.A* **115**, 12188-12193 (2018).

29. D. T. Tambe, C. Corey Hardin, T. E. Angelini, K. Rajendran, C. Y. Park, X. Serra-Picamal, E. H. Zhou, M. H. Zaman, J. P. Butler, D. A. Weitz, J. J. Fredberg, X. Trepat, Collective cell guidance by cooperative intercellular forces. *Nature Materials* **10**, 469 (2011).

30. P. Leroy, K. E. Mostov, Slug is required for cell survival during partial epithelial-mesenchymal transition of HGF-induced tubulogenesis. *Molecular biology of the cell* **18**, 1943-1952 (2007).

31. T. Hirashima, M. Hoshuyama, T. Adachi, In vitro tubulogenesis of Madin-Darby canine kidney (MDCK) spheroids occurs depending on constituent cell number and scaffold gel concentration. *J Theor Biol* **435**, 110-115 (2017).

32. S. Horne-Badovinac, D. Bilder, Mass transit: Epithelial morphogenesis in the Drosophila egg chamber. *Developmental Dynamics* **232**, 559-574 (2005).

33. A. Doostmohammadi, S. P. Thampi, T. B. Saw, C. T. Lim, B. Ladoux, J. M. Yeomans, Celebrating Soft Matter's 10th Anniversary: Cell division: a source of active stress in cellular monolayers. *Soft Matter* **11**, 7328-7336 (2015).

34. R. W. Naylor, H.-H. G. Chang, S. Qubisi, A. J. Davidson, A novel mechanism of gland formation in zebrafish involving transdifferentiation of renal epithelial cells and live cell extrusion. *eLife* **7**, e38911 (2018).

35. F. Martin-Belmonte, K. Mostov, Regulation of cell polarity during epithelial morphogenesis. *Current Opinion in Cell Biology* **20**, 227-234 (2008).

36. J. d'Alessandro, A. Barbier--Chebbah, V. Cellerin, O. Benichou, R. M. Mège, R. Voituriez, B. Ladoux, Cell migration guided by long-lived spatial memory. *Nat. Commun.* **12**, 4118 (2021).

37. S. R. K. Vedula, M. C. Leong, T. L. Lai, P. Hersen, A. J. Kabla, C. T. Lim, B. Ladoux, Emerging modes of collective cell migration induced by geometrical constraints. *Proc. Natl. Acad. Sci. U.S.A* **109**, 12974-12979 (2012).

38. L. Balasubramaniam, A. Doostmohammadi, T. B. Saw, G. H. N. S. Narayana, R. Mueller, T. Dang, M. Thomas, S. Gupta, S. Sonam, A. S. Yap, Y. Toyama, R.-M. Mège, J. M. Yeomans, B. Ladoux, Investigating the nature of active forces in tissues reveals how contractile cells can form extensile monolayers. *Nature Materials* **20**, 1156-1166 (2021).

39. R. Sunyer, V. Conte, J. Escribano, A. Elosegui-Artola, A. Labernadie, L. Valon, D. Navajas, J. M. García-Aznar, J. J. Muñoz, P. Roca-Cusachs, X. Trepat, Collective cell durotaxis emerges from long-range intercellular force transmission. *Science* **353**, 1157-1161 (2016).

40. W. Xi, T. B. Saw, D. Delacour, C. T. Lim, B. Ladoux, Material approaches to active tissue mechanics. *Nat. Rev. Mater.* **4**, 23-44 (2019).

41. A. Ravasio, I. Cheddadi, T. Chen, T. Pereira, H. T. Ong, C. Bertocchi, A. Brugues, A. Jacinto, A. J. Kabla, Y. Toyama, X. Trepat, N. Gov, L. Neves de Almeida, B. Ladoux, Gap geometry dictates epithelial closure efficiency. *Nat. Commun.* **6**, 7683 (2015).

42. M. Luciano, S.-L. Xue, W. H. De Vos, L. Redondo-Morata, M. Surin, F. Lafont, E. Hannezo, S. Gabriele, Cell monolayers sense curvature by exploiting active mechanics and nuclear mechanoadaptation. *Nat. Phys.*, (2021).

43. L. Pieuchot, J. Marteau, A. Guignandon, T. Dos Santos, I. Brigaud, P.-F. Chauvy, T. Cloatre, A. Ponche, T. Petithory, P. Rougerie, M. Vassaux, J.-L. Milan, N. Tusamda Wakhloo, A. Spangenberg, M. Bigerelle, K. Anselme, Curvotaxis directs cell migration through cell-scale curvature landscapes. *Nat. Commun.* **9**, 3995 (2018).

44. P. Rougerie, L. Pieuchot, R. S. dos Santos, J. Marteau, M. Bigerelle, P.-F. Chauvy, M. Farina, K. Anselme, Topographical curvature is sufficient to control epithelium elongation. *Sci. Rep.* **10**, 14784 (2020).

45. S.-M. Yu, J. M. Oh, J. Lee, W. Lee-Kwon, W. Jung, F. Amblard, S. Granick, Y.-K. Cho, Substrate curvature affects the shape, orientation, and polarization of renal epithelial cells. *Acta Biomaterialia* **77**, 311-321 (2018).

46. I. D. Johnston, D. K. McCluskey, C. K. L. Tan, M. C. Tracey, Mechanical characterization of bulk Sylgard 184 for microfluidics and microengineering. *Journal of Micromechanics and Microengineering* **24**, 035017 (2014).

47. L. Lu, S. J. Oswald, H. Ngu, F. C. Yin, Mechanical properties of actin stress fibers in living cells. *Biophys J* **95**, 6060-6071 (2008).

48. C. S. Chen, J. Tan, J. Tien, Mechanotransduction at Cell-Matrix and Cell-Cell Contacts. *Annual Review of Biomedical Engineering* **6**, 275-302 (2004).

49. M. Bienz, β-Catenin: A Pivot between Cell Adhesion and Wnt Signalling. *Current Biology* **15**, R64-R67 (2005).

50. K. A. Knudsen, A. P. Soler, K. R. Johnson, M. J. Wheelock, Interaction of alpha-actinin with the cadherin/catenin cell-cell adhesion complex via alpha-catenin. *J. Cell Biol.* **130**, 67-77 (1995).

51. S. Yonemura, Y. Wada, T. Watanabe, A. Nagafuchi, M. Shibata, α-catenin as a tension transducer that induces adherens junction development. *Nat Cell Biol* **12**, (2010).

52. M. Rauzi, P. Verant, T. Lecuit, P.-F. Lenne, Nature and anisotropy of cortical forces orienting Drosophila tissue morphogenesis. *Nat. Cell Biol.* **10**, 1401-1410 (2008).

53. K. Matsuzawa, T. Himoto, Y. Mochizuki, J. Ikenouchi, α-Catenin Controls the Anisotropy of Force Distribution at Cell-Cell Junctions during Collective Cell Migration. *Cell Rep* **23**, 3447-3456 (2018).

54. W. Y. Wang, C. D. Davidson, D. Lin, B. M. Baker, Actomyosin contractility-dependent matrix stretch and recoil induces rapid cell migration. *Nat. Commun.* **10**, 1186 (2019).

55. S. Jain, B. Ladoux, R. M. Mège, Mechanical plasticity in collective cell migration. *Curr Opin Cell Biol* **72**, 54-62 (2021).

56. C. Blanch-Mercader, R. Vincent, E. Bazellières, X. Serra-Picamal, X. Trepat, J. Casademunt, Effective viscosity and dynamics of spreading epithelia: a solvable model. *Soft Matter* **13**, 1235-1243 (2017).

57. K. Kruse, J. F. Joanny, F. Jülicher, J. Prost, K. Sekimoto, Generic theory of active polar gels: a paradigm for cytoskeletal dynamics. *The European Physical Journal E* **16**, 5-16 (2005).

58. F. Jülicher, K. Kruse, J. Prost, J. F. Joanny, Active behavior of the Cytoskeleton. *Physics Reports* **449**, 3-28 (2007).

59. M. Poujade, E. Grasland-Mongrain, A. Hertzog, J. Jouanneau, P. Chavrier, B. Ladoux, A. Buguin, P. Silberzan, Collective migration of an epithelial monolayer in response to a model wound. *Proc. Natl. Acad. Sci. U.S.A* **104**, 15988-15993 (2007).

60. T. E. Angelini, E. Hannezo, X. Trepat, M. Marquez, J. J. Fredberg, D. A. Weitz, Glass-like dynamics of collective cell migration. *Proc. Natl. Acad. Sci. U.S.A* **108**, 4714-4719 (2011).

61. J. M. López-Gay, H. Nunley, M. Spencer, F. d. Pietro, B. Guirao, F. Bosveld, O. Markova, I. Gaugue, S. Pelletier, D. K. Lubensky, Y. Bellaïche, Apical stress fibers enable a scaling between cell mechanical response and area in epithelial tissue. *Science* **370**, eabb2169 (2020).

62. P. Haas, D. Gilmour, Chemokine signaling mediates self-organizing tissue migration in the zebrafish lateral line. *Dev Cell* **10**, 673-680 (2006).

63. Q. Guo, B. Xia, S. Moshiach, C. Xu, Y. Jiang, Y. Chen, Y. Sun, J. M. Lahti, X. A. Zhang, The microenvironmental determinants for kidney epithelial cyst morphogenesis. *European journal of cell biology* **87**, 251-266 (2008).

64. W. Xi, S. Sonam, C. T. Lim, B. Ladoux, in *Methods in Cell Biology,* J. Doh, D. Fletcher, M. Piel, Eds. (Academic Press, 2018), vol. 146, pp. 3-21.

65. Q. Tseng, E. Duchemin-Pelletier, A. Deshiere, M. Balland, H. Guillou, O. Filhol, M. Théry, Spatial organization of the extracellular matrix regulates cell–cell junction positioning. *Proc. Natl. Acad. Sci. U.S.A* **109**, 1506-1511 (2012).
66. L. Petitjean, M. Reffay, E. Grasland-Mongrain, M. Poujade, B. Ladoux, A. Buguin, P. Silberzan, Velocity fields in a collectively migrating epithelium. *Biophys. J.* **98**, 1790-1800 (2010).
67. Z. Püspöki, M. Storath, D. Sage, M. Unser, Transforms and Operators for Directional Bioimage Analysis: A Survey. *Advances in anatomy, embryology, and cell biology* **219**, 69-93 (2016).
68. G. Napoli, L. Vergori, Extrinsic Curvature Effects on Nematic Shells. *Phys. Rev. Lett.* **108**, 207803 (2012).
69. G. Napoli, L. Vergori, Surface free energies for nematic shells. *Physical Review E* **85**, 061701 (2012).
70. A. Segatti, M. Snarski, M. Veneroni, Equilibrium configurations of nematic liquid crystals on a torus. *Physical Review E* **90**, 012501 (2014).
71. D. Jesenek, S. Kralj, R. Rosso, E. G. Virga, Defect unbinding on a toroidal nematic shell. *Soft Matter* **11**, 2434-2444 (2015).
72. I. Nitschke, M. Nestler, S. Praetorius, H. Löwen, A. Voigt, Nematic liquid crystals on curved surfaces: a thin film limit. *Proceedings of the Royal Society A: Mathematical, Physical and Engineering Sciences* **474**, 20170686 (2018).
73. M. Nestler, I. Nitschke, S. Praetorius, A. Voigt, Orientational Order on Surfaces: The Coupling of Topology, Geometry, and Dynamics. *Journal of Nonlinear Science* **28**, 147-191 (2018).
74. M. Nestler, I. Nitschke, H. Löwen, A. Voigt, Properties of surface Landau–de Gennes Q-tensor models. *Soft Matter* **16**, 4032-4042 (2020).
75. D. J. G. Pearce, P. W. Ellis, A. Fernandez-Nieves, L. Giomi, Geometrical Control of Active Turbulence in Curved Topographies. *Phys. Rev. Lett.* **122**, 168002 (2019).
76. D. J. G. Pearce, Defect order in active nematics on a curved surface. *New Journal of Physics* **22**, 063051 (2020).
77. D. Khoromskaia, G. Salbreux, Active morphogenesis of patterned epithelial shells. *arXiv*, arXiv:2111.12820 (2021).
78. M. Nestler, A. Voigt, Active nematodynamics on curved surfaces -- the influence of geometric forces on motion patterns of topological defects. *arXiv*, arXiv:2107.07779 (2021).
79. G. Salbreux, F. Jülicher, J. Prost, A. Callan-Jones, Theory of nematic and polar active fluid surfaces. *arXiv*, arXiv:2201.09251 (2022).
80. S. Bell, S.-Z. Lin, J.-F. Rupprecht, J. Prost, Active nematic flows on curved surfaces. *arXiv*, arXiv:2203.05644 (2022).
81. P. G. de Gennes, J. Prost, *The Physics of Liquid Crystals*. (Clarendon Press, 1993).
82. M. Nestler, I. Nitschke, A. Voigt, A finite element approach for vector- and tensor-valued surface PDEs. *Journal of Computational Physics* **389**, 48-61 (2019).
83. M. C. Marchetti, J. F. Joanny, S. Ramaswamy, T. B. Liverpool, J. Prost, M. Rao, R. A. Simha, Hydrodynamics of soft active matter. *Reviews of Modern Physics* **85**, 1143-1189 (2013).

Acknowledgments

Author contributions:
Conceptualization: WX, BL, JP
Methodology: WX, BL, AG, JP, CBM, TBS, CTL
Investigation: AG, CBM, WX, DD, LB, SJ, FL, AD, BD
Analysis: AG, LB, CBM, WX, JdA, TBS
Visualization: AG, WX, CBM
Supervision: WX, BL, JP
Writing—original draft: AG, CBM, WX
Writing—review & editing: WX, BL, JP, CBM

Competing interests: Authors declare that they have no competing interests.

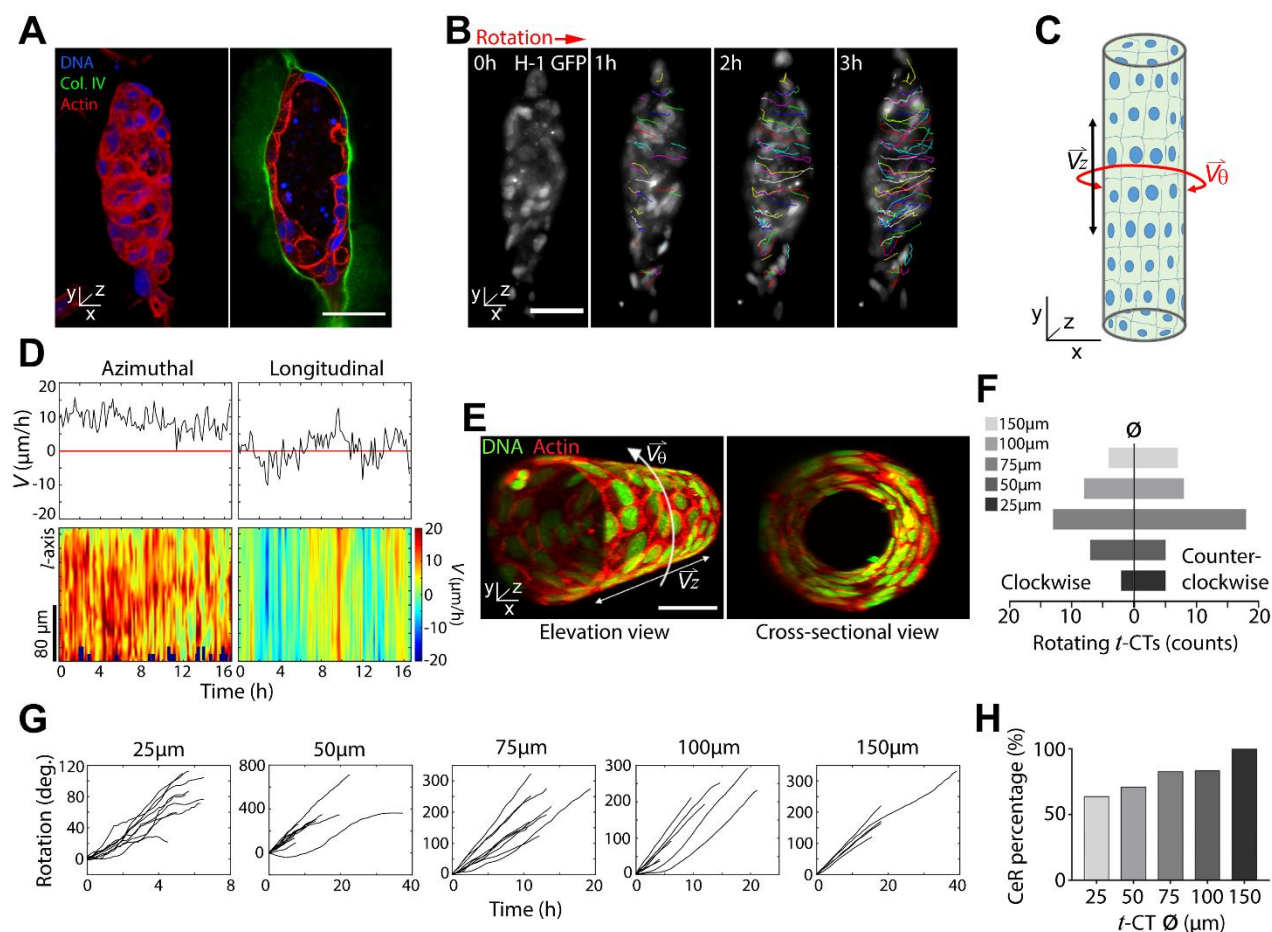**Data and materials availability:** All data needed to evaluate the conclusions in the paper are present in the paper and/or the Supplementary Materials.

1058

1059

1060

1061

1062

1063

1064

1065

1066

1067

1068

1069

1070

1071

1072

1073

1074

1075

1076

1077

1078

1079

1080

1081

1082

1083

1084

1085

1086

1087

1088

1089

1090

1091

1092

Figures

Fig. 1. Whole-tissue collective rotation in 3D concave cylindrical epithelia. (**A**) Images of a histone 1-GFP (H1-GFP) MDCK duct inside Matrigel at different *z*-positions. Left: view from top, right: cross-sectional view, revealing hollow lumen inside the structure. H1-GFP nuclei are colored in blue, actin (phalloidin) in red and collagen type IV in green. (**B**) Time-lapsed images showing the circumferential rotation of the MDCK duct from (**A**). Single-cell trajectories are shown as varying colored lines. Red arrow indicates rotational direction. (**C**) Schematic representation of a confluent MDCK tubular cylindrical tissue (*t*-CT) with collective movements with longitudinal ($\overrightarrow{V_z}$) and azimuthal ($\overrightarrow{V_\theta}$) velocities. The symbols were used to match the conventional terminology to describe a cylindrical system. (**D**) Graphs (top panel) and kymographs (bottom panel) displaying the average velocities (*V*) of the MDCK duct from (**A**) in azimuthal and longitudinal directions as a function of time. *V* is calculated using particle imaging velocimetry (PIV) analysis. The graphs then plot the average azimuthal and longitudinal component of *V* for each time point, reflecting the average movement of the whole duct. The kymographs demonstrate spatial average $\overrightarrow{V_\theta}$ and $\overrightarrow{V_z}$ along the *l*-axis for every time point for entire observation period, thus showing spatiotemporal distribution of local velocities. (**E**) Representative 3D reconstructed images of an MDCK *t*-CT with $\emptyset = 100$ μm. Actin, red and nuclei, green (H-1 GFP). White arrows show either $\overrightarrow{V_\theta}$ or $\overrightarrow{V_z}$. (**F**) Graphs representing counts of clockwise and counter-clockwise rotating *t*-CTs of varying diameters. (**G**) Graphs representing average nucleus angular displacements of *t*-CTs with different sizes. Each line in each graph represents a *t*-CT. (**H**) Graph showing the percentage of CeR events observed in *t*-CTs of different diameters ($n = 11$–29 for each condition). Scale bars, 50μm.
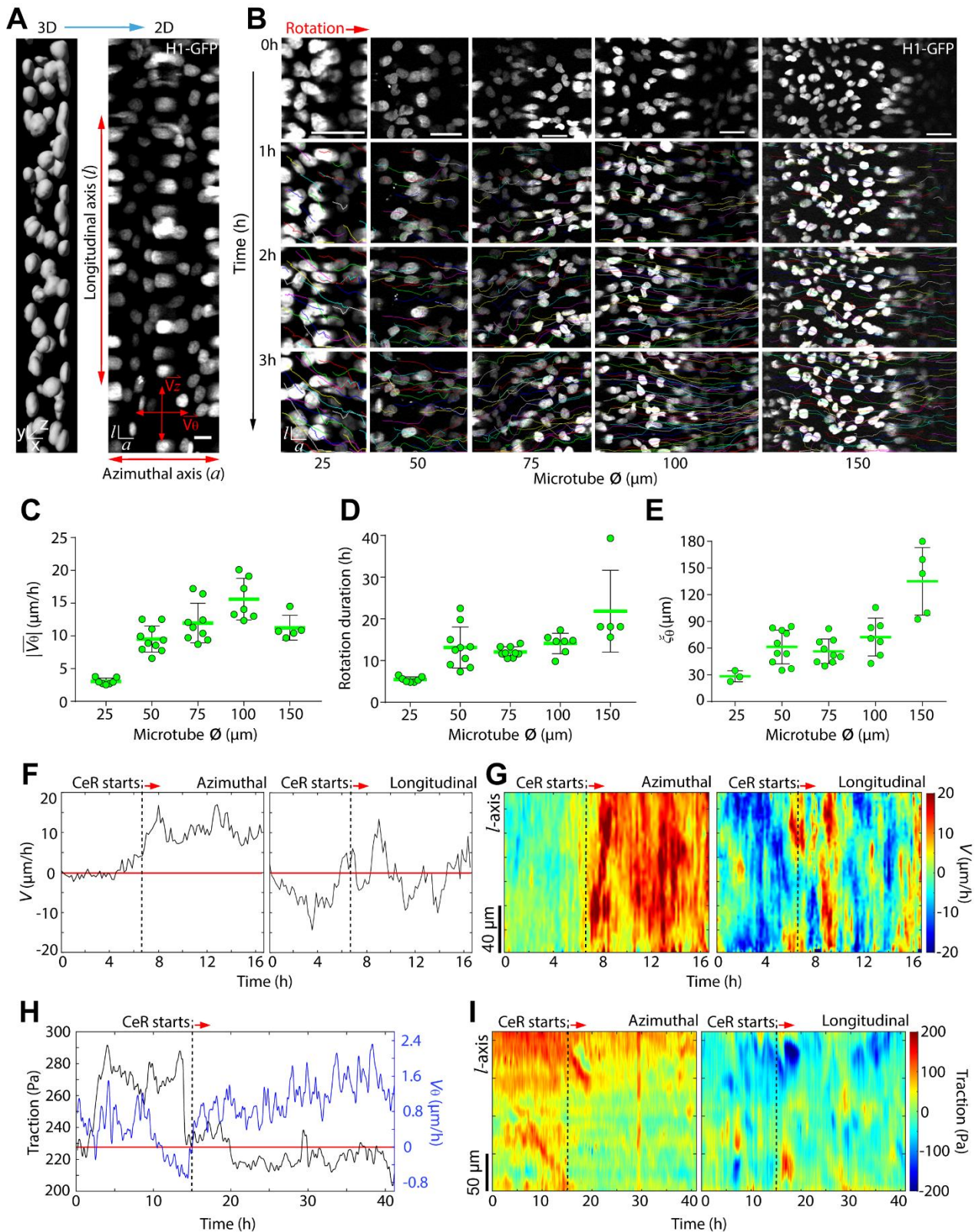
1118
Fig. 2. Characteristics of epithelial tissue rotation inside microtubes. (**A**) Transform of a 3D *t*-
CT into a 2D projection for analysis. The azimuthal and longitudinal velocity vectors are shown in
red. Scale bar, 20 μm. (**B**) Cropped time-lapse 2D projections of rotating H1-GFP MDCK *t*-CT of
different sizes. Tracking individual cell nuclei shows cell trajectories as parallel colored lines. Scale
bars, 50μm. (**C**) – (**E**) Graphs showing absolute average azimuthal velocities ($|\overline{V_\theta}|$) (**C**), CeR
duration (**D**) and $\overrightarrow{V_\theta}$ correlation length (ξ_θ) (**E**) in different *t*-CTs ($n = 3$-10 for each condition). Data
presented as individual values with mean ± s.d. (**F**) and (**G**) Representative graphs (**F**) and

kymographs (**G**) showing average velocity of a t-CT with $\emptyset = 75$ µm in azimuthal and longitudinal direction and spatial distribution along l-axis as a function of time. (**H**) Graph presenting the average traction force (T – black line) applied by a t-CT of $\emptyset = 75$ µm together with average V_θ (blue line) evolving with time. (**I**) Kymographs showing spatial distribution of average traction from (**H**) exerted azimuthally (T_θ) or longitudinally (T_z) along l-axis as a function of time. In (**F**) – (**I**), vertical black dash lines and red arrows denote onset of CeR.
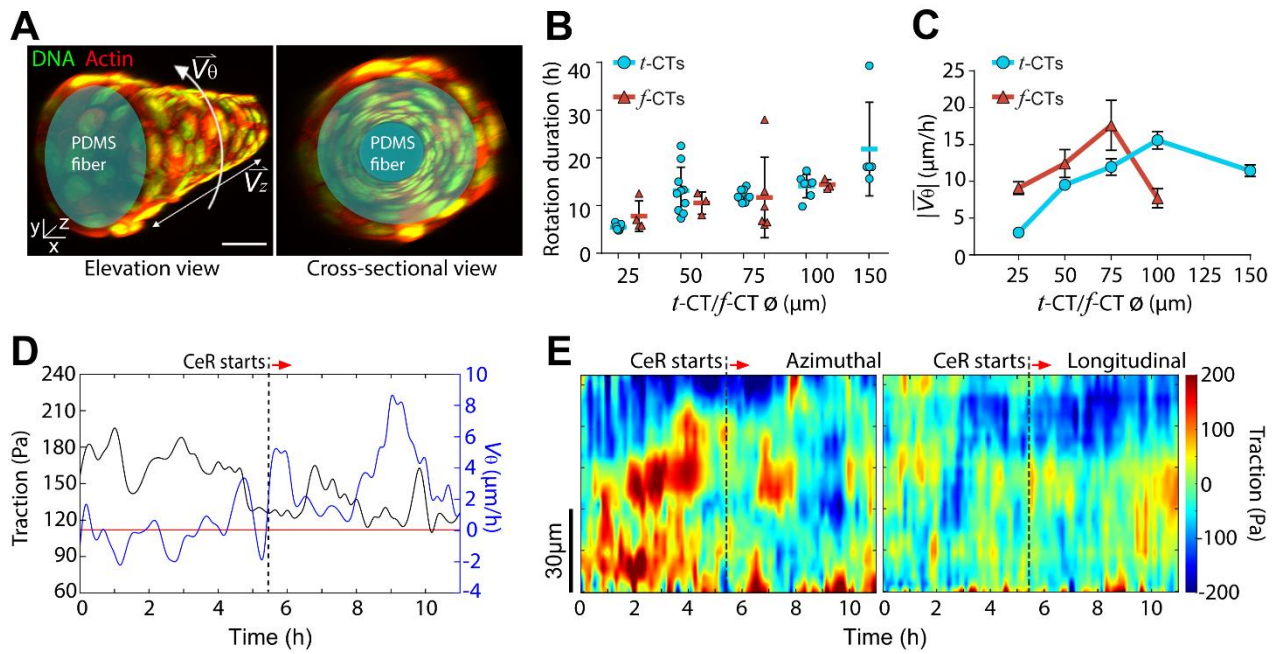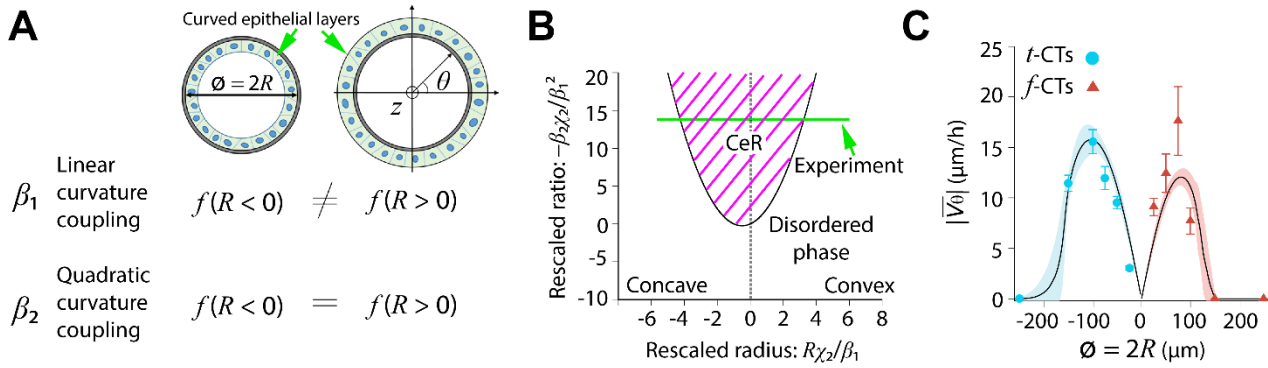
Fig. 3. Convex CTs show collective cell rotation. (**A**) Representative 3D reconstructed images of H1-GFP MDCK cells on Ø = 100 μm PDMS microfiber (marked by teal) showing a convexly curved *f*-CT. Actin, red and nuclei, green (H1-GFP). White arrows show either $\overrightarrow{V_\theta}$ or $\overrightarrow{V_z}$. Scale bar, 50 μm. (**B**) Graph displaying CeR duration of different *t*-CTs (aqua) and *f*-CTs (red). Data presented as individual values with mean ± s.d. (**C**) Graph showing $|\overline{V_\theta}|$ of different *t*-CTs (aqua) and *f*-CTs (red). Data presented as mean ± s.d. n = 5-10 (*t*-CTs) and n = 3-8 (*f*-CTs) for each diameter. (**D**) Graph presenting the average magnitude of traction (black line) applied by an *f*-CT on a Ø = 75 μm soft silicone fiber together with average azimuthal velocity (blue line) as a function of time. (**E**) Kymographs showing time-evolving average T_θ and T_z from (**D**) along *l*-axis. In (**D**) and (**E**), vertical black dash lines and red arrows indicate onset of CeR.
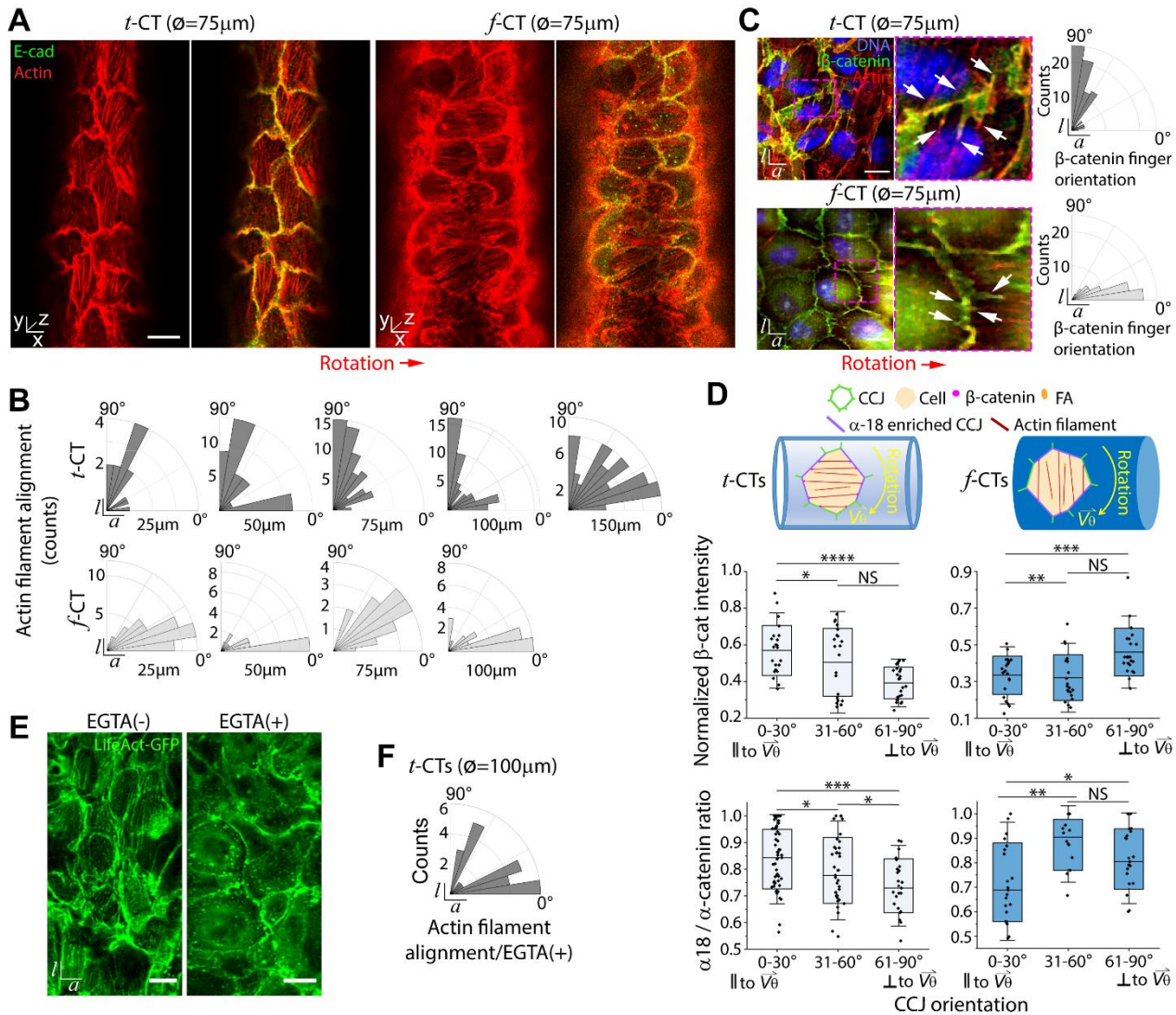
Fig. 4. Different organizations of actin cytoskeleton and cell-cell junction according to tissue curvatures. (**A**) Representative 3D reconstructed images of rotating MDCK *t*-CTs and *f*-CTs showing large-scale long-range basal actin filaments orienting in different directions. Actin, red and E-cadherin, green. (**B**) Rose diagrams of actin filament orientation in CTs of varying diameters (*n* = 13 – 75). (**C**) 2D projections of a *t*-CT (top panel) and a *f*-CT (bottom panel) showing detail features of cell-cell junctions (CCJs) in different orientations. White arrows indicate actin filaments overlapping with β-catenin fingers. Magenta dash boxes indicate zoom-in regions. Rose diagrams on the right showing orientation of β-catenin fingers at CCJs (*n* = 88 for *t*-CTs and *n* = 65 for *f*-CTs) with respect to the azimuthal axis. (**D**) Upper panel: schematic representation of actin alignment and distribution of β-catenin and α-18 enriched CCJs in *t*-CTs and *f*-CTs. Actin filaments may attach to CCJs via β-catenin and substrate via focal adhesion (FA). Middle and bottom panels: Normalized β-catenin fluorescent intensity (middle panel, *n* = 68 for *t*-CTs and *n* = 65 for *f*-CTs) and fluorescent intensity ratio of unfolded α-catenin (α-18) over total α-catenin (bottom panel, *n* = 115 for *t*-CTs and *n* = 50 for *f*-CTs) in various oriented CCJs. The relative angles between CCJs and CeR direction (i.e., relative to *a*-axis) were presented in *x*-axis. Data are shown as individual values overlapped with box charts showing mean ± s.d. (coef = 1 for the box and coef = 1.5 for the whiskers). (**E**) 2D fluorescent projections showing organization of actin (LifeAct-GFP) in a *t*-CT with Ø = 100μm before and after EGTA treatment. (**F**) Rose diagram showing actin filament orientation in *t*-CTs with Ø = 100μm after EGTA treatment (*n* = 26).
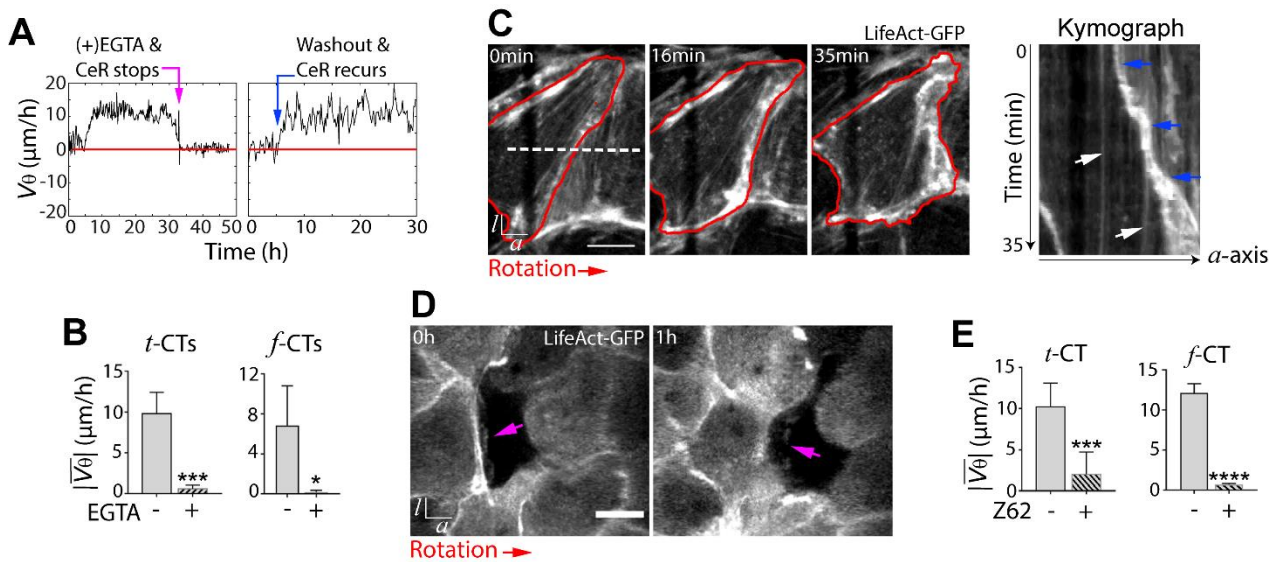
1225

Fig. 5. Roles of cell-cell adhesions and cell polarity in rotating CTs. (**A**) Graphs showing EGTA treatment ceased CeR ($V_\theta \approx 0$, magenta arrow) and CeR recurrence (blue arrow) after washout. (**B**) Plots presenting $|\overline{V_\theta}|$ for different rotating CTs before and after EGTA treatment ($n = 4$ for all cases). (**C**) 2D time-lapse (15s per frame) projections demonstrating actin dynamics of a t-CT ($\varnothing = 100\mu m$) expressing LifeAct-GFP during CeR. Cell periphery is drawn in red. Kymograph on the right was obtained by re-slicing along white dash line (0 min). White arrows indicate trajectories of immobile long-range actin filaments and blue arrows show displacement of cell front with respect to a-axis. (**D**) 2D time-lapse projections demonstrating actin-based cryptic protrusion of a rotating t-CT ($\varnothing = 100\mu m$) consisting of wild-type and LifeAct-GFP MDCKs. Magenta arrows denote lamellipodial protrusions of a LifeAct-GFP-expressing cell towards a wild-type (unmarked) cell. (**E**) Graphs presenting $|\overline{V_\theta}|$ for different rotating CTs before and after Z62 treatment ($n = 6$ for t-CTs and $n = 3$ for f-CTs). Student's t-test, NS non-significant, * P < 0.05, ** P < 0.01, *** P < 0.001, **** P < 0.0001. In (**B**) and (**E**), data are presented as mean ± s.d. Red arrows indicate rotation direction. Scale bars, 20μm.

1240
1241
1242
1243
1244
1245
1246
1247
1248
1249
1250
1251
1252
1253
1254
1255
1256
1257
1258
1259
1260

Fig. 6. An active-polar-gel description for 3D collective tissue rotation and polarization. (**A**) Schematic representation of cross-sectional views of a cell monolayer that lays on either the inner (left, i.e., *t*-CT) or outer (right, i.e., *f*-CT) side of a cylindrical substrate (dark gray). Couplings linear to the curvature (β_1) distinguish between both configurations, whereas couplings quadratic to the curvature (β_2) do not. The free-energy density f is given by Eq. (1). We use the convention that $R < 0$ for microtubes (*t*-CT) and $R > 0$ for microfibers (*f*-CT). In this framework, z and θ denote the longitudinal direction and the azimuthal direction of the cylindrical substrate. (**B**) Phase diagram of steady-state uniform solutions as a function of the rescaled substrate radius $R\chi_2/\beta_1$ and the effective parameter $-\beta_2\chi_2/\beta_1^2$. The two solutions (separated by the black parabola) correspond to a disordered phase and a collective rotating phase (indicated by magenta slash shaded area). In our experiments, we sample the *x*-axis of the phase-diagram by varying the radius of micro-tubes/-fibers, R. The parameter region that fits best the experimental velocity curves from (**C**) is indicated by the green line parallel to the *x*-axis. To sample the *y*-axis, one can alter intrinsic epithelial properties, such as enhancing/weakening cell-cell adhesions and cell-substrate adhesion. (**C**) Graph showing azimuthal velocity as a function of CT's diameter. The circular aqua and triangular red dots correspond to the experimental measurements of the azimuthal velocity from (Fig. 3C). The dark curves and shaded aqua/red areas represent the mean ± s.d. of the azimuthal velocity given by Eq. (2) for the subset of parameters that satisfies $\mathcal{E} < 1.1\mathcal{E}_m$, being $\mathcal{E}$ the error function given by Eq. (S29) in Theoretical Section 5 in Supplementary Materials and $\mathcal{E}_m$ the absolute minimum. Parameters $\bar{\beta}_1 = \bar{\beta}_2 = 0$.

Supplementary Materials

Supplementary Materials for this article is available at https://science.org.

Supplementary Text - Theoretical Section

Full details of mathematical description of an active-polar-fluid framework

Contents

SECTION 1: PHYSICAL DESCRIPTION OF AN ACTIVE POLAR FLUID

MDCK cell monolayers are described as a $2d$ active polar fluid with a polarization field p_α and a velocity field v_α, representing the average cell polarization and the average cell velocity, respectively. We consider that the system forms a steady-state disordered phase with $p_\alpha = 0$ and vanishing average velocity $v_\alpha = 0$ in the absence of drivings.

Previous work studied the effects of couplings between the extrinsic curvature and an orientational order on the steady-state evolution of passive liquid crystals [70–76]. This work was extended to active liquid crystals for different types of geometries like planar, cylindrical, toroidal or spherical shells, and different types of orientational order that were described by either a director vector field or a nematic tensor field [26, 77–81]. The previous studies focused on the effects of quadratic couplings between the extrinsic curvature and the orientational order parameter. Unlike to linear couplings, quadratic couplings do not differentiate between convexity/concavity of the embedding geometry. Even though linear couplings are allowed by the symmetries of some biological systems, like apico-basal polarity in cells, their effects in active liquid crystal have been only studied recently for the case of stripes with curvature in the transverse direction [82]. Here, we will study the steady-state patterns generated via the interplay between polar traction forces and linear/quadratic couplings between the extrinsic curvature and the orientational order on a cylindrical geometry.

To describe the effects of the substrate curvature, we consider that the extrinsic curvature tensor $\mathcal{C}_{\alpha\beta}$ behaves as an external field, which is coupled to p_α. The effective free-energy density of our system reads

$$\mathcal{F} = \int_{\mathcal{A}} f\, da = \int_{\mathcal{A}} \left(\frac{\chi_2}{2} p_\gamma p_\gamma + \frac{\chi_4}{4} (p_\gamma p_\gamma)^2 + \frac{\mathcal{K}}{2} (\partial_\beta p_\gamma)(\partial_\beta p_\gamma) + f_C^{(1)}(\mathcal{C}_{\alpha\beta}, p_\alpha) + f_C^{(2)}(\mathcal{C}_{\alpha\beta}, p_\alpha) \right) da.$$
(S1)

The first three terms in Eq. (S1) correspond to the Landau-Ginzburg free-energy density in the one-constant approximation [83]. The coefficients χ_2 and χ_4 are typical Landau-Ginzburg parameters, and $\mathcal{K}$ is a Frank elastic modulus associated with distortions of the polarization field. Specifically, the first and second terms in Eq. (S1) penalise configurations with a finite local order (i.e. $p_\gamma p_\gamma \neq 0$), and the third term penalises configurations with spatial gradients of the polarization field. The third term in the free-energy density is computed by taking $3D$ derivatives in cylindrical coordinates of $\partial_\beta p_\gamma$ and subsequently, summing over repeated indices. Because the analysis is restricted to cylindrical geometries and the director field is enforced to remain parallel to the surface, this term takes the expression derived in Refs. [70, 71] for a cylindrical shell. For a general discussion on the thin-film limit of this term in liquid crystal surfaces with arbitrary shapes, we refer to Ref. [84]. The

fourth and fifth terms depend explicitly on the geometry of the substrate through the extrinsic curvature tensor $C_{\alpha\beta}$. The functional $f_C^{(1)}$ includes terms linear in $C_{\alpha\beta}$, whereas $f_C^{(2)}$ includes quadratic terms in $C_{\alpha\beta}$. The third term in the free-energy density can also lead to quadratic couplings between the orientational order and the extrinsic curvature, [70, 71]. Importantly, the sign of the curvature tensor depends on whether the system sits on the inner or outer face of the substrate. Therefore, the functional $f_C^{(1)}$ changes sign upon changing the face of the substrate that the system sits on, whereas $f_C^{(2)}$ does not.

Symmetry requires that $f_C^{(1)}$ in Eq. (S1) takes the form

$$f_C^{(1)} = \frac{\beta_1}{2} C_{\alpha\beta} p_\beta p_\alpha + \frac{\overline{\beta}_1}{2} C_{\gamma\gamma} p_\alpha p_\alpha, \tag{S2}$$

and, similarly, $f_C^{(2)}$ reads

$$f_C^{(2)} = \frac{\beta_{2,1}}{2} C_{\alpha\gamma} C_{\alpha\beta} p_\beta p_\gamma + \frac{\overline{\beta}_{2,1}}{2} C_{\alpha\beta} C_{\alpha\beta} p_\gamma p_\gamma + \frac{\beta_{2,2}}{2} C_{\gamma\gamma} C_{\alpha\beta} p_\beta p_\alpha + \frac{\overline{\beta}_{2,2}}{2} C_{\alpha\alpha} C_{\beta\beta} p_\gamma p_\gamma. \tag{S3}$$

The coarse-grained interactions between cells and the underlying substrate are described by four terms: a linear viscous-like friction force ($\sim \xi v_\alpha$) with friction coefficient ξ, an active polar traction force ($\sim T_0 p_\alpha$) with amplitude T_0, and two active nematic traction forces with amplitudes λ_s and λ_b corresponding to splay and bend deformation of the polarization field. Thereby, in the overdamped limit, momentum conservation equation reduces to

$$\partial_\beta \sigma_{\alpha\beta}^t = \xi v_\alpha - T_0 p_\alpha + \lambda_s p_\alpha \partial_\beta p_\beta + \lambda_b p_\beta \partial_\beta p_\alpha, \tag{S4}$$

where the total stress tensor $\sigma_{\alpha\beta}^t$ can be decomposed in two terms $\sigma_{\alpha\beta}^t = \sigma_{\alpha\beta}^e + \sigma_{\alpha\beta}$, the first term being the Ericksen stress tensor $\sigma_{\alpha\beta}^e$ and the second term being the deviatoric stress tensor $\sigma_{\alpha\beta}$ [83]. The Ericksen stress tensor reads

$$\sigma_{\alpha\beta}^e = -P\delta_{\alpha\beta} - \frac{\partial f}{\partial(\partial_\beta p_\gamma)} \partial_\alpha p_\gamma = -P\delta_{\alpha\beta} - \mathcal{K} \partial_\beta p_\gamma \partial_\alpha p_\gamma, \tag{S5}$$

where P corresponds to the pressure field, and f the effective free-energy density given by Eq. (S1). Keeping a one-viscosity description, the deviatoric stress tensor $\sigma_{\alpha\beta}$ takes the form

$$\sigma_{\alpha\beta} = 2\eta v_{\alpha\beta} - \zeta \Delta\mu p_\alpha p_\beta + \frac{\nu}{2}(p_\alpha h_\beta + p_\beta h_\alpha) + \frac{1}{2}(p_\alpha h_\beta - p_\beta h_\alpha) \tag{S6}$$

where $v_{\alpha\beta} = (\partial_\alpha v_\beta + \partial_\beta v_\alpha)/2$ is the symmetric part of the velocity gradient tensor and h_α is the molecular field defined as the functional derivative of $\mathcal{F}$ with respect to p_α, $h_\alpha = -\delta\mathcal{F}/\delta p_\alpha$. The coefficient $\Delta\mu$ is the chemical potential difference of an out-of-equilibrium reaction, such as the ATP hydrolysis in cells, which renders the system active. From left to right, the terms of $\sigma_{\alpha\beta}$ are:

viscous stresses with a shear viscosity η, anisotropic active stresses proportional to ζ ($\zeta > 0$ for extensile materials), nemato-elastic stresses with transport coefficients ν, and the asymmetric part of the deviatoric stress tensor [57, 58].

We consider that our system is incompressible

$$\partial_\gamma v_\gamma = 0, \tag{S7}$$

consequently the pressure P in Eq. (S5) acts as a Lagrange multiplier to ensure that the density field remains constant. Finally, the dynamics of the polarization field reads

$$\partial_t p_\alpha + v_\beta \partial_\beta p_\alpha + \omega_{\alpha\beta} p_\beta = \frac{h_\alpha}{\gamma} + \lambda p_\beta \partial_\beta p_\alpha - \nu v_{\alpha\beta} p_\beta \tag{S8}$$

where $\omega_{\alpha\beta} = (\partial_\alpha v_\beta - \partial_\beta v_\alpha)/2$ is the antisymmetric part of the velocity gradient tensor, γ is a rotational viscosity, λ is an active transport coefficient and ν is the so-called flow-aligning parameter. The term proportional to λ exists only in polar systems. The sign of the transport coefficient ν is not fixed by thermodynamical principles, and in the context of liquid crystals this coefficient depends, for instance, on the aspect ratio of the constituting particle shape, being $\nu < -1$ for rod-like particles and $\nu > 1$ for disk-like particles. For more details about the derivation of the constitutive equations, we defer the reader to Refs. [57, 58].

SECTION 2: ACTIVE POLAR FLUID EMBEDDED ON A CYLINDRICAL SHELL

In this section, we apply the physical description that was presented in Section 1 to a cylindrical substrate of radius R, Fig. S17. We consider that the physical fields are independent of the azimuthal coordinate θ as well as independent of the longitudinal coordinate z, except for the pressure field P.

The uniform polarization field takes the form $\boldsymbol{p} = p_\theta \hat{\theta} + p_z \hat{z}$, where $\hat{\theta}$ and $\hat{z}$ are unit vectors along the circular cross-section of the cylinder (i.e. azimuthal direction) and along its long axis (i.e. longitudinal direction), respectively. The normal direction to the cylinder surface is the radial direction $\hat{r}$. Hence, p_θ and p_z are the components of the polarization field in each of the in-plane directions. Note that since we are looking for the onset of polarity parallel to the cylindrical surface, naturally $p_r = 0$. Similarly, the uniform velocity field is expressed as $\boldsymbol{v} = v_\theta \hat{\theta} + v_z \hat{z}$.

Under these approximations, the free-energy density f given by Eq. (S1) reduces to

$$f = \left(\frac{\chi_2}{2} + \frac{\overline{\beta}_1}{2R} + \frac{\overline{\beta}_{2,1} + \overline{\beta}_{2,2}}{2R^2} \right) (p_\theta^2 + p_z^2) + \frac{\chi_4}{4} (p_\theta^2 + p_z^2)^2 + \left(\frac{\beta_1}{2R} + \frac{\mathcal{K} + \beta_{2,1} + \beta_{2,2}}{2R^2} \right) p_\theta^2 \tag{S9}$$
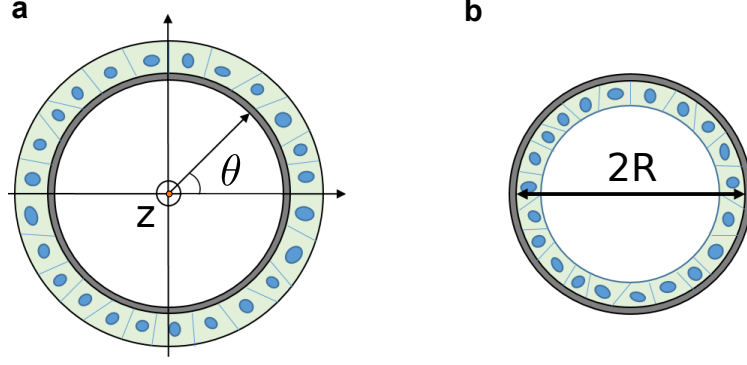
FIG. S17: Schematic drawing of two cell monolayers (light green), laying on either the outer side of a cylindrical substrate (dark gray) in **a** or its inner side in **b**. The radius of the substrate is R. z and θ correspond to the longitudinal coordinate and azimuthal angle, respectively.

where the only non-vanishing component of the curvature tensor is $\mathcal{C}_{\alpha\beta} = (1/R)\hat{\theta} \otimes \hat{\theta}$ and of the polarization gradient tensor is $\partial_\alpha p_\beta = (-p_\theta/R)\hat{\theta} \otimes \hat{r}$. For convenience, we redefine the parameters as follows: $\overline{\beta}_{2,1} + \overline{\beta}_{2,2} \to \overline{\beta}_2$, and $\mathcal{K} + \beta_{2,1} + \beta_{2,2} \to \beta_2$. Note that depending on whether the cell monolayer is inside microtubes or on fibers, the curvature tensor changes from $\mathcal{C}_{\theta\theta} = -1/R$ for microtubes to $\mathcal{C}_{\theta\theta} = 1/R$ for fibers. For convenience, we allow R to change sign to account for the curvature change between microtubes and fibers, and use the convention that $R > 0$ for fibers and $R < 0$ for microtubes. This way, the linear curvature couplings $f_C^{(1)}$ change sign upon changing the face of the substrate that the system sits on, whereas the quadratic curvature couplings $f_C^{(2)}$ do not.

In this case, the components of the molecular field are expressed as

$$h_\theta = -\frac{\delta\mathcal{F}}{\delta p_\theta} = -\left(\chi_2 + \frac{\beta_1 + \overline{\beta}_1}{R} + \frac{\beta_2 + \overline{\beta}_2}{R^2}\right)p_\theta - \chi_4\left(p_\theta^2 + p_z^2\right)p_\theta \tag{S10}$$

$$h_z = -\frac{\delta\mathcal{F}}{\delta p_z} = -\left(\chi_2 + \frac{\overline{\beta}_1}{R} + \frac{\overline{\beta}_2}{R^2}\right)p_z - \chi_4\left(p_\theta^2 + p_z^2\right)p_z \tag{S11}$$

The non-vanishing components of the total stress tensor $\sigma_{\alpha\beta}^t$ given by Eqs. (S5) and (S6) read

$$\sigma_{rr}^t = -P, \tag{S12a}$$

$$\sigma_{r\theta}^t = \sigma_{\theta r}^t = -\eta\frac{v_\theta}{R}, \tag{S12b}$$

$$\sigma_{\theta\theta}^t = -\zeta\Delta\mu p_\theta^2 + \nu p_\theta h_\theta - P - \mathcal{K}\frac{p_\theta^2}{R^2}, \tag{S12c}$$

$$\sigma_{\theta z}^t = -\zeta\Delta\mu p_z p_\theta + \frac{\nu}{2}\left(p_z h_\theta + p_\theta h_z\right) + \frac{1}{2}\left(p_\theta h_z - p_z h_\theta\right), \tag{S12d}$$

$$\sigma_{z\theta}^t = -\zeta\Delta\mu p_z p_\theta + \frac{\nu}{2}\left(p_z h_\theta + p_\theta h_z\right) - \frac{1}{2}\left(p_\theta h_z - p_z h_\theta\right), \tag{S12e}$$

$$\sigma_{zz}^t = -\zeta\Delta\mu p_z^2 + \nu p_z h_z - P, \tag{S12f}$$

where the only non-vanishing component of the velocity gradient tensor is $\partial_\alpha v_\beta = (-v_\theta/R)\hat{\theta} \otimes \hat{r}$. The incompressibility condition (S7) is satisfied by uniform velocity fields (i.e. $v_z = cte$) and reads

$$\partial_z v_z = 0. \tag{S13}$$

The dynamic equations for the polarization field given by Eqs. (S8) reduces to

$$\partial_t p_\theta = h_\theta, \tag{S14a}$$

$$\partial_t p_z = h_z. \tag{S14b}$$

Note that in our case, the term proportional to λ in Eq. (S8) gives a contribution in the radial direction (i.e. $\lambda p_\beta \partial_\beta p_\alpha = (-\lambda p_\theta^2/R)\hat{r}$). Consequently, this term does not influence the dynamics of the in-plane components of the polarization field.

Finally, Eqs. (S4) reduces to force balance in the direction $\hat{\theta}$

$$\partial_r \sigma_{\theta r}^t|_{r=R} + \frac{\sigma_{\theta r}^t + \sigma_{r\theta}^t}{R} = -\eta \frac{v_\theta}{R^2} = \xi v_\theta - T_0 p_\theta, \tag{S15}$$

where the term $\partial_r \sigma_{\theta r}^t|_{r=R} = \eta \frac{v_\theta}{R^2}$ gives a contribution due to the explicit dependence on the cylinder radius R, as well as, force balance in the direction $\hat{z}$

$$-\partial_z P = \xi v_z - T_0 p_z. \tag{S16}$$

Note that in our case, the terms proportional to λ_s and λ_b in Eq. (S4) read $\lambda_s p_\alpha \partial_\beta p_\beta = 0$ and $\lambda_b p_\beta \partial_\beta p_\alpha = (-\lambda_b p_\theta^2/R)\hat{r}$, respectively. The latter can yield forces normal to the cylinder surface, so that these terms do not influence the transition that we discuss here.

SECTION 3: EQUILIBRIUM UNIFORM SOLUTIONS

In the following, we study the equilibrium uniform solutions for the polarization field.

The free-energy density of our system given by Eq. (S9) for a uniform field reads

$$f = \left(\frac{\chi_2}{2} + \frac{\overline{\beta}_1}{2R} + \frac{\overline{\beta}_2}{2R^2}\right)(p_\theta^2 + p_z^2) + \left(\frac{\beta_1}{2R} + \frac{\beta_2}{2R^2}\right)p_\theta^2 + \frac{\chi_4}{4}\left(p_\theta^2 + p_z^2\right)^2. \tag{S17}$$

The equilibrium uniform solutions for the polarization field correspond to the minimum of Eq. (S17), being either an azimuthal ordered phase with both $p_z = 0$ and $p_\theta \neq 0$, or an longitudinal ordered phase with both $p_z \neq 0$ and $p_\theta = 0$, or a disordered phase with $p_z = p_\theta = 0$. Such solutions satisfy $h_\theta = h_z = 0$ in Eqs. (S10). To simplify notation, we denote $\mathcal{A} = \chi_2 + \overline{\beta}_1/R + \overline{\beta}_2/R^2$, and $\mathcal{B} = \beta_1/R + \beta_2/R^2$.

In the following, we study the stability of each of these solutions. Expanding Eq. (S17) within a neighbourhood of each uniform solution, one obtains for an azimuthal ordered phase

$$f \ = \ (\mathscr{A} + \mathscr{B})\frac{(p_\theta^0)^2}{4} - (\mathscr{A} + \mathscr{B})\left(p_\theta - p_\theta^0\right)^2 - \mathscr{B}\frac{p_z^2}{2} + \mathscr{O}_3(p_z, (p_\theta - p_\theta^0)), \tag{S18}$$

where $p_\theta^0 = \pm\sqrt{-(\mathscr{A} + \mathscr{B})/\chi_4}$, and for an longitudinal ordered phase

$$f \ = \ \mathscr{A}\frac{(p_z^0)^2}{4} - \mathscr{A}\left(p_z - p_z^0\right)^2 + \mathscr{B}\frac{p_\theta^2}{2} + \mathscr{O}_3(p_\theta, (p_z - p_z^0)), \tag{S19}$$

where $p_z^0 = \pm\sqrt{-\mathscr{A}/\chi_4}$, and finally for a disordered phase

$$f \ = \ (\mathscr{A} + \mathscr{B})\frac{p_\theta^2}{2} + \mathscr{A}\frac{p_z^2}{2} + \mathscr{O}_3(p_z, p_\theta), \tag{S20}$$

where $\mathscr{O}_3$ denotes third-order corrections.

As shown in Fig. S18, each solution is stable in a different domain of the parameter space. Specifically, an azimuthal ordered phase is stable when both $\mathscr{A} + \mathscr{B} < 0$, and $\mathscr{B} < 0$, according to Eq. (S18). An longitudinal ordered phase is stable when both $\mathscr{A} < 0$, and $\mathscr{B} > 0$, according to Eq. (S19). Finally, a disordered phase is stable when both $\mathscr{A} + \mathscr{B} > 0$, and $\mathscr{A} > 0$, according to Eq. (S20). Note that in the absence of couplings between the polarization and the curvature tensor, $\mathscr{B}, \mathscr{A} > 0$ as $\chi_2 > 0$ and $\mathscr{K} > 0$, hence the disordered phase is linearly stable.
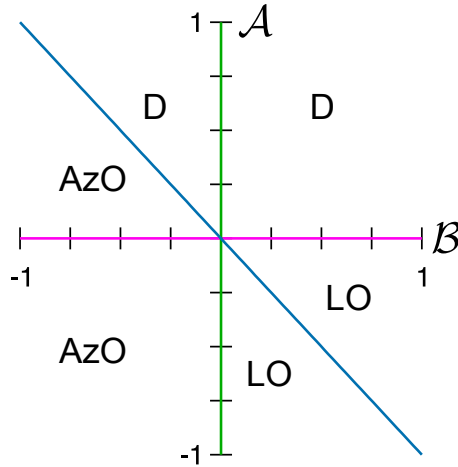

FIG. S18: Phase diagram of equilibrium uniform phases as a function of the parameters $\mathscr{A} = \chi_2 + \overline{\beta}_1/R + \overline{\beta}_2/R^2$ and $\mathscr{B} = \beta_1/R + \beta_2/R^2$. The solid lines delimit the boundaries between each stability region of equilibrium phases: blue $\mathscr{A} + \mathscr{B} = 0$, pink $\mathscr{A} = 0$, and green $\mathscr{B} = 0$. The equilibrium phases are labelled as: AzO for an azimuthal ordered phase, LO for an longitudinal ordered phase and D for a disordered phase.

The stability of equilibrium uniform solutions depend on the geometry of the substrate R, as well as the side of the substrate that the system sits on. To understand how the substrate

geometry can influence the solution's stability, we restrict the following discussion to a parameter space wherein $\mathcal{A} > 0$ for any value of R. This parameter regime guarantees that only a transition between an azimuthal ordered phases and a disordered phase could occur, and it can be achieved by, for instance, assuming that $\overline{\beta}_1 = \overline{\beta}_2 = 0$ as $\chi_2 > 0$, which we assume hereon. Under this simplification, the transition occurs whenever $\mathcal{A} + \mathcal{B} = 0$, resulting in two different critical radii

$$R_c^1 \chi_2 / \beta_1 = (-1 + \sqrt{1 - 4\beta_2 \chi_2 / \beta_1^2})/2, \tag{S21}$$

$$R_c^2 \chi_2 / \beta_1 = (-1 - \sqrt{1 - 4\beta_2 \chi_2 / \beta_1^2})/2. \tag{S22}$$

For convenience, we define the rescaled radius $r = R\chi_2/\beta_1$, and the rescaled critical radius $r_c^1 = R_c^1 \chi_2$ and $r_c^2 = R_c^2 \chi_2$.

If $\beta_2 < 0$, there exists two real critical radius r_c^1 and r_c^2, Fig. 5 in the main text, whereat $\mathcal{A} + \mathcal{B} = 0$ in Fig. S18. For a radius $r > r_c^1$ or $r < r_c^2$, the disordered phase with $p_z = p_\theta = 0$ is favoured. For $r_c^2 < r < r_c^1$, substrate curvature aligns the polarization in the azimuthal direction that is $p_z = 0$ and $p_\theta = \pm\mathscr{P}$, that reads

$$\mathscr{P} = \sqrt{-\left(\chi_2 + \frac{\beta_1}{R} + \frac{\beta_2}{R^2}\right)/\chi_4}. \tag{S23}$$

If $\beta_2 > 0$, one can have two different scenarios, Fig. 5 in the main text. The first scenario is obtained when both $r < 0$, and $\beta_1^2 > 4\beta_2 \chi_2$. In this case, there exist two positive critical radii, r_c^1 and r_c^2, for which a transition between a disordered and an azimuthal ordered phase occurs. For $r > r_c^1$ or $r < r_c^2$, the disordered phase with $p_z = p_\theta = 0$ is dominant. For $r_c^2 < r < r_c^1$, a phase with an azimuthal alignment $p_z = 0$ and $p_\theta = \pm\mathscr{P}$ is dominant, where $\mathscr{P}$ is given by Eq. (S23). In the second scenario, when $r < 0$, and $\beta_1^2 < 4\beta_2 \chi_2$ or $r > 0$, the dominant phase is disordered.

To gain further insights into the influence of the linear curvature-polarization couplings in the free-energy density (S1) on the solution's stability, let us consider the limiting case whereby $f_C^{(1)}$ given by Eq. (S2) vanishes. Following the same reasoning as above, if $\beta_2 < 0$, both critical radius have the same absolute value $|R_c^1| = |R_c^2|$. This means that the transition between a disordered and an azimuthal ordered phase occurs for the same radius $|R|$ on both sides of the substrate. If $\beta_2 > 0$, no real critical radii exists and the system forms a disordered phase regardless of the substrate radius R. Therefore, linear curvature-polarization couplings (S2) are crucial to establish an asymmetry between the critical radii for the transition on both sides of the substrate.

Similarly, to gain further insights into the influence of the quadratic curvature-polarization couplings in the free-energy density (S1) on the solution's stability, let us consider the limiting case whereby $f_C^{(2)}$ given by Eq. (S2) vanishes. As $\beta_2 = \mathcal{K} > 0$ can only be positive, the disordered

phase is dominant regardless of R on, at least, one of the two sides of the substrate. Therefore, quadratic curvature-polarization couplings (S3) are crucial to sustain an azimuthal ordered phase over a range of radii R on both sides of the substrate.

In conclusion, depending on the sign of β_2, we predict two distinct scenarios: first, an active polar fluid that on one side of the substrate, could either form an azimuthal ordered phase at intermediate substrate radii R or a disordered phase regardless of the values of R, while on the other side of the substrate it forms a disordered phase regardless of R. Second, an active polar fluid forming an azimuthal ordered phase for R smaller than a critical radius that depends on the side of the substrate on which the system sits.

SECTION 4: STEADY-STATE DYNAMICS OF UNIFORM SOLUTIONS

In the following, we study the stress and velocity patterns of the uniform solutions for the polarization field from Section 3.

The equilibrium uniform solutions for the polarization field can be stable to fluctuations in the absence of activity or specific boundaries, see Section 3. In the geometry we consider, our active polar fluid includes, however, two active contributions controlled by the parameters: $\zeta\Delta\mu$ corresponding to the amplitude of the anisotropic active stresses, and T_0 corresponding to the amplitude of the traction forces. It is expected that for sufficiently large values of $\zeta\Delta\mu$, the uniform ordered solutions of the polarization field become unstable to linear fluctuations, as reported in other contexts by many authors [85]. A detailed analysis of the influence of $\zeta\Delta\mu$ on the stability of our uniform solutions falls beyond the scope of this manuscript. However, it is important to note that due to the substrate geometry and the coupling terms $f_C^{(1)}$ and $f_C^{(2)}$ given by Eqs. (S2)-(S3), the rotational symmetry of the system is broken. In this case, global rotations of the polarization field are linearly stable for small enough activity. Here, we assume that the uniform solutions for the polarization field that were found in the previous section are stable over the range of radii R under study.

The longitudinal component of the velocity field v_z is obtained by solving Eq. (S13) and reads

$$v_z = V, \tag{S24}$$

where V is an integration constant that is set by boundary conditions. For a uniform azimuthal ordered phase, according to Eq. (S16), we predict that the pressure field P is a linear function of

the longitudinal coordinate

$$P - P_0 = -\xi V z, \tag{S25}$$

where P_0 is an integration constant. Note that a non-vanishing v_z requires different boundary conditions on each end of the cylindrical surface, such as in the presence of a leading edge. Otherwise, $v_z = 0$ and $P = P_0$, and only azimuthal motion could be observed.

In this case, from Eq. (S15), one obtains for the azimuthal component of the velocity field

$$v_\theta = \frac{T_0}{\xi + \eta/R^2}\mathscr{P}, \tag{S26}$$

where $\mathscr{P}$ is given by Eq. (S23).

For a uniform disordered phase, the velocity field v_θ vanishes, see Eq. (S15).

As shown in Fig. 5 in the main text, the azimuthal velocity v_θ exhibits a non-monotonic dependence on the substrate radius R. Normalising the velocity amplitude by the factor $T_0\sqrt{\chi_2/\chi_4}/\xi$ and the substrate radii by $x = -R\chi_2/\beta_1$, one obtains that the azimuthal velocity given by Eq. (S26) depends on two dimensionless parameters: $\alpha_1 = -\beta_2\chi_2/\beta_1^2$, and $\alpha_2 = \eta\chi_2^2/\xi\beta_1^2$. The dimensionelss azimuthal velocity takes the form

$$v_\theta = \pm\frac{1}{1 + \alpha_2/x^2}\sqrt{\frac{\alpha_1}{x^2} + \frac{1}{x} - 1}. \tag{S27}$$

The existence of this velocity is linked to the region of stability of the azimuthal ordered phase, which is discussed in the above section.

Thus we find that for an infinite cylindrical surface, we expect pure azimuthal rotation, whereas in the presence of boundaries, such as a leading edge, we expect helical migration. The latter results from the combination of the longitudinal velocity induced by the leading edge, and the azimuthal velocity resulting from curvature-induced symmetry breaking.

SECTION 5: FITTING PROCEDURE ON THE VELOCITY PATTERNS

In the following, we detail the procedure for computing the fitting parameters from the experimental curves of the azimuthal component of the velocity field as a function of the substrate radius R for MDCK cell monolayers.

As MDCK cells, in both microtubes and fibers, exhibit collective rotation along the azimuthal direction for radii smaller than a critical value, we consider that $\beta_2 < 0$ (see Section 3). As shown in Section 4, the theoretical curve for the azimuthal velocity reads

$$v_\theta = \frac{T_0\sqrt{\chi_2/\chi_4}}{\xi + \eta/R^2}\sqrt{-\left(1 + \frac{\beta_1}{\chi_2 R} - \frac{|\beta_2|}{\chi_2 R^2}\right)}, \tag{S28}$$
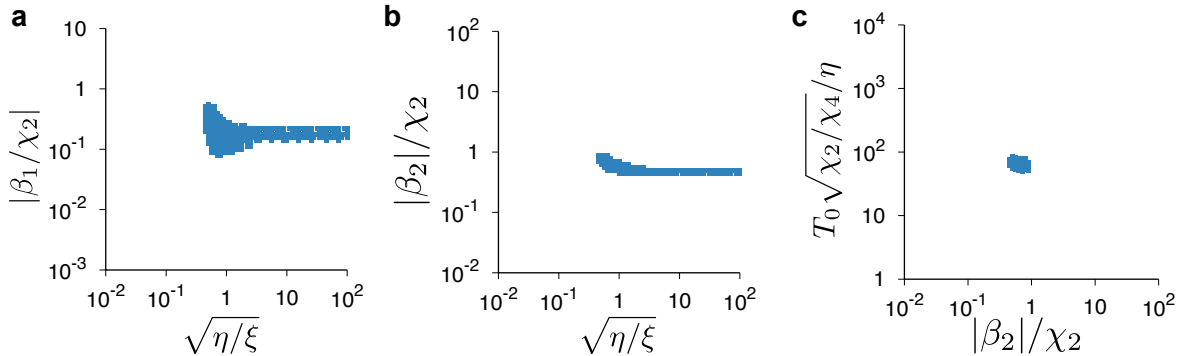
FIG. S19: Region of the parameter space whereby the error function $\mathcal{E}$ given by Eq. (S29) is at most 10% larger than the absolute minimum error $\mathcal{E}_{min}$. panel **a** shows a cross-section of the parameter space on the plane $|\beta_1/\chi_2|$-$\sqrt{\eta/\xi}$, panel **b** on $|\beta_2|/\chi_2$-$\sqrt{\eta/\xi}$, and panel **c** on $T_0\sqrt{\chi_2/\chi_4}/\eta$-$|\beta_2|/\chi_2$. The parameters $\overline{\beta}_1 = \overline{\beta}_2 = 0$ and the unit of length was set to 100 μm, and the unit of velocity to 1 μm/h.

where we can identify four distinct parameters: a velocity scale $V = T_0\sqrt{\chi_2/\chi_4}/\xi$, a friction length $L_\eta = \sqrt{\eta/\xi}$, and two coupling parameters between the polarization field and the substrate curvature $c_1 = \beta_1/\chi_2$, and $c_2 = |\beta_2|/\chi_2$. Remember that according to our convention, we allow R to change sign to account for the curvature change between microtubes and fibers, and use the convention that $R > 0$ for fibers and $R < 0$ for microtubes.

For a given set of the fitting parameters (V, L_η, c_1, c_2), we compute the error function

$$\mathcal{E} = \sqrt{\sum_{\#exp} |v_\theta^{exp}(R) - v_\theta|^2}, \tag{S29}$$

where v_θ is given by Eq. (S28), and $v_\theta^{exp}(R)$ corresponds to the experimental value of the azimuthal velocity for a given radii R in either microtubes or fibers. The sum in Eq. (S29) runs over all experimental values, namely MDCK monolayers on microtubes and fibers in a range of substrate diameters $2|R|$ from 25 μm to 250 μm (see Methods). For substrate diameter $2|R| > 150$ μm in microtubes and $2|R| > 100$ μm in fibers, collective rotation is not found to be the dominant phase, and we consider that the $v_\theta^{exp}(R) = 0$ for these values of R.

We compute the error function $\mathcal{E}$ in the parameter space $(V, L_\eta, c_1, c_2) = (10^{-1}, 10^8) \times (10^{-2}, 10^2) \times (10^{-3}, 10) \times (10^{-2}, 10^2)$, where the units of length were set to 100 μm, and the units of velocity to 1 μm/h. We search for the absolute minimum $\mathcal{E}_{min}$ of the error function over the parameter space (V, L_η, c_1, c_2). Fig. S19 shows the subset of the previous parameter space whereby the error function $\mathcal{E} < 1.1 * \mathcal{E}_{min}$. Our analysis disclosed a single region of the parameter space that is compatible with the experimental measurements. Fig. 5 in the main text shows the comparison in both microtubes and fibers between the experimental profiles of the azimuthal velocity $v_\theta^{exp}(R)$

Parameter	Definition	Mean±SD
$V/L_\eta^2 = T_0\sqrt{\chi_2/\chi_4}/\eta$	Ratio between velocity scale and friction length squared	0.0064 ± 0.0007 $1/(\mu\text{m h})$
$L_\eta = \sqrt{\eta/\xi}$	Friction Length	> 40 μm
$|\beta_1/\chi_2|$	Linear coupling between the polarization field and the substrate curvature	21 ± 8 μm
β_2/χ_2	Quadratic coupling between the polarization field and the substrate curvature	-6000 ± 1000 μm^2

TABLE S1: Estimation of material parameters for an active polar fluid. $\beta_1/\chi_2 R$ is positive for fibers. The error bars correspond to the SD in the region of the parameter space that satisfies $\mathcal{E} < 1.1 * \mathcal{E}_{min}$.

as a function of the radii R, and the theoretical fits of v_θ for the optimal parameter region.

Table S1 contains the average and standard deviation of the fitting parameters in the region of parameters from Fig. S19. We find that the lower bound of the friction length L_η is compatible to that found in MDCK monolayers spreading on flat surfaces [56]. Both coupling parameters (β_1, β_2) between the polarization field and the substrate curvature are finite. $\beta_2/\chi_2 < 0$ showing that the effect of substrate curvature are dominant compared to the elastic deformations of the polarization field associated with the Frank constant $\mathcal{K}$. We found that the ratio $|\beta_2/\beta_1| > 200$ μm is larger than the typical threshold of collective rotation in microtubes and fibers, $2|R| > 150$ μm and $2|R| > 100$ μm respectively, showing that quadratic couplings are predominant for collective rotation in cylindrical MDCK monolayers.

SECTION 6: GENERALISATION WITH TWO ORIENTATIONAL ORDERED FIELDS

In experiments, the orientation of actin fibrils was found on average in the longitudinal direction for microtubes, and in the azimuthal direction for fibers, see Fig. 4 in the main text. Such organisation contrasts with the average direction of collective rotation, which is in the azimuthal direction for both microtubes and fibers, see Fig. 2 and 3 in the main text. In the following, we discuss steady-state patterns made of two coupled orientational ordered fields in a liquid crystal on a cylindrical surface and show that one can understand these experimental observations.

Actin fibrils exhibit a clear nematic order, which contrasts with the polar order corresponding to the azimuthal motion of cell monolayers. Hence, we consider a liquid crystal with two coupled orientational ordered fields: a polarization field $\mathbf{p}$ corresponding to the spontaneous motion and a director field $\mathbf{n}$ corresponding to the actin fibrils. This means that the physical description

is invariant to $\mathbf{n} \to -\mathbf{n}$ but is not invariant to $\mathbf{p} \to -\mathbf{p}$. A convenient way for discussing the orientation patterns for an azimuthally moving system consists in writing an effective free-energy density:

$$\mathcal{F} = \int_{\mathcal{A}} f \, da = \int_{\mathcal{A}} \Big(\frac{\chi_2}{2} p_\gamma p_\gamma + \frac{\chi_4}{4} (p_\gamma p_\gamma)^2 + \frac{\mathcal{K}}{2} (\partial_\beta p_\gamma)(\partial_\beta p_\gamma) + f_C^{(1)}(\mathcal{C}_{\alpha\beta}, p_\alpha) + f_C^{(2)}(\mathcal{C}_{\alpha\beta}, p_\alpha)$$
$$\frac{\bar{\chi}_2}{2} n_\gamma n_\gamma + \frac{\bar{\mathcal{K}}}{2} (\partial_\beta n_\gamma)(\partial_\beta n_\gamma) + h_C^{(1)}(\mathcal{C}_{\alpha\beta}, n_\alpha) + h_C^{(2)}(\mathcal{C}_{\alpha\beta}, n_\alpha) + g_{pn}^{(0)}(p_\beta, n_\alpha)$$
$$+ g_{pn}^{(1)}(\mathcal{C}_{\alpha\beta}, p_\beta, n_\alpha) + g_{pn}^{(2)}(\mathcal{C}_{\alpha\beta}, p_\beta, n_\alpha) \Big) da, \tag{S30}$$

where we assumed a one-constant approximation for both fields [83]. In view of the fact that in experiments, the orientational order of actin fibrils is well developed, we consider that $|\mathbf{n}| = 1$. In this case, the parameter $\bar{\chi}_2$ acts as a Lagrange multiplier. Additionally, we consider that both orientational fields $\mathbf{p}$ and $\mathbf{n}$ are uniform. In the previous free-energy density, the term $\bar{\mathcal{K}}/2(\partial_\beta n_\gamma)(\partial_\beta n_\gamma)$ is computed in a similar way to the term $\mathcal{K}/2(\partial_\beta p_\gamma)(\partial_\beta p_\gamma)$ as it was explained in Section 1.

The first two coupling functions $f_C^{(1)}$ and $f_C^{(2)}$ are given by Eqs. (S2)-(S3). The other coupling functions read

$$h_C^{(1)} = \frac{\beta_3}{2} \mathcal{C}_{\alpha\beta} n_\beta n_\alpha, \tag{S31}$$

$$h_C^{(2)} = \frac{\beta_{4,1}}{2} \mathcal{C}_{\alpha\gamma} \mathcal{C}_{\alpha\beta} n_\beta n_\gamma + \frac{\beta_{4,2}}{2} \mathcal{C}_{\gamma\gamma} \mathcal{C}_{\alpha\beta} n_\beta n_\alpha \tag{S32}$$

$$g_{pn}^{(0)} = \frac{\lambda_{0,1}}{2} p_\alpha p_\beta n_\beta n_\alpha, \tag{S33}$$

$$g_{pn}^{(1)} = \frac{\lambda_{1,2}}{2} \mathcal{C}_{\alpha\beta} p_\alpha p_\gamma n_\gamma n_\beta + \frac{\lambda_{1,3}}{2} \mathcal{C}_{\alpha\beta} p_\gamma p_\gamma n_\alpha n_\beta + \frac{\lambda_{1,4}}{2} \mathcal{C}_{\gamma\gamma} p_\alpha p_\beta n_\alpha n_\beta \tag{S34}$$

$$g_{pn}^{(2)} = \frac{\lambda_{2,1}}{2} \mathcal{C}_{\alpha\beta} \mathcal{C}_{\alpha\beta} p_\delta p_\gamma n_\delta n_\gamma + \frac{\lambda_{2,4}}{2} \mathcal{C}_{\alpha\beta} \mathcal{C}_{\alpha\delta} p_\beta p_\gamma n_\delta n_\gamma + \frac{\lambda_{2,5}}{2} \mathcal{C}_{\alpha\beta} \mathcal{C}_{\alpha\delta} p_\gamma p_\gamma n_\beta n_\delta$$
$$+ \frac{\lambda_{2,7}}{2} \mathcal{C}_{\alpha\beta} \mathcal{C}_{\delta\delta} p_\alpha p_\gamma n_\gamma n_\beta + \frac{\lambda_{2,8}}{2} \mathcal{C}_{\alpha\beta} \mathcal{C}_{\delta\delta} p_\gamma p_\gamma n_\alpha n_\beta + \frac{\lambda_{2,9}}{2} \mathcal{C}_{\gamma\gamma} \mathcal{C}_{\delta\delta} p_\alpha p_\beta n_\alpha n_\beta. \tag{S35}$$

We restrict ourselves to couplings that are compatible with the symmetries of the system and at most of second order in either $\mathbf{p}$, $\mathbf{n}$, or the extrinsic curvature tensor $\mathcal{C}$.

To simplify the discussion, we consider directly the experimental case, where $\mathbf{p} = \bar{\mathcal{P}} \hat{\theta}$ as discussed in Section 3. Then, the effective free energy density f given by Eq. (S30) reduces to

$$f = \frac{\chi_2}{2} \bar{\mathcal{P}}^2 + \frac{\chi_4}{4} \bar{\mathcal{P}}^4 + \frac{\bar{\chi}_2}{2} |\mathbf{n}|^2 + \frac{\beta_1 + \overline{\beta}_1}{2R} \bar{\mathcal{P}}^2 + \frac{\mathcal{K} + \beta_{2,1} + \overline{\beta}_{2,1} + \beta_{2,2} + \overline{\beta}_{2,2}}{2R^2} \bar{\mathcal{P}}^2 + \frac{\beta_3}{2R} n_\theta^2$$
$$+ \frac{\bar{\mathcal{K}} + \beta_{4,1} + \beta_{4,2}}{2R^2} n_\theta^2 + \frac{\lambda_{0,1}}{2} \bar{\mathcal{P}}^2 n_\theta^2 + \frac{\lambda_{1,2} + \lambda_{1,3} + \lambda_{1,4}}{2R} \bar{\mathcal{P}}^2 n_\theta^2$$
$$+ \frac{\lambda_{2,1} + \lambda_{2,4} + \lambda_{2,5} + \lambda_{2,7} + \lambda_{2,8} + \lambda_{2,9}}{2R^2} \bar{\mathcal{P}}^2 n_\theta^2, \tag{S36}$$

which can be recast as

$$f = \frac{\mathcal{A}}{2} \bar{\mathcal{P}}^2 + \frac{\mathcal{B}}{4} \bar{\mathcal{P}}^4 + \frac{\mathcal{C} + \mathcal{D} \bar{\mathcal{P}}^2}{2} n_\theta^2 + cte, \tag{S37}$$

where the effective parameters $\mathscr{A}$, $\mathscr{B}$, $\mathscr{C}$, and $\mathscr{D}$ depend on the material parameters of Eqs. (S36) and the substrate radius R. The third term is the only one that influences the orientation field $\mathbf{n}$. The steady-state solution for $\mathbf{n}$ can be obtained by minimising the effective free-energy density (S37).

Recall, that according to our convention, we allow R to change sign to account for the curvature change between microtubes and fibers, and use the convention that $R > 0$ for fibers and $R < 0$ for microtubes. This effect can change both the amplitude of the polarization field $\mathbf{p}$ given by $\bar{\mathscr{P}}$ and the linear couplings with the extrinsic curvature tensor $C_{\alpha\beta}$ in a microtube and in a fiber. To denote the values of the effective parameters on microtubes and fibers, we use from now on, the superscript, t and f, respectively.

As actin-fibril networks orient in the longitudinal direction for microtubes, Fig. 4 in the main text, this implies that $0 < \mathcal{C}^t + \mathscr{D}^t(\bar{\mathscr{P}}^t)^2$. Whereas as actin-fibril networks orient in the azimuthal direction for fibers, Fig. 4 in the main text, this implies that $0 > \mathcal{C}^f + \mathscr{D}^f(\bar{\mathscr{P}}^f)^2$. Rearranging these conditions leads us to

$$0 < \mathcal{C}^t - \mathcal{C}^f + \mathscr{D}^t(\bar{\mathscr{P}}^t)^2 - \mathscr{D}^f(\bar{\mathscr{P}}^f)^2. \tag{S38}$$

The inequality (S38) can only be satisfied in the regime where the dominant coupling terms are those linearly proportional to the extrinsic curvature tensor $C_{\alpha\beta}$ in Eq. (S37). Indeed, let us neglect such terms in Eq. (S37). In this case, the effective parameters are independent on the side of the substrate that the system sits on, meaning that $\mathcal{C}^t = \mathcal{C}^f$ and $\mathscr{D}^t(\bar{\mathscr{P}}^t)^2 = \mathscr{D}^f(\bar{\mathscr{P}}^f)^2$, and the inequality (S38) is unfulfilled. Therefore, the experimental actin-fibril organisation for microtubes and fibers shows that the steady-state orientation patterns of such actin organisations are dominated by couplings that are linearly proportional to the extrinsic curvature tensor.

Note that the theoretical analysis suggests that such linear couplings could arise from two different microscopical mechanisms. For instance, they could result from direct interactions between the curvature and actin fibrils through the effective couplings included in $\mathcal{C}$; or they could result from indirect interactions between the curvature and actin fibrils mediated by cell polarization markers like cryptic lamellipodia through the effective couplings included in $\mathscr{D}$.

Figures S1 to S16
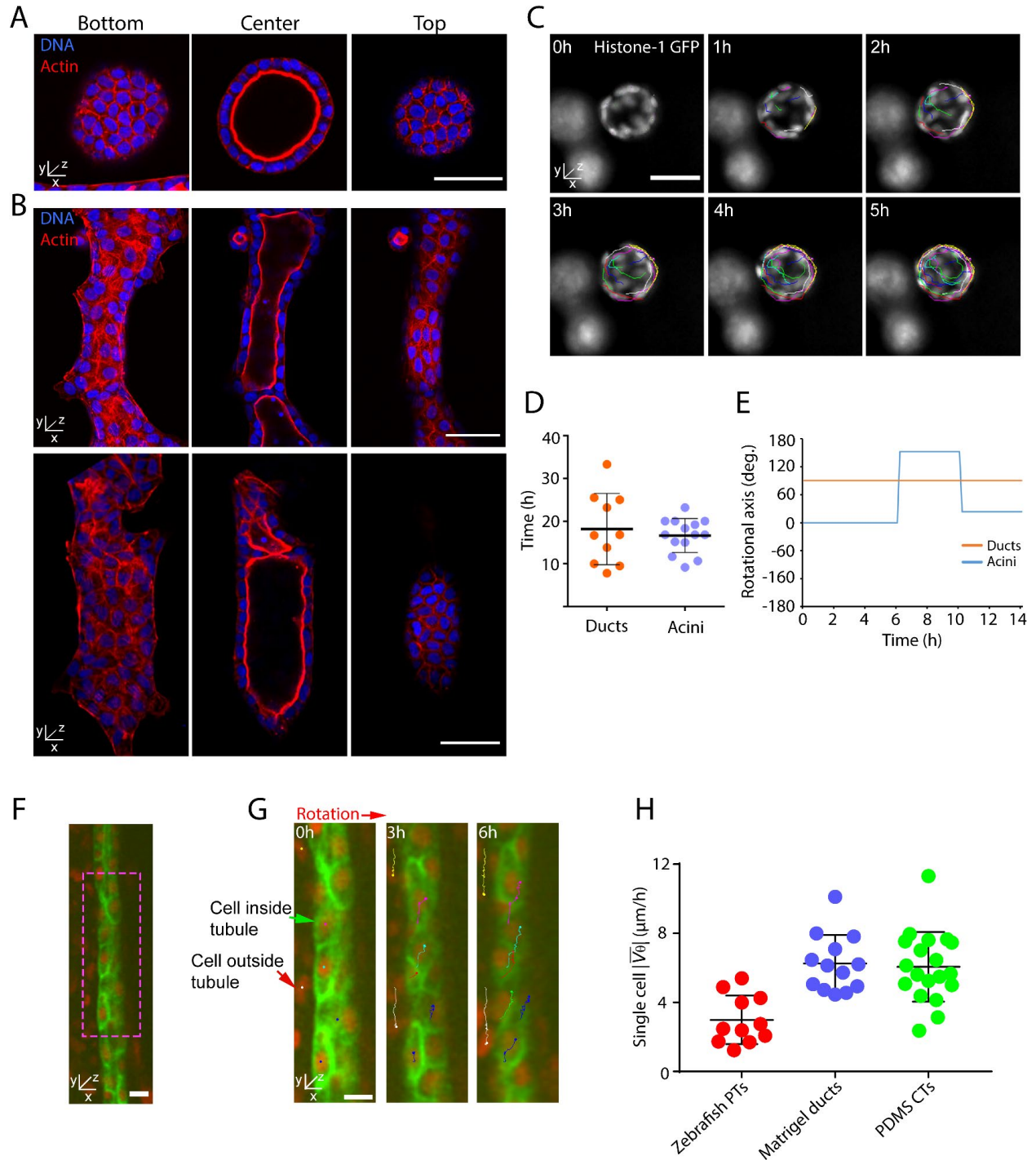
Fig. S1.

(**A**) and (**B**) Images at different z-positions of a histone 1-GFP (H1-GFP) MDCK spherical cyst (**A**) and two tubular MDCK ducts (**B**) of different diameters (Øs) grown inside Matrigel, stained for actin filaments (red). H1-GFP nuclei are colored in blue. From left to right, the bottom, middle and top views of the 3D tissues are shown. Scale bars, 50 μm. (**C**) Time-lapsed images of a rotating spherical H1-GFP MDCK acinus. Single cell trajectories are portrayed with varying color lines for

each cell. Scale bar, 50 µm. (**D**) Graph showing the duration of collective epithelial rotation (CeR) in MDCK ducts ($n = 10$) and acini ($n = 14$), from 3 independent experiments. (**E**) Graph showing angular variation of rotational axes over time relative to x-axis in a representative MDCK duct (orange line) and acinus (blue line). (**F**) Snapshot image of a time-lapse movie showing the distal pronephric tubule of a transgenic Tg(cldnb:lynEGFP) embryo. Cells of the pronephric tubule express a membrane-bound GFP and H2B-mcherry in nuclei. Zoom-in region highlighted by magenta dash box is shown in (**G**). Scale bar, 20µm. (**G**) Cropped region (magenta dash box in (**F**)) from (**F**) highlighting part of the tubule in which cells rotate in azimuthal direction (indicated by red arrow) during tubule elongation at approximately 35 hours post-fertilization (hpf). Single cell trajectories are portrayed with varying color lines. Cells outside the tubule are indicated by white and yellow lines while cells inside the tubule are indicated by other colors. Cells outside have longitudinal-aligned trajectories. In contrast, the trajectories for cells of the tubule show features of a helical movement, resulting from the superposition of azimuthal rotation and longitudinal displacement. Scale bar, 10 µm. (**H**) Absolute values of average single cell azimuthal velocities (V_θ) in rotating zebrafish pronephric tubules (red, $n = 11$), MDCK ducts in Matrigel (blue, $n = 13$) and MDCK tubular cylindrical tissues (t-CTs) inside PDMS microtubes (green, $n = 19$) of similar size (Ø = 20 – 25 µm). Data are presented as individual values with mean ± s.d.
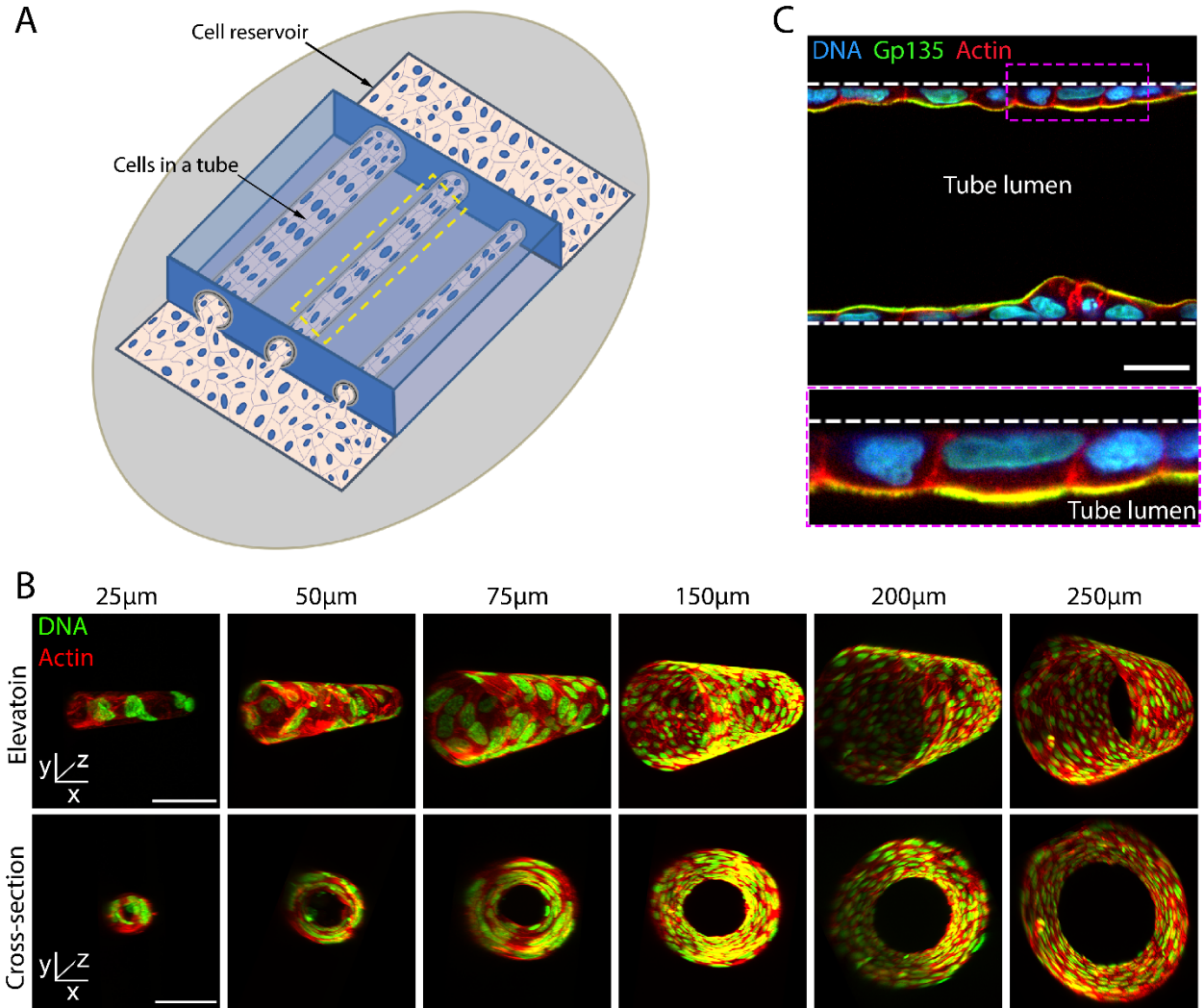
Fig. S2.

(**A**) Schematic representation of the experimental set up to form *in vitro* MDCK *t*-CTs. Cells were loaded in the reservoir areas and let grow inside various PDMS tubes until confluence to form *t*-CTs of varying diameters. Yellow dash box indicates a typical observation region for CeR. (**B**) 3D fluorescent representations of MDCK *t*-CTs of different diameters. Nuclei in green (H1-GFP) and actin in red. Scale bars, 50 µm. (**C**) Representative fluorescent image of a confluent MDCK *t*-CTs with Ø = 75 µm, stained for apical marker – Gp135 (green), actin (red) and DAPI (blue). The white dashed lines mark inner borders of PDMS tube. Zoom-in image highlighted by the magenta dashed-box is shown at the lower part of the image. Scale bar, 20µm.

18
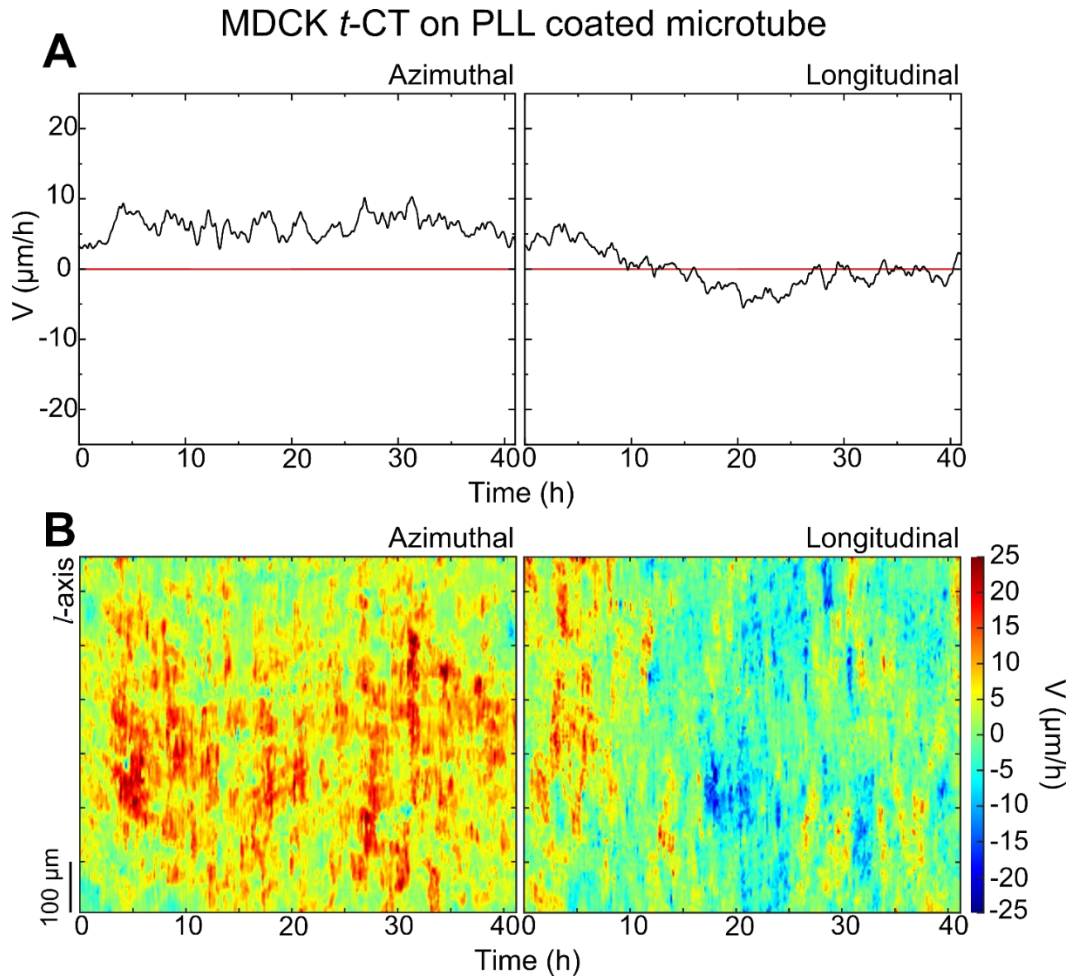
Fig. S3.

Representative graphs (**A**) and kymographs (**B**) showing average velocities (V) of a MDCK H1-GFP t-CT in azimuthal and longitudinal directions as a function of time. The t-CT grows in a PLL-coated PDMS microtube of $\varnothing = 75$ µm. V is calculated using particle imaging velocimetry (PIV) analysis. The graphs then plot the average azimuthal and longitudinal component of V for each time point (**A**), reflecting the average movement of the whole t-CT. The kymographs (**B**) demonstrate spatial average azimuthal, $\vec{V_\theta}$ and longitudinal, $\vec{V_z}$ velocities along the l-axis for every time point for entire observation period, thus showing spatiotemporal distribution of local velocities.
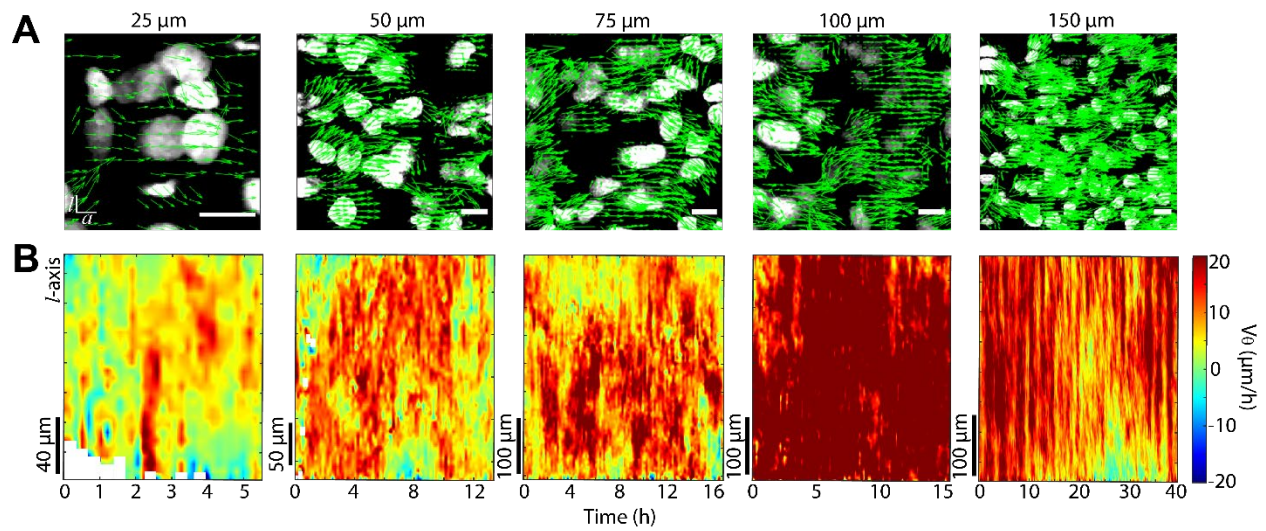
Fig. S4.

(**A**) Representative cropped snapshots of particle imaging velocimetry (PIV) analysis performed on 2D projections of H1-GFP MDCK *t*-CTs of various diameters. Green arrows show local velocity direction. Scale bars, 20µm. (**B**) Representative examples of kymographs showing PIV-calculated spatial average $\overrightarrow{V_\theta}$ along *l*-axis as a function of time for different *t*-CTs. The color code indicates overall average $\overrightarrow{V_\theta}$ peaks at Ø =100 µm.
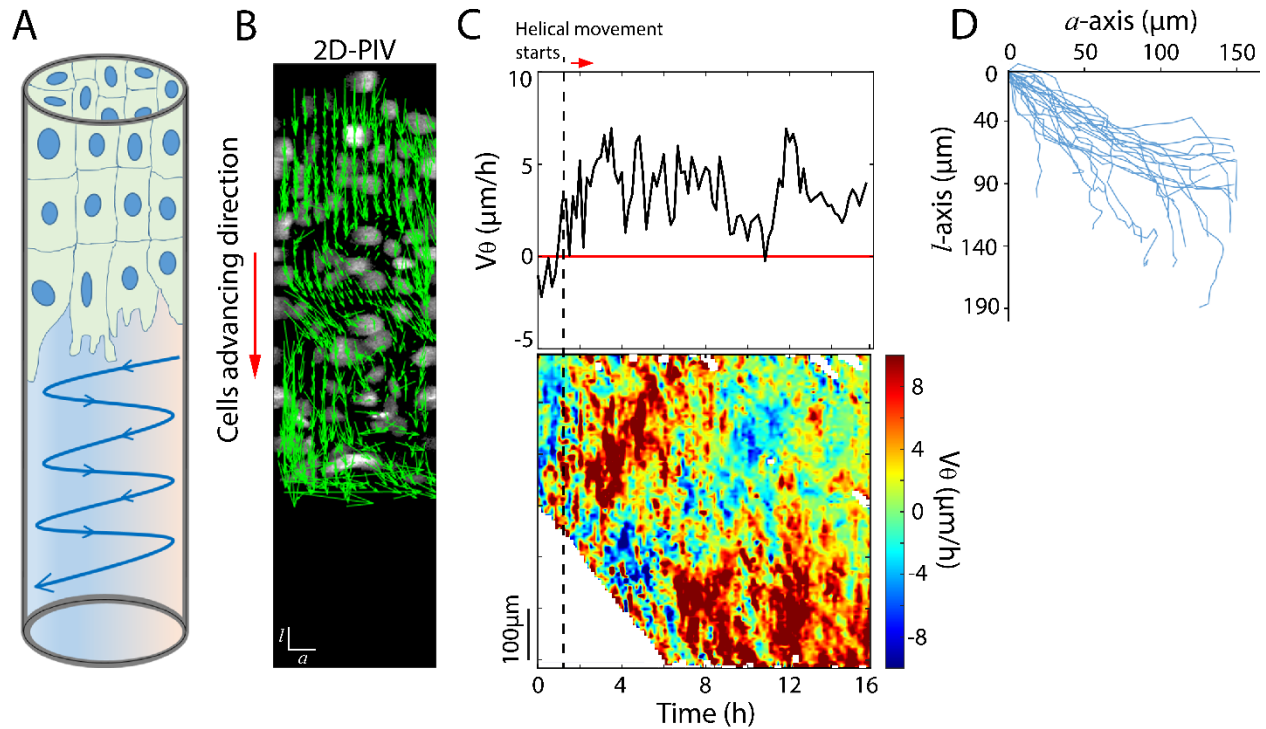
Fig. S5.
(**A**) Schematic representation of collective helical migration inside a non-confluent PDMS microtube with an advancing MDCK *t*-CT. (**B**) Representative snapshot of PIV analysis on a 2D projection of a H1-GFP MDCK *t*-CT of Ø = 50 μm showing features of helical movement. Green arrows map the velocity field. (**C**) Graph (top) and kymograph (bottom) showing spatiotemporal average azimuthal velocity (V_θ) of the advancing *t*-CT in (**B**) evolving with time. Black dash line indicates the start time point of the collective helical movement. (**D**) Representative single cell trajectories in the advancing *t*-CT in (**B**) showing cell displacement in both *a*- and *l*-axes, a feature of collective helical migration. Cell trajectories were determined by tracking displacement of H1-GFP nuclei.
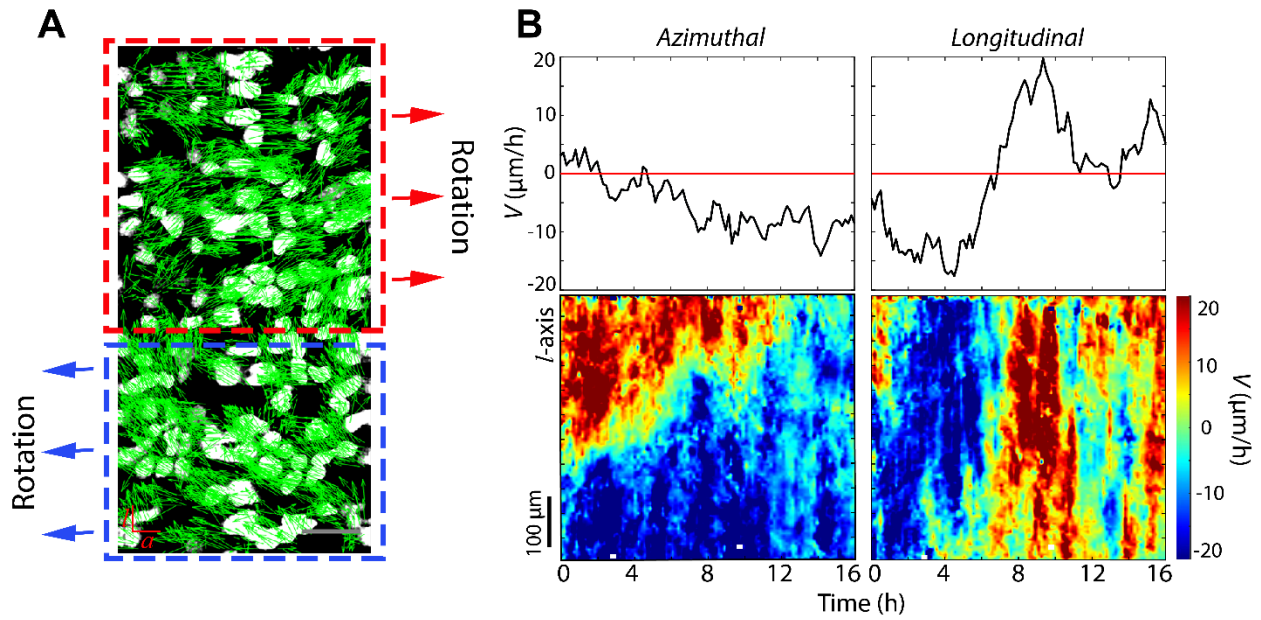
Fig. S6.
(**A**) Representative cropped snapshot of PIV analysis on a 2D projection of a Ø = 75µm H1-GFP MDCK *t*-CT where two neighboring cell groups engage in opposite azimuthal movements. Red dash box indicates the cell group rotating towards the right and blue dash box indicates the cell group rotating towards the left. Scale bar, 50µm. (**B**) Graphs (top panel) and kymographs (bottom panel) showing spatiotemporal average azimuthal and longitudinal velocities of the *t*-CT in (**A**). The azimuthal velocity kymograph shows that as time passes, the cohort rotating towards the left prevails and the whole *t*-CT rotates uniformly in one direction.
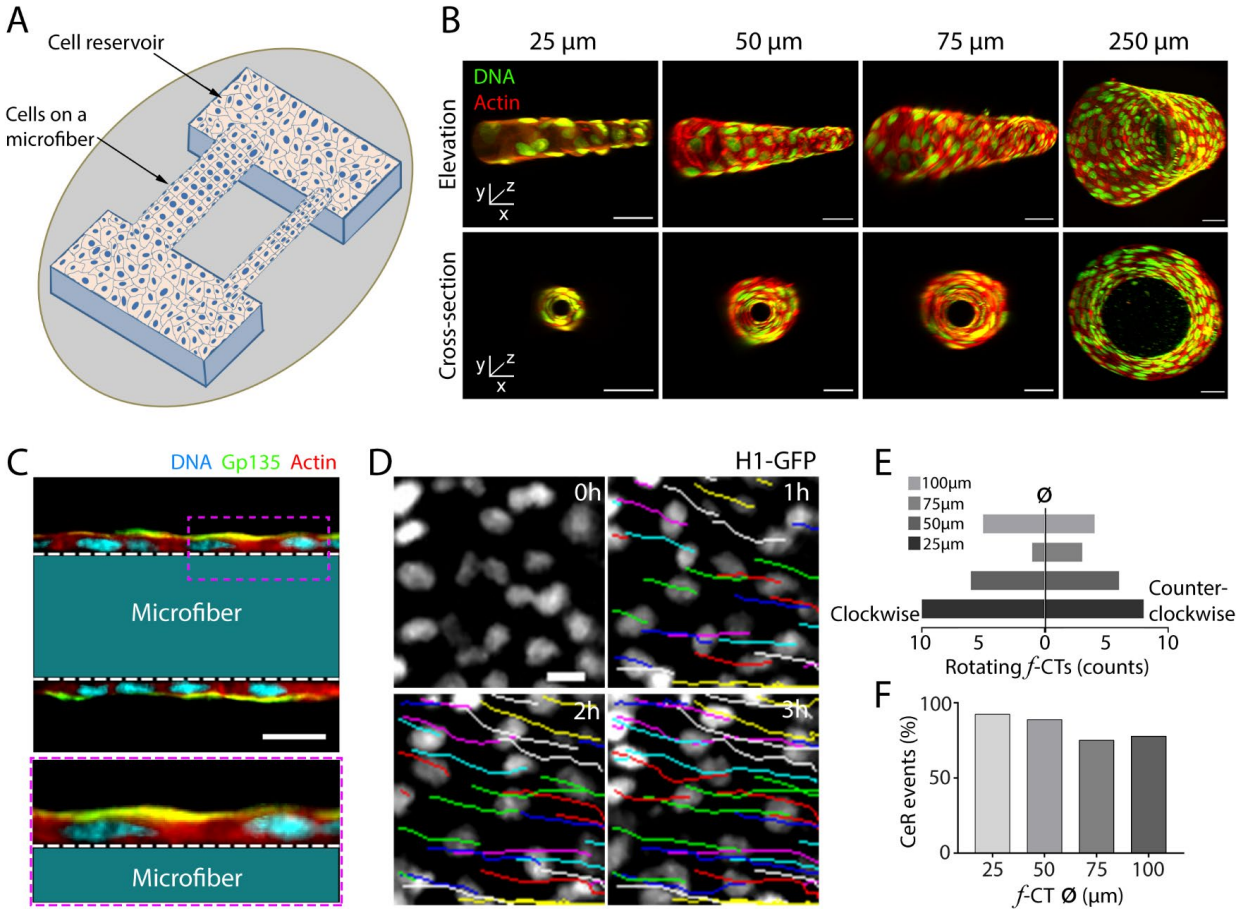
Fig. S7.

(**A**) Schematic representation of the experimental set up to form *in vitro* MDCK CTs on PDMS microfibers (*f*-CTs). Cells were loaded in the reservoir areas and let grow on various PDMS fibers until confluence to form convexly curved *f*-CTs of varying diameters. (**B**) 3D fluorescent representations of H1-GFP MDCK *f*-CTs of different diameters. Actin, red and nuclei, green. Scale bars, 50µm. (**C**) A cross-sectional fluorescent image of a confluent MDCK *f*-CT of Ø = 75 µm, stained for apical marker – Gp135 (green), actin (red) and DAPI (blue). The white dashed lines denote the borders of PDMS microfiber (marked as teal area). Zoom-in image highlighted by magenta dashed-box is shown at the lower part of the image. Scale bar, 20µm. (**D**) Time-lapse 2D projections of a H1-GFP MDCK *f*-CT rotating on a Ø = 100 µm PDMS microfiber. Tracking individual cell nuclei shows cell trajectories as parallel colored lines. Scale bar, 20 µm. (**E**) Graph showing counts of clockwise and counter-clockwise rotating *f*-CTs of varying Øs. (**F**) Graph presenting percentage of CeR events observed in *f*-CTs of different diameters (*n* = 4-9 for each condition).
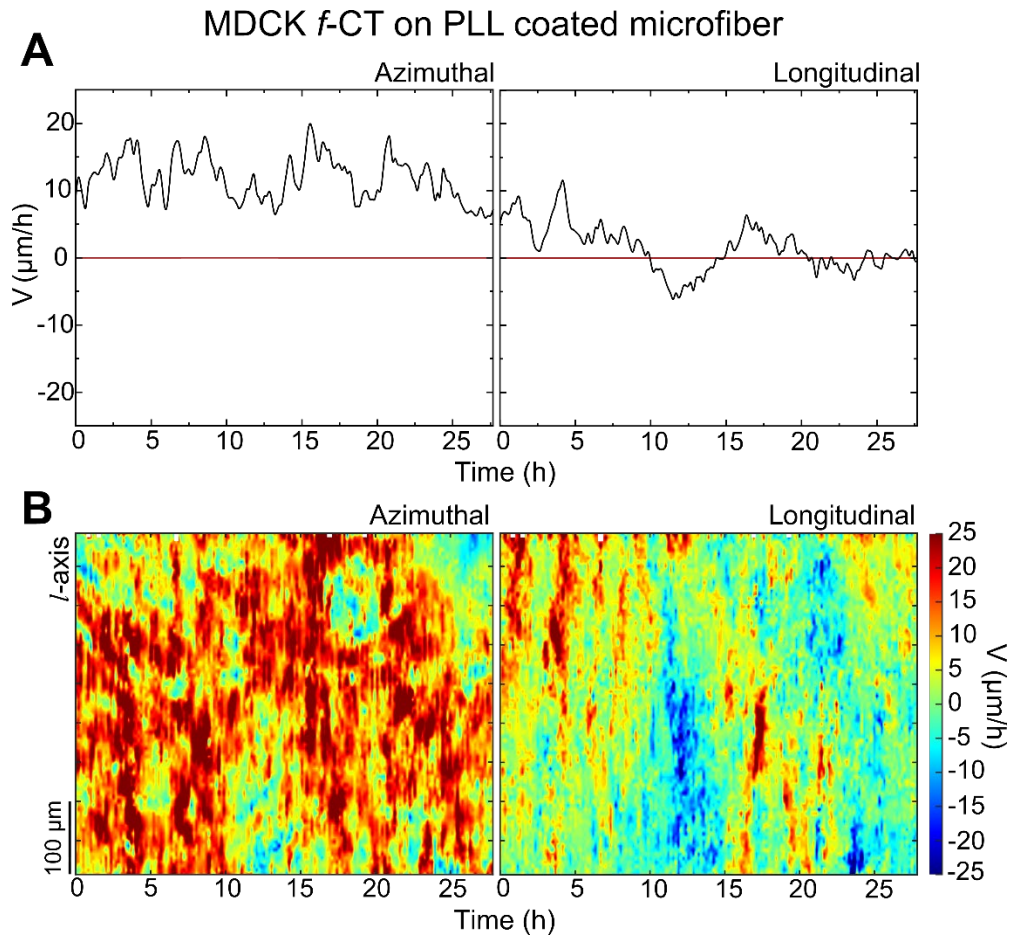
Fig. S8.
(**A**) and (**B**) Representative graphs (**A**) and kymographs (**B**) (like fig. S3) showing average velocity of a H1-GFP MDCK *f*-CT in azimuthal and longitudinal directions and spatial distribution along *l*-axis as a function of time. The *f*-CT grows on a PLL-coated PDMS microfiber of Ø = 75 µm.
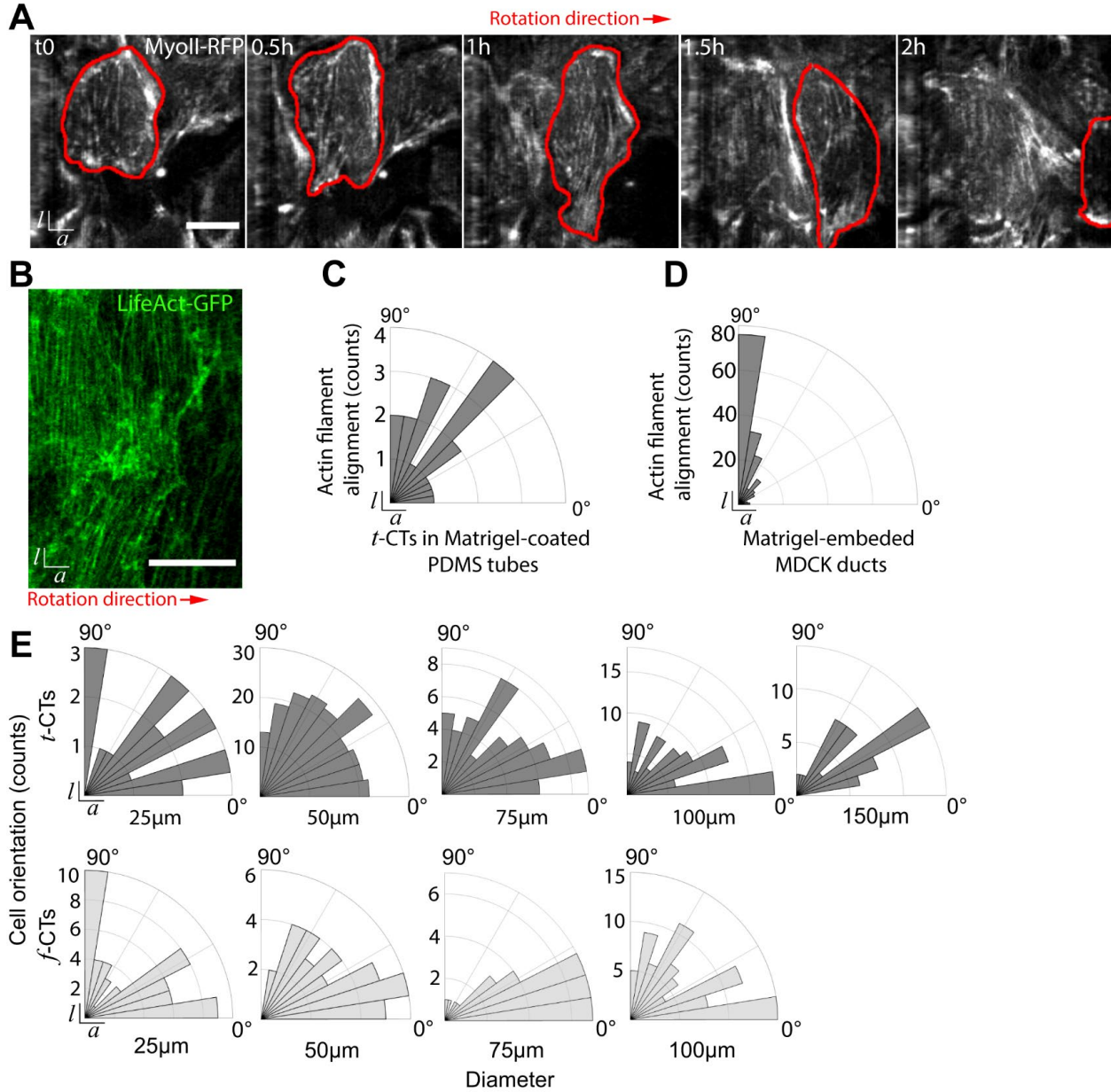
Fig. S9.

(**A**) 2D time-lapse projections of a MDCK t-CT (Ø = 50µm) expressing Myosin IIA-RFP showing alignment of actomyosin network is perpendicular to its CeR direction. Cell periphery is marked by red line. (**B**) 2D projection of a MDCK t-CT (Ø = 100µm) expressing LifeAct-GFP presenting longitudinally aligned actin filaments in a Matrigel-coated PDMS microtube. (**C**) and (**D**) Rose diagrams showing actin filament alignment in t-CTs (Ø = 75 and 100µm, n = 18) inside Matrigel-coated PDMS microtubes (**C**) and in Matrigel-grown MDCK ducts ((**D**), Ø = 20 – 75µm, n = 183). The angle between actin filaments and the azimuthal axis was calculated. (**E**) Rose diagrams presenting cell orientation in different CTs. An ellipsoidal fit to cell shape was performed and cell orientation is the relative angle between the major ellipsoid axis and the azimuthal axis (n = 19 – 211 for each condition).

Rotation direction ➡

Paxillin
Actin

l ⌐
a

MDCK *t*-CT

l ⌐
a

MDCK *f*-CT
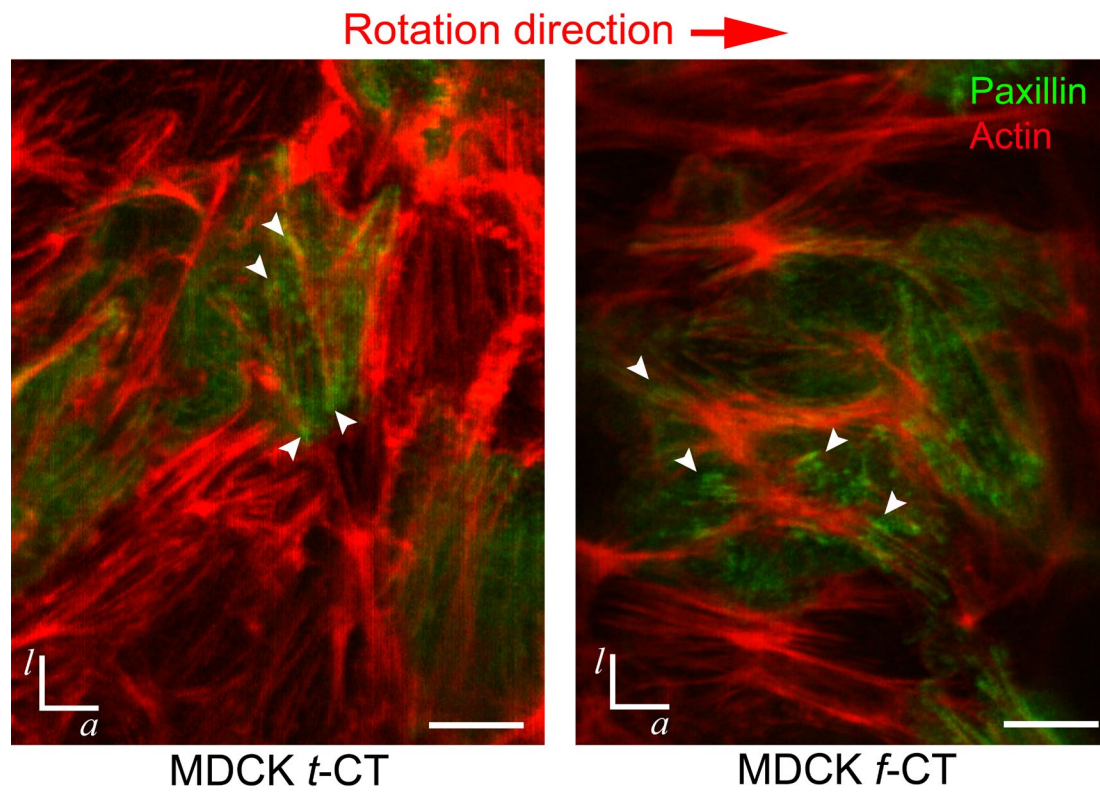
Fig. S10.
Fluorescent images showing paxillin (green) and actin (red) in rotating MDCK *t*-CT and *f*-CT. White arrowheads mark paxillin staining. Scale bars, 10 µm.

26
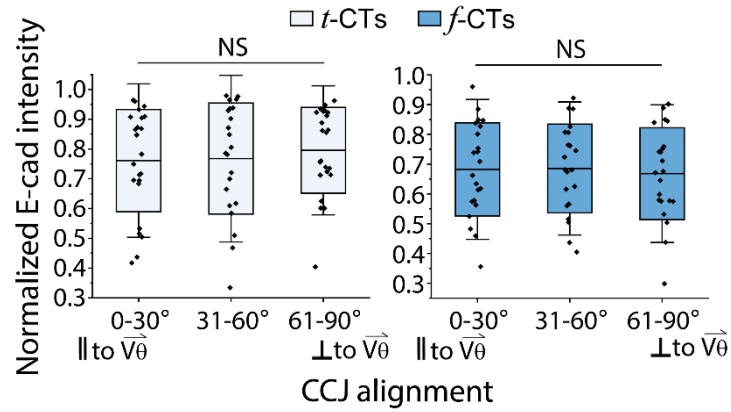
Fig. S11.

Normalized E-cadherin fluorescent intensity in CCJs of different orientations (relative to the CeR direction, i.e., a-axis) in t-CTs and f-CTs. The relative angles between CCJs and $\overrightarrow{V_\theta}$ were presented in x-axis (left panel, $n = 66$ and right panel, $n = 65$). Data are shown as individual values overlapped with box charts showing mean $\pm$ s.d. (coef = 1 for the box and coef = 1.5 for the whiskers). Student's t-test, NS non-significant.
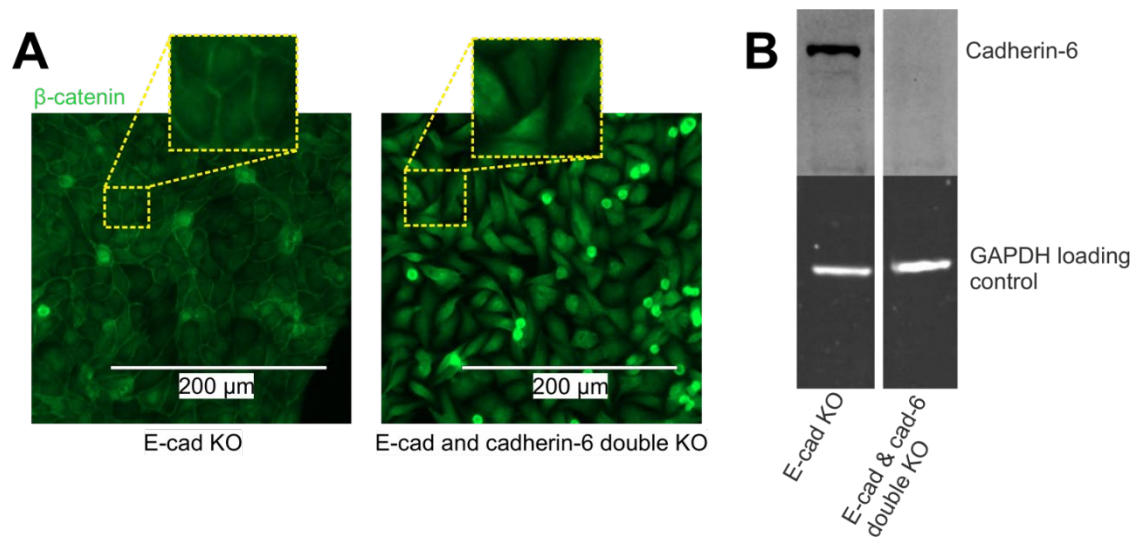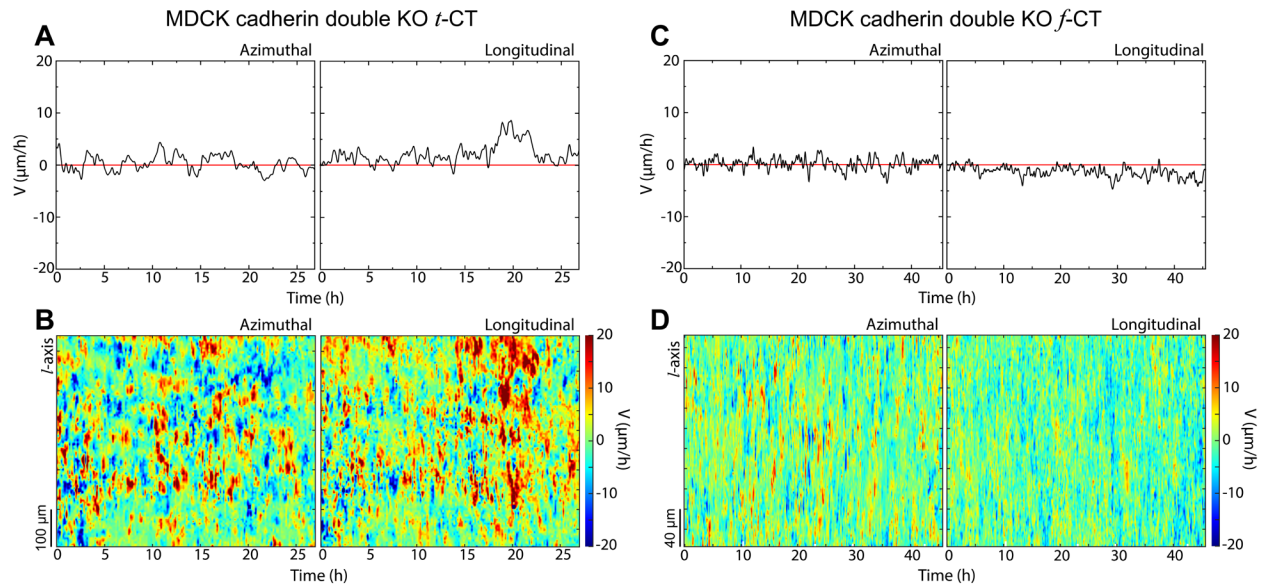
Fig. S12.

(**A**) Immunofluorescence staining of β-catenin, along with (**B**) representative western blot for cadherin-6 (cat-6) in MDCK E-cad KO and MDCK E-cad&cadherin-6 double KO cells.
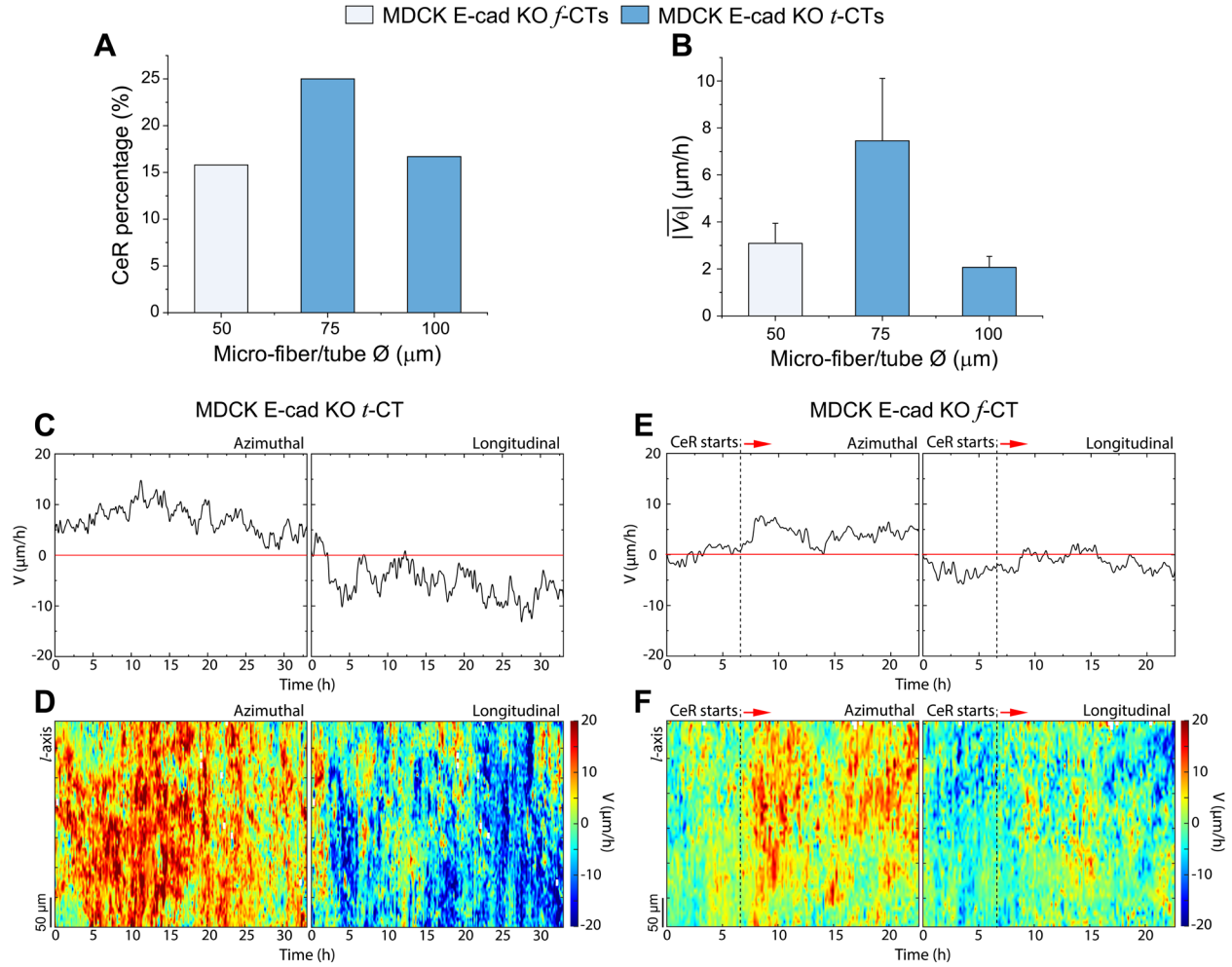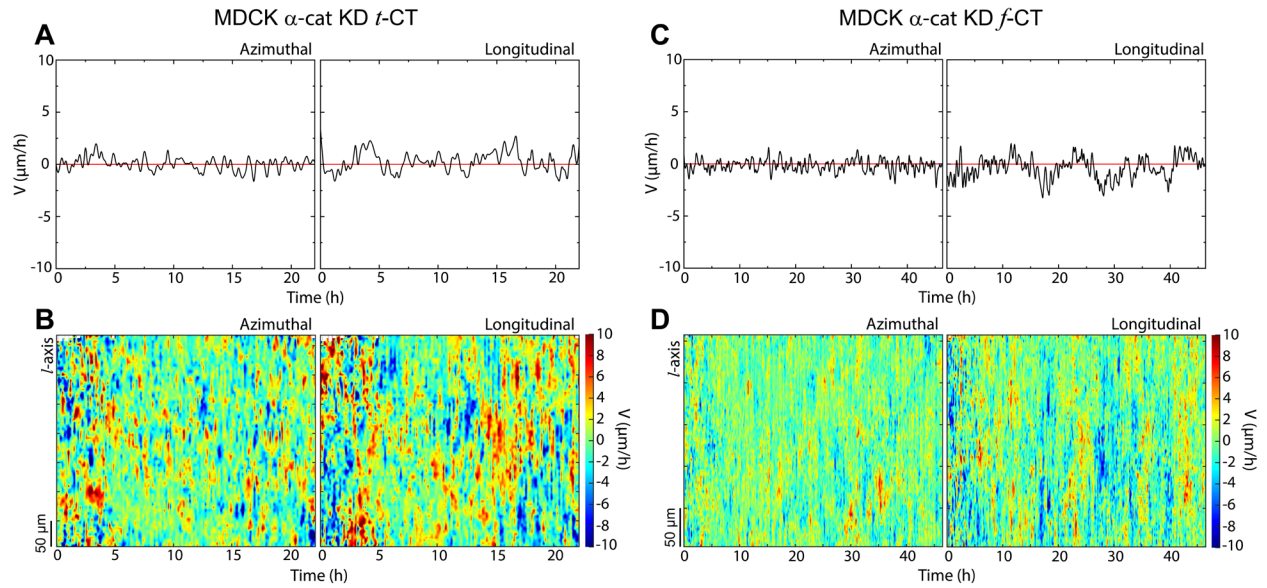
Fig. S13.
(**A**) Column graph presenting percentage of CeR events observed in E-cad KO *t*-CTs and *f*-CTs of different diameters. *n* = 19 – 24 for each diameter. (**B**) Graph showing $|\overline{V_\theta}|$ of different E-cad KO *t*-CTs and *f*-CTs. *n* = 3 – 5 for each diameter. In (**A**) and (**B**), values are mean ± s.d. (**C**) and (**D**) Representative graphs (**C**) and kymographs (**D**) (like fig. S3) showing average velocity of a MDCK E-cad KO *t*-CT with Ø = 75 µm in azimuthal and longitudinal direction, as well as spatial distribution along *l*-axis as a function of time. (**E**) and (**F**) Similar representative graphs and kymographs for a MDCK E-cad KO *f*-CT with Ø = 50 µm as (**C**) and (**D**).
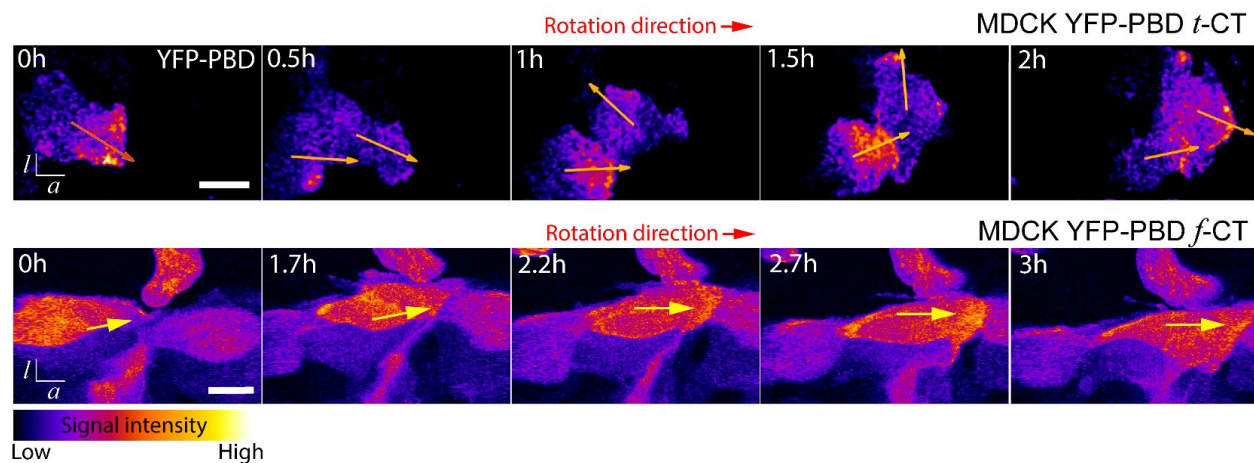
Fig. S14.
(**A**) and (**B**) Representative graphs (**A**) and kymographs (**B**) (like fig. S3) showing average velocity of a MDCK cadherin double KO *t*-CT with Ø = 75 µm in azimuthal and longitudinal direction, as well as spatial distribution along *l*-axis as a function of time. (**C**) and (**D**) Similar representative graphs and kymographs for a MDCK cadherin double KO *f*-CT with Ø = 50 µm as (**A**) and (**B**).

Fig. S15.

(**A**) and (**B**) Representative graphs (**A**) and kymographs (**B**) (like fig. S3) showing average velocity of a MDCK α-catenin knock-down (KD) *t*-CT with Ø = 75 µm in azimuthal and longitudinal direction, as well as spatial distribution along *l*-axis as a function of time. (**C**) and (**D**) Similar representative graphs and kymographs for a MDCK α-catenin knock-down *f*-CT with Ø = 50 µm as (**A**) and (**B**).

Fig. S16.

2D time-lapse projections of MDCK expressing YFP-PBD in rotating *t*-CT (Ø = 50 µm) and *f*-CT (Ø = 50 µm). PBD signal intensity is displayed in fire color code. Orange arrows indicate the direction of protrusions. Scale bars, 20 µm. Red arrows indicate CeR direction.

Movies S1 to S14

Movie S1.
Persistent collective rotation in MDCK acini. Scale bar, 50 μm.

Movie S2.
Persistent collective rotation in a MDCK duct.

Movie S3.
Helical movement in an elongating pronephric tubule expressing a membrane-bound GFP and H2B-mcherry in nuclei. Cell trajectories are portrayed with varying color lines. Scale bar, 10 μm.

Movie S4.
Persisting collective rotation in a H1-GFP MDCK tubular cylindrical tissue (*t*-CT). Scale bar, 50 μm.

Movie S5.
Particle imaging velocimetry mapping of collective rotation in a H1-GFP MDCK *t*-CT (2D projection). Scale bar, 50 μm.

Movie S6.
Helical movement of an advancing H1-GFP MDCK *t*-CT. Scale bar, 50 μm.

Movie S7.
Particle imaging velocimetry mapping of evolution of a H1-GFP MDCK *t*-CT with two adjacent groups of cells rotating in opposite directions. Scale bar, 50 μm.

Movie S8.
Traction force microscopy measurement of a rotating H1-GFP MDCK *t*-CT in a soft silicon microtube. Scale bar, 40 μm.

Movie S9.
Synchronized collective rotation in a H1-GFP MDCK cylindrical tissue on a microfiber (*f*-CT). Scale bar, 50 μm.

Movie S10.
2D projection of a rotating MDCK *t*-CT expressing myosin-IIA RFP showing *a*-axial movement of cells with *l*-axial aligned actomyosin networks. Scale bar, 20 μm.

Movie S11.
Y-27 treatment on rotating H1-GFP MDCK *t*-CT fails to halt collective rotation. Scale bar, 100 μm.

Movie S12.
Persisting collective rotation in an Ecad-KO MDCK *t*-CT expressing LifeAct-GFP. Scale bar, 50 μm.

Movie S13.
Radom cell movement in a confluent MDCK cadherin double KO *t*-CT. Nuclei were stained with NUCLEAR-ID® Blue DNA Dye. Scale bar, 50 μm.

Movie S14.
A rotating MDCK *f*-CT expressing LifeAct-GFP showing persistent *a*-axial actin filaments. Scale bar, 10 μm.